Università degli Studi di Napoli "Federico II"

Dottorato in
Fisica Fondamentale ed Applicata

XXII Ciclo

Dr. Antonio Di Nitto

Thesis for Doctor of Philosophy degree

Study of fission dynamics in the systems of intermediate fissility: ^{132}Ce and ^{158}Er.

Coordinatore
Prof. Lorenzo Marrucci

Novembre 2009

Contents

4

Introduction

Since its discovery, the fission process has proved to be a powerful probe for the properties of the nuclear matter. The early work of Davies and collaborators in 1976, based on the analysis of the total kinetic energy of the fission fragments for a large variety of heavy nuclei, is one of the first experimental evidences that nuclear matter is highly viscous. Although indicative of this property of the nuclear matter, this observable alone was not sufficient to precise the nature of nuclear viscosity. In particular, whether nuclear dissipation proceeds primarily by means of individual two-body collisions (two-body friction), as in the case of ordinary fluid, or by means of nucleons colliding with a moving potential wall (one-body friction), remain an open question. Since then, an increasing interest for this subject triggered much experimental and theoretical work on heavy ion induced fission, aimed at studying the nature of viscosity and its role in fission dynamics.

The observation of an excess of pre-scission light particles and γ-rays, with respect to the predictions of the statistical model, for nuclei in a wide range of mass, has been one the most direct confirmation that fission is a slow process dominated by the nuclear viscosity. These studies, mainly based on pre-scission neutron multiplicities, provided estimates of the fission time scale within a phenomenological approach relying on the statistical model. A value of $\tau_{\mathrm{f}} = (35+15) \times 10^{-21}$s has been reported by Hinde and collaborators, although the estimates from the other numerous studies are spread out over a wide range of values $(5 - 400 \times 10^{-21}$s$)$, depending on the system and on the experimental probe.

More realistic approaches have been used to study the role of viscosity in fission dynamics. They rely on the transport equations of nuclear matter, as the Langevin equations. These latter have been used to analyse the experimental total kinetic energy and the neutron pre-scission multiplicity for ^{200}Pb nuclei; the data are consistent with one-body dissipation. Opposite results are reported on the base of systematic studies using deterministic dynamical models, which indicate two-body mechanism as responsible for energy dissipation in fission. On the basis of a review of the current studies on the

subject, the friction coefficient β values range from $\simeq 2$ to $\simeq 30 \times 10^{21} \mathrm{s}^{-1}$, with rather controversial conclusions on the nature of energy dissipation.

In this framework many questions still remain open. As mentioned, they mainly refer to a precise determination of the fission time scale as well as to the nature of the dissipation. Furthermore, the strength of viscosity and its dependence on the deformation and/or temperature are still largely debated. The lack of constraints to the models are expected to be one of the main sources of discrepancies. In this respect, the systems of intermediate fissility, compared to the heavier ones, have larger pre-scission charged particle multiplicities as well as comparable fission and evaporation residue cross sections. Therefore, the measurements of light particle multiplicities and energy spectra in the two channels as well as of the channel cross sections, allow to put severe constraints on the models, implying more reliable values of fission delay and of the friction parameter. Another source of uncertainty is related with the use of phenomenological approaches, which don't take into account for the dynamics of the process.

In this framework, my research work has been devoted to the study of fission dynamics in the systems of intermediate fissility: 200 MeV ^{32}S $+^{100}$ Mo and 180 MeV ^{32}S $+^{126}$ Te. For these systems, charged particle multiplicities in the pre-scission and evaporation residue channels, as well as channel cross sections and Mass-Total kinetic energy distributions of the fission fragments have been measured. Experiments have been carried out using the 4π charged particle detector 8πLP and the electrostatic deflector at the Laboratori Nazionali di Legnaro coupled to the TOF spectrometer CORSET for fission fragments. A large amount of data has been analysed and all the extracted observables have been compared with the predictions of the statistical model and with a more realistic model based on three dimensional Langevin equations. The numerous Monte Carlo simulations have been filtered trough the response function of 8πLP. The main objective of this work is to explore the mentioned aspects of fission dynamics, still debated, on the base of an extended set of data and in a realistic theoretical framework.

In this thesis, will be first illustrated some introductory concepts regarding the formation and the decay of the composite system, than a brief overview of the main studies on fission dynamics is presented. In particular, starting from the phenomenological studies on fission time-scale, the approaches used to study the nature and the intensity of nuclear viscosity in the fission process are described. The main open questions on fission dynamics are briefly described at the end of the first chapter. A second topic, described in this thesis, regards the nuclear models used in the present work. In particular, the second chapter is devoted to describe the main physical ingredient of the statistical model, the rotating liquid drop model, and finally of

the dynamical model based on three dimensional Langevin equations. A description of the experimental set-up and the data analysis of the two studied systems is given in the third chapter. Details of 8πLP apparatus at the LNL as well as of the CORSET TOF spectrometer and the LNL electromagnetic separator are given. In the same chapter the extraction of the observables in the evaporation residue and fission channels are described. The last chapter is devoted to the results obtained by the comparison of the data with the statistical and the dynamical model.

Chapter 1

Studies of fission dynamics: a brief overview

Since its discovery, nuclear fission has proved to be a powerful probe for the properties of nuclear matter. It is well established that fission is a slow process dominated by nuclear viscosity. The most striking experimental evidence of this behaviour is the observed surplus of pre-scission light particles, with respect to the predictions of the SM, with the increase of excitation energy. Empirical studies with this model allowed to obtain estimates of the characteristic time, and, in some cases, of the strength of nuclear viscosity. More realistic studies of nuclear viscosity have been carried out with dynamical models using deterministic and stochastic approaches. Although much work has been devoted to fission dynamics, there are still many open questions. They mainly refer to the time-scale, the strength and nature of dissipation, as well as the dependence on the temperature and shape of the fissioning system.

In this chapter I will briefly recall the basic physical concepts underlying the compound nucleus decay. Then a brief review will be presented on the main studies of fission dynamics, based on the statistical and dynamical models. Particular attention is paid to the physics underlying nuclear viscosity and the transport equations of nuclear matter: the Langevin and the Fokker-Plank equations. The main open questions are addressed at the end of the chapter.

1.1 Formation and decay of the compound nucleus

Heavy ion collisions at energies over the Coulomb barrier, have high probability to proceed through the complete fusion of the projectile and the target, with the formation of a compound nucleus (CN). In the fusion process, the kinetic energy available in the center of mass system is completely dissipated through a series of nucleon-nucleon interactions inside the dinuclear complex. The CN is produced in an excited state and decays subsequently with times $\tau > 10^{-21}s$ through two main mechanisms: particle evaporation and fission. The main features of this decay rely on the thermodynamical equilibrium reached by the system which is characterized by an excitation energy U and an angular momentum $\vec{J}$. In agreement with the observation of the long life times that characterize the CN, in 1936 Bohr suggested the independence between the two processes: formation and decay of the system. This allows to factorize the cross section in two terms: the fusion cross section of the colliding ions σ_{fus} in the entrance channel $a(x, A)$ and the decay probability $G(b)$ of the compound nucleus in the exit channel $b(y, B)$:

$$\sigma_{a \to b} = \sigma_{fus} G(b), \qquad (1.1)$$

When an isolated state is populated, the reaction cross section have a typical *resonant behaviour* trend expressed by the Breit-Wigner formula [Hog78]. Such situation concerns states at low excitation energy.

With the increase of the excitation energy the mean spacing between the nuclear levels is reduced and at the same time their width increases. This implies in the region of high excitation energy that many states of the compound nucleus are populated in the reaction, whose widths are superimposed, and a treatment based on the statistical physics is needed to describe the decay. In particular the concept of level density $\rho(E)$ becomes important.

In this region, called continuum region, the *statistical model* (SM) allows to calculate the decay probabilities of the CN in each channel energetically accessible. In such contest the consistent treatment of the fusion-fission (FF) and fusion-evaporation (FE) decay channels can provide quantitative predictions of all relevant quantities of the decay products, such as the cross sections, the angular distributions and the energy spectra of the reaction products.

The *complete fusion cross section* σ_{fus} can be obtained by measuring the fusion-evaporation σ_{FE} and fusion-fission σ_{FF} cross sections:

$$\sigma_{fus} = \sigma_{FE} + \sigma_{FF} \qquad (1.2)$$

The prevailing of one of the two terms depends essentially upon the mass of the compound nucleus. In general, in the case of light nuclei ($A < 100$ a.m.u.) the term σ_{FE} dominates while, with the increase of the mass of the compound nucleus, σ_{FF} becomes comparable to σ_{fus}, the former becoming dominant for heavy nuclei.

1.1.1 Evaporation residue channel

Owing to the angular momentum transfered to the compound nucleus by the reaction, the excitation energy U is given by:

$$U = E_{th} + E_{rot} \tag{1.3}$$

where E_{rot} is the collective rotational energy and E_{th} is the thermal energy associated to the excitation of intrinsic degrees of freedom.

The classical relation between the rotational energy E_{rot} and the total angular momentum $\vec{J}$ is:

$$E_{rot} = \frac{|\vec{J}|^2}{2\Im} \tag{1.4}$$

where $\Im$ is the inertia momentum of the nucleus. At high excitation energy $\Im$ can be calculated using the rigid sphere approximation:

$$\Im = \frac{2}{5}MR^2 \tag{1.5}$$

A schematic description of the CN decay in the evaporation channel, to the final states of the evaporation residue, can be obtained using the U-J plane shown in Fig. 1.1. The values of the rotational energy in this plane identify the *Yrast-line*, below which no states are allowed to the CN. In the figure, one Yrast-line approximates all the decays of the nuclei involved in the evaporative chain. In the upper part of Fig. 1.1 is shown the triangular distribution of the angular momentum in the entrance channel, while on the left the level density $\rho(U)$. The CN starts to decay from the initial excitation energy U_i in the continuum region and an angular momentum J_i. At high excitation energy, light particle emission dominate with respect to the electro-magnetic radiation emission and the nucleus decays initially with the emission of n, p and $\alpha-$particle losing part of excitation energy and of the angular momentum according to the conservation laws.

The process continues with further emissions till the excitation energy of the residual nucleus is less than the minimum needed for the emission of a particle. The final residue $\{Z_{ER}, A_{ER}\}$, called evaporation residue (ER), will be still in an excited state in the continuum region, called region of *Entry*
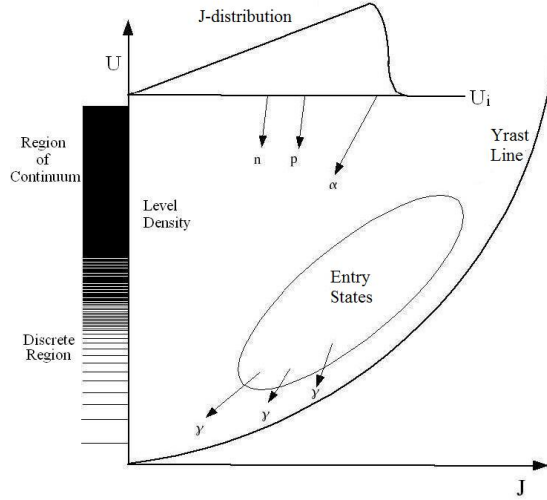
Figure 1.1: U-J plane representation of the decay of a compound nucleus. The yrast line represents the rotational energy of the nucleus, instead the distance between U_i and the yrast line is the thermal energy of the nucleus. The initial angular momentum distribution (upper part) and the level density (left) are also shown.

States as shown in Fig. 1.1 . The decay in this region occurs only by emission of $\gamma-$rays till the ground state is reached. The $\gamma-$ray emission from the entry states starts in the continuum region reaching the region of the discrete level density in proximity of the Yrast-line.

The emission of a light particle is the result of a competitive process, which will be analyzed more in detail in the next chapter. As a general behaviour, the neutron emission is favored with respect to the emission of charge particles because of the Coulomb barrier. For heavy nuclei the neutron emission becomes dominant, while for medium-light nuclei the charged particles compete more effectively with the neutrons.

The angular momentum plays an important role in particle emission, especially for light nuclei. To show these effects, in the Fig.1.2 the decay of nuclei ^{44}Sc and ^{46}Ti are presented in the U-J plane. From the figure it is evident that the plane can be divided qualitatively in many regions, each of them being characterized by the prevalence ($> 50\%$) of the decay of a kind of particle. We can notice that the $\gamma-$decay is prevalent at low energy, instead the $\alpha-$decay at high values of angular momentum. The most probable evaporative cascades of the nucleus ^{46}Ti at $E_{LAB} = 76$ MeV is presented in the right part of the figure. The $\alpha-$particles are shown by thick arrows and neutrons by thin arrows. One can see that the increase of the angular momentum
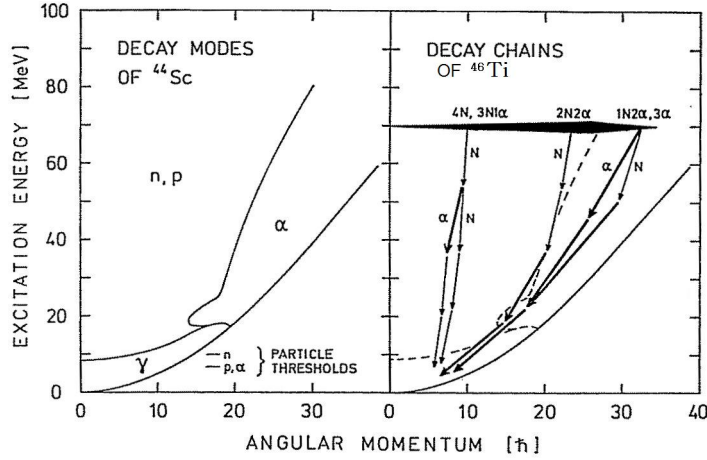
Figure 1.2: Dominant decay modes (partial widths > 50%) for the nucleus ^{44}Sc. In the right-hand part of the figure, the most likely decay chains in the decay are indicated for different angular momenta of compoundus nucleus ^{46}Ti. Heavy arrows for $\alpha-$emission, thin ones for nucleons (from [Puh77]).

of the compound nucleus, enhances the probability of $\alpha-$particles emission, these particles being more effective to take away angular momentum.

Once created, the compound nucleus proceeds along the beam direction and the recoil, produced by the particles emission, determines the angular distribution of evaporation residues inside a cone with an angular opening of few degrees around the beam direction. The ER's are distributed in mass, charge and energy, reflecting the emission of different kinds of light particles.

As will be seen in the next chapter particle evaporation is governed by two main quantities: the transmission coefficients and the level density.

The observation of ER's with indirect methods can be done through the measurement of the discrete characteristics $\gamma-$rays and is more practicable in the case of low excitation energy, which involves a limited variety of nuclei. The direct observation of residues implies the use of mass spectrometers, electrostatic deflectors or techniques based on the measure of time of flight (TOF). They observed energetic spectra of the emitted particles in the CN decay shown an evaporative behaviour [Wei40].

Their angular distributions of the evaporated particles, in the center of mass system, shows a symmetry around $\theta = 90^o$ with respect to the direction of the beam reflecting the evaporative nature of the emission.
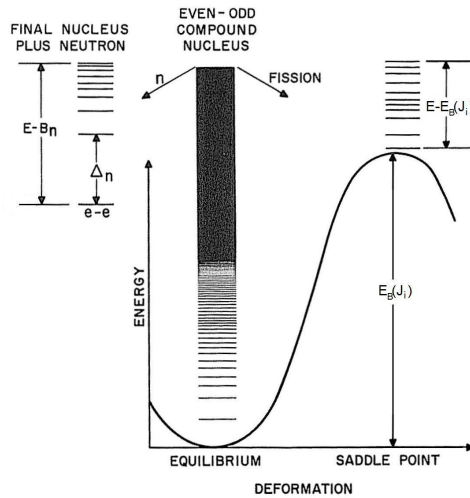
13

Figure 1.3: Potential as function of the nuclear deformation. The corresponding level spectrum at the equilibrium and saddle configurations is also shown, together with the decay by neutron emission.

1.1.2 Fission channel

The fission process consists in the scission of the compound nucleus in two fragments of comparable mass. The excitation energy of the compound nucleus is transferred not only to the relative motion of the fragments, but also to their intrinsic degrees of freedom and angular momentum.

The fragments are produced in excited states which can decay through light particles evaporation and γ-rays. These particles are called post-scission particles, instead the pre-scission particles are emitted from the compound nucleus before the scission in two fragments.

The fission process can be described assimilating the nucleus to a rotating liquid drop [Coh74](RLDM). According to this model the nucleus behaves as a charged incompressible liquid drop with a constant charge density, and a sharp well defined surface. The equilibrium shapes are determined from the action of the attractive nuclear forces (superficial tension forces) and repulsive forces (Coulomb and centrifugal).

The potential energy, shown in Fig.1.3, has been determined by the RLDM as function of the deformation parameters. The equilibrium configuration represents the minimum of the potential energy, where the model predicts a stable shape, in this configuration an high thermal energy is available, because only a small part of U is spent for nuclear deformation. This is indicated in the figure with the high level density available for the nucleus. The saddle point corresponds to the maximum of the potential energy, where

14

the available thermal energy is smaller. A nucleus reaching the saddle point configuration has high probability to fission. In the figure it is also shown that the decay of the composite system by neutron emission is competing with the fission. The difference between the saddle and the equilibrium point represents the fission barrier (B$_f$).

The fundamental Bohr's hypothesis assumes that the fissioning nucleus reaches the potential barrier in well defined quantum states that constitutes the exit ways towards fission. In this theory, called transitional states theory, the fission probability, as established by Bohr and Wheeler [Boh39] is governed by the transitional level density at the saddle point ρ_{SADDLE} and the transmission coefficient T_l across the barrier

$$\Gamma_f^{BW} \propto \rho_{SADDLE} \cdot T_l. \tag{1.6}$$

This expression is used in the statistical model to describe the compound nucleus decay in the fission channel.

Systematic studies of the mass and total kinetic energy (TKE) distributions of the fission fragments have been carried out in different contexts. At high excitation energies, the mass distribution of fission fragments presents a Gaussian shape with a mean value equal to half of the mass of the compound nucleus (*symmetric fission*). A Gaussian distribution is also observed for the total kinetic energy of the fission fragments. The measurement of this last quantity can provide information on the shape of the compound nucleus at the scission point. In fact the Coulomb repulsion between the two nascent fragments, which is the main contributor to the TKE, is sensitive to the nuclear deformation. Systematic measurements of the mean TKE ($< TKE >$), carried out by Viola and collaborators [Vio85], allowed to obtain the following expression:

$$< TKE >= (0.1166Z^2/A^{1/3} + 9.0)MeV \tag{1.7}$$

where Z and A are the atomic and mass numbers of the fissioning nucleus.

1.2 The statistical model as a tool to study the fission time-scale

The particles emitted during the fission process, and in particular the pre-scission ones, represent a powerful tool to investigate the fission dynamics. This study has received remarkable impulse after the experimental observation of a substantial excess of pre-scission particle multiplicities with respect to the prediction of the SM. These measurements represent the clearest and most dramatic evidence of the effects of nuclear viscosity in fission process.
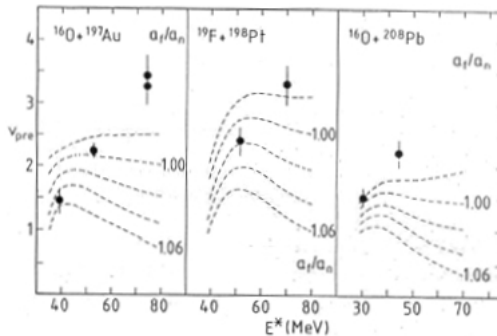
Figure 1.4: Pre-scission neutron excitation functions, measured (points) and calculated using the statistical model (dashed lines) for values of a_f/a_n varying by 0.02 (from [Hin89]).

Owing to the larger cross section, compared to protons and $\alpha-$particles , most of the early works have used the pre-scission neutrons as a probe for the time-scale of the fission process.

1.2.1 The neutron-clock technique

The early works made by Hinde [Hin89] and collaborators concern systems with mass $A = 150 - 250$ and excitation energy in the range $100 - 400 \ MeV$. From the experimental point of view, the study is based on the measurement of neutrons in coincidence with fission fragments. The neutron energy spectra contain the pre- and post-scission contributions. On the base of the different kinematics of the two processes and using simulations to unfold the different contributions, the respective multiplicities have been obtained.

In Fig.1.4 are shown the measured neutron pre-scission multiplicities for the systems $^{16}O +^{197}$ Au, $^{19}F +^{198}$ Pt and $^{16}O +^{208}$ Pb as function of the excitation energy of the compound nucleus. In the figure are also shown the predictions of the statistical model for different values of the ratio a_f/a_n where a_f is the level density parameter for fission and a_n for neutron evaporation. The failure of the SM to describe the steep increase of the pre-scission multiplicities with the excitation energy can be clearly seen in figure.

The physical picture emerging from this observation is that fission is a slow process dominated by nuclear viscosity. During the time needed by the nucleus to reach the scission configuration, a large amount of pre-scission neutrons can be emitted, far in excess to the predictions of the SM. Using the "neutron-clock" technique, this excess can provide information on the "delay time" of the fission process. The link between the pre-scission neutron multiplicities and the fission delay time relies on the probability to evaporate

16

a neutron:

$$\Gamma_n(U, J) = \frac{2s_{n+1}}{2\pi\rho_c(U, J)} \sum_l \sum_{J_R} \int_0^{U-B_n} \rho_R(E_R, J_R) T_l(\epsilon_n) d\varepsilon_n \qquad (1.8)$$

where s_n, ϵ_n, B_n are the spin, the kinetic energy and the separation energy of the neutron, respectively; E_R, J_R, $\rho_R(E_R, J_R)$ and $\rho_c(U, J)$, are the excitation energy, the angular momentum and the level density of the residual nucleus and the emitting nucleus. The level density for a fixed excitation energy U and angular momentum J is provided by the Fermi gas model:

$$\rho(U, J) = \frac{2J+1}{12}\sqrt{a}\left(\frac{\hbar^2}{2\Im}\right)^{\frac{1}{2}} \frac{1}{(U - E_{rot})^2} \exp\left[2\sqrt{a(U - E_{rot})}\right] \qquad (1.9)$$

where a is the level density parameter.

Under the assumption that neutron emission is the dominant channel, Eq.1.8 is a good approximation of the total width of compound nucleus decay Γ_{tot}:

$$\Gamma_{tot}(U, J) \approx \Gamma_n(U, J) \qquad (1.10)$$

The Heisenberg's indetermination principle allows to determine the mean-life τ_n of CN decay:

$$\tau_n = \frac{\hbar}{\Gamma_n(U, J)} \qquad (1.11)$$

Summing the times τ_n for each pre-scission neutron emission one can obtain a relation that connects the neutron multiplicities with the fission time-scale τ.

In Fig.1.5 is shown the neutron multiplicity as a function of τ, calculated on the base of the above mentioned approach for the compound nucleus $^{278}_{110}\text{X}$. The two curves correspond to the calculations assuming neutron emission from the spherical configuration (thick line) and from the extreme scission configuration of two touching spheres (thin line). These configurations of the fissioning system correspond to different excitation energies equal to 149.3 MeV in the spherical case and 74.3 MeV in the deformed one.

From this figure one can infer that the neutron-clock technique is not free from uncertainties, related to the region of excitation energy assumed for the neutron pre-scission emission. A further uncertainty arises from the level density parameter a, for which different values can be adopted. It has been shown by Hinde and collaborators that part of this uncertainty can be removed considering as a further constraint the neutron energy spectra.
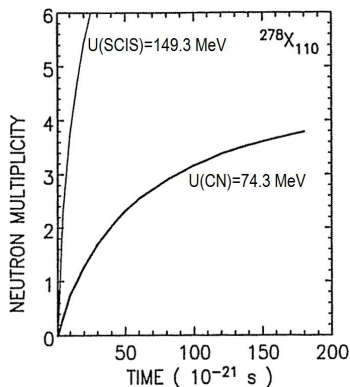
Figure 1.5: Neutron multiplicity as function of time, for the compound nucleus $^{278}_{110}$X at excitation energies corresponding to the equilibrium deformation (thick line) and an extreme scission configuration (thin line) (from [Hin89]).

Following this approach, Hinde and collaborators have modified the statistical model introducing a new free parameter τ_d. In order to describe the slowing down of fission process, because of nuclear viscosity, the fission probability is assumed:

$$
\begin{array}{llll}
\Gamma_f = 0 & for & \tau = \sum_n \tau_n \leq \tau_d \\
\Gamma_f = \Gamma_{BW} & for & \tau = \sum_n \tau_n > \tau_d
\end{array}
\tag{1.12}
$$

where Γ_{BW} is the Bohr-Wheeler standard value of Γ_f [Boh39] adopted in the statistical model. The parameter τ_d can be interpreted as an estimate of the delay of fission, because of the viscosity. A more precise interpretation of this parameter will be given in the framework of the dynamical models. The estimate obtained by Hinde comparing the experimental pre-scission neutron multiplicities for many systems with the predictions of the modified SM, is $\tau_d = (35 \pm 15) \times 10^{-21}$s.

The analysis shows that with the increasing of the projectile energy, most of the excitation energy is removed by the pre-scission emission. This result is indicated by the post-scission multiplicity ν_{post}. In fact it is evident from the Fig.1.6 that this quantity is essentially independent from the initial excitation energy of the CN.

1.2.2   Pre-scission light charged particles

Owing to the low multiplicity, the use of pre-scission charged particles as a probe for fission dynamics has been possible only more recently with the availability of more efficient charged particle detectors. These particles
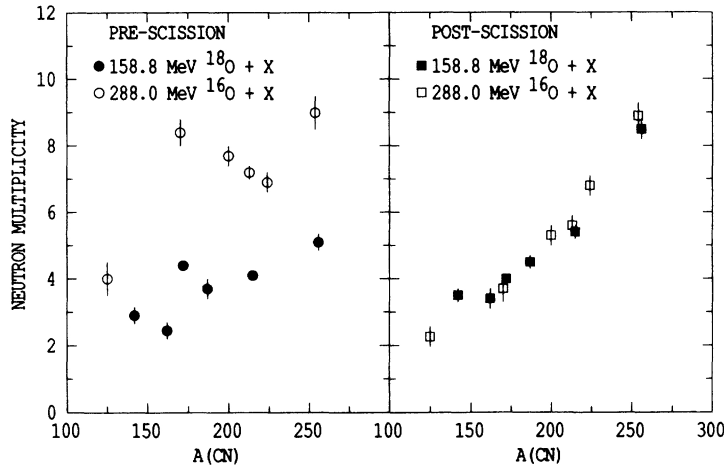
Figure 1.6: Measured ν_{pre} and $2\nu_{\text{post}}$(post-scission multiplicity for both fragments) values for ^{18,16}O induced reactions as function of the compound nucleus mass number. The figure shows that almost all the extra energy brought in by the higher energy ^{16}O projectile is removed by pre-scission emission, since the post-scission multiplicity is almost unchanged (from [Hin92]).

are sensitive to the Coulomb emission barrier, therefore they allow to obtain information also on the average deformation of the fissioning CN.

Studies with light charged particles (LCP's) have been carried out by Lestone and collaborators [Les91] for the reactions $^{28}Si +^{164,167,170} Eu$ at beam energies in the range $140 \div 185\ MeV$ leading to the formation of the compound nuclei $^{192,195,198}Pb$. This work has shown the importance to measure simultaneously pre-scission neutrons, protons and $\alpha-$particles to obtain a more reliable estimate of the total fission time τ_f. In particular, the sensitivity of pre-scission charge particles to nuclear deformation allowed to separate the fission time in two intervals: a pre-saddle time τ_d, where the nucleus has nearly a spherical shape and a saddle to scission time τ_{ssc}, where elongated shapes are involved. In this approach the fission time τ_f is given by:

$$\tau_f = \tau_d + \tau_{ssc} \qquad (1.13)$$

In Fig. 1.7 energy spectra (dots) of protons and $\alpha-$particles measured in coincidence with fission fragments are shown, together with the simulated evaporative pre- and post-scission spectra. From the best fit to the data the pre- and post-scission multiplicities have been extracted.

To obtain an estimate of the characteristic time of the fission process, the SM code JOANNE has been modified to include the fission time, using
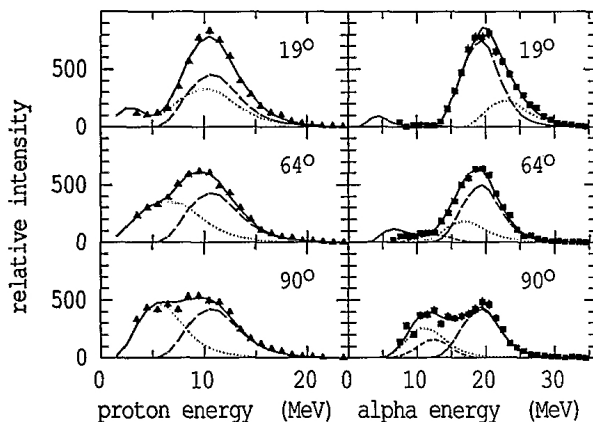
Figure 1.7: Proton and $\alpha-$particle spectra for $^{164}Er +^{28} Si$ at 177.5 MeV, in coincidence with fission fragments at the indicated correlation angles. The simulated pre-scission components are shown as the dashed and dotted lines. The full lines are the sum of these contributions (from Ref.[Les91]).

two free parameters τ_d and τ_{ssc}. In the "pre-saddle" region ($t \in [0, \tau_d]$) the compound nucleus decay by light particles is described assuming a spherical shape (equilibrium configuration) and the fission probability is set equal to 0. In the "post-saddle" region ($t \in [\tau_d, \tau_{ssc}]$), where the nucleus has high probability to fission, particle emission takes place assuming saddle point deformation and rotational energy equal to the mean value between those predicted by the RLDM at the saddle and at the scission point.

In Fig.1.8 the light particle multiplicities are compared with the predictions of the SM for different values of τ_d and τ_{ssc}.

In the calculation with $\tau_{ssc} = 0$ and variable τ_d (left part of the figure), it is observed that, due to the suppression of the fission, there is a large increase of $\alpha-$particle multiplicity with the increase of τ_d, in comparison with neutrons and protons. This is because the process of $\alpha-$particles emission carries away larger angular momentum. Under these conditions the maximum delay τ_d is limited by the α multiplicity.

In the second phase the nucleus (right part of figure) is highly deformed, being close to the scission. This implies a reduction of the mean emission barrier and an increase of the binding energy of the charged particles. As a consequence, the emission of these particles is preferred, due to first effect, while is reduced by the second effect. The superposition of both effects results in a reduction of charged particles emission at scission deformations. For neutrons there is a decrease of binding energy with the increase of deformation,
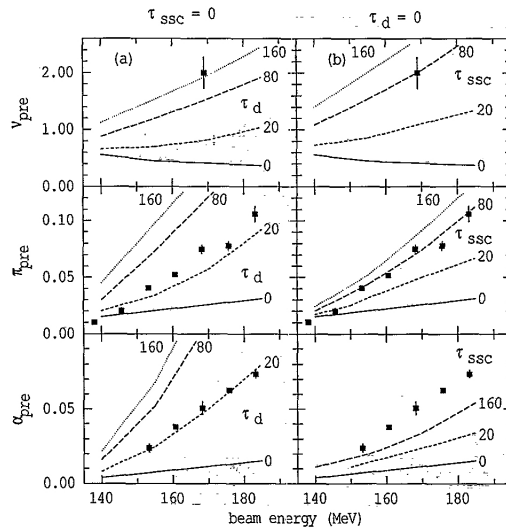
Figure 1.8: Neutron and LCP pre-scission multiplicities measured (dots) for the compound system ^{192}Pb as function of the beam energy. The lines represent results of the simulation: on the left each curve corresponds to different values of τ_d, having fixed $\tau_{ssc} = 0$. On the right side, the value of $\tau_d = 0$ has been fixed, and different values of τ_{ssc} have been calculated (from [Les91]).

so the emission is favored in the second phase and limits the maximum value of delay τ_{ssc}.

These results show that it is not possible to reproduce at the same time the pre-scission multiplicities assuming only one parameter, instead using both τ_d and τ_{ssc} Lestone and collaborators could reproduce the data assuming $\tau_d = 10 \times 10^{-21}s$ and $\tau_{ssc} = 50 \times 10^{-21}s$ for the nuclei $^{192,195,198}Pb$. This implies a total fission time:

$$\tau_f = 60 \times 10^{-21}s. \tag{1.14}$$

In particular, in Fig.1.9 the values of τ_d and τ_{ssc} that better reproduce the experimental multiplicities for the nucleus ^{192}Pb are reported. The lines represent minimum and maximum values of the τ_d and τ_{ssc} that allow to reproduce the experimental pre-scission multiplicities. From the intersection of the areas, which reproduce the data, the hatched region is obtained, which provides the range of values while allow to reproduce all the observables at the same time.

Pre-scission LCP's have been also observed in the work of Ikezoe and collaborators [Ike92, Ike94] for the compound nuclei ^{200}Pb,^{213}Fr,^{216}Ro,^{225}Np and ^{236}Cm at excitation energies in the range U=50-120 MeV. The authors
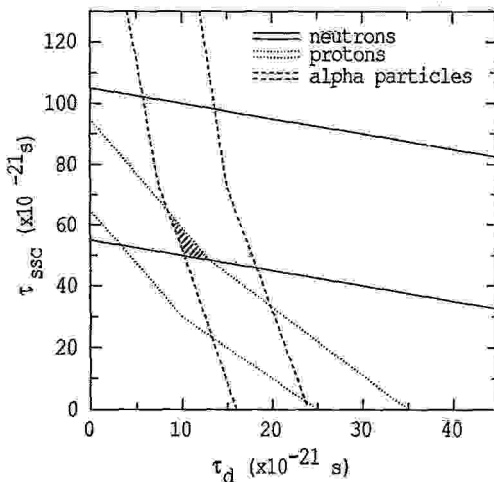
Figure 1.9: Combination of τ_d and τ_{ssc} required to provide acceptable fits to the measured particle multiplicities for ^{192}Pb. The separations of similar lines relate to the experimental errors (from [Les91]).

can reproduce the pre-scission multiplicities of protons and $\alpha-$particles with the statistical model assuming the ratio a_f/a_n within the range between 1.00 and 1.02 and with a delay time of $\tau_d = 5 \times 10^{-21}$s. On the other hand, this value was too small to account for the pre-scission neutron multiplicities, indicating that a significant part of the pre-scission neutrons could be emitted later on in the process, after LCP emission.

This possibility is supported by the angular correlation between $\alpha-$particles and fission fragments which confirms the results of Lestone et collaborators, indicating that the emission of pre-scission $\alpha-$particles occurs mainly from spherical compound nuclei and therefore, in an early stage of the fission process. Furthermore, the post-scission protons and $\alpha-$particles are consistent with the evaporation from the fission fragments with excitation energies considerably reduced by the pre-scission neutron emission.

Although many studies have been carried on the base of pre-scission light particle and $\gamma-$ray multiplicities, using the SM, the reported values of the fission delay are spread out over a large time interval, ranging from 5 to $400 \times 10^{-21}s$, depending on the system and on the experimental probe. The limits of the SM, which cannot account for the dynamical of the process, as well as the lack of constraints to the model itself, are among the sources of these uncertainties.

Another important aspect which must be considered concerning the large dispersion of the estimates of the fission time-scale is the following: based on dynamical models, the fission time distribution is expected to be broad, with

a tail reaching values till $10^4 \times 10^{-21} s$. Pre-scission light particles and $\gamma-$rays are expected to probe only the initial part of this distribution. Furthermore, LCP appear to be emitted preferentially in the early stage of decay, with respect to neutron, therefore, different values of the delay time are expected from these two probes. Concerning $\gamma-$rays , they are expected to be emitted in a wider time range of the time distribution, therefore they reflect larger delay times with respect to light particles.

As will see, although these probes allow to explore only part of the fission time distributions, the comparison of the data with the predictions of realistic dynamical models provide information on the entire time distribution.

In conclusion, although the phenomenological studies provide only limited information on the fission time-scale, the results are very important as they represent the most clear evidence that fission is a slow process dominated by nuclear viscosity. The nature and the strength of this quantity have been studied comparing the data with the predictions of dynamical models.

1.3 The role of nuclear viscosity in the fission process

As mentioned in the previous paragraph, there are several evidences that fission is a slow process dominated by the nuclear viscosity. They relies on the comparisons between the pre- and post-scission light particles multiplicities with the SM. The concept of friction in the crossing of a potential barrier in nuclear fission was introduced by Kramers since 1940. In this framework, he suggested to describe the fission as a diffusion process over a potential barrier, by mean of transport equations of the nuclear matter (Fokker-Plank and Langevin equations). The basic idea of this approach is to assimilate the evolution of the collective variables, describing the shapes of the fissioning systems, to the erratic Brownian motion of particles in a "heat bath" . The role of a heat bath is played by the excitation of the internal degrees of freedom.

The Langevin approach describes the evolution of the system, assuming conservative, frictional and fluctuating forces. Starting, for simplicity, from the case of only one collective variable R, the equation of Langevin can be written as

$$M\ddot{R} = \tilde{F}(R) + F_{frict}(R, \dot{R}) + F_L(R, t) \qquad (1.15)$$

where $\tilde{F}(R)$ represents the conservative force acting on the system, $F_{frict}(R, \dot{R})$ is the friction force and $F_L(R, t)$ is the Langevin force.

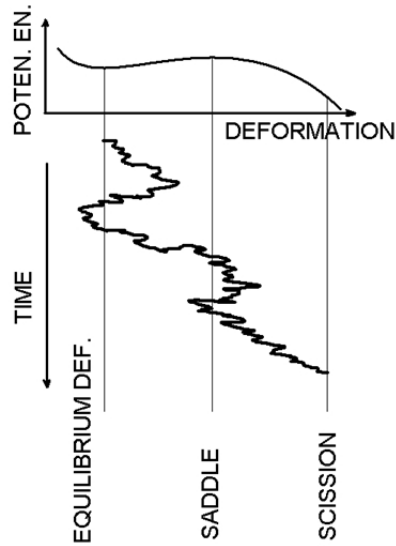In Fig. 1.10 is shown a typical event of fission, in a schematic diagram

Figure 1.10: Fission trajectory calculated by a stochastic model based on Langevin equations.

of a possible evolution of the excited nucleus towards scission predicted by Langevin equations. From the figure is evident how a nucleus can overcome the saddle-point and after can come back, with the possibility to not undergo fission. As will see, these fluctuations produce a reduction of fission probability with respect to that predicted by the B.W. classical approach, where, once reached the saddle point, the nucleus is committed to fission.

Each single random solution of Langevin equations, as that shown in Fig.1.10, is not interesting alone. Rather, one requires the distributions of these solutions, i.e. the distribution function or probability density $d(x;t)$ of the set of variables x as a function of the time t. This distribution function can be obtained sampling a sufficient large number of Langevin trajectories. However, it is possible to convert the Langevin equations into an equation whose solution yields the distribution function directly. This is the Fokker-Plank equation:

$$\frac{\partial f(q,p,t)}{\partial t}+\frac{p}{m}\frac{\partial f(q,p,t)}{\partial q}-\frac{\partial V}{\partial q}\frac{\partial f(q,p,t)}{\partial p}=\frac{\beta}{m}\frac{\partial}{\partial p}(pf(q,p,t))+\beta T\frac{\partial^2 f(q,p,t)}{\partial p^2}$$
$$(1.16)$$

where f(q,p,t) is the distribution associated to the collective variable q(t) and its conjugate momentum p(t) at time t, m representing the mass of nucleus, β the reduced coefficient of friction and T the temperature.

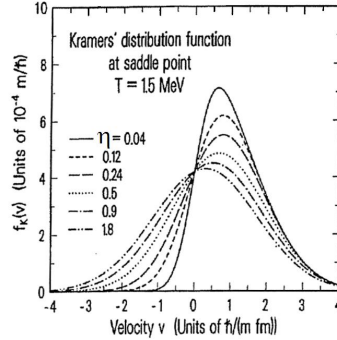Kramers proposed an analytical solution (for one dimension case) of

Figure 1.11: Distribution $f_k(v)$ of velocity at saddle-point corresponding to Kramers' stationary solution, for various values of dissipation strength η (from [Nix84]).

this equation. From that he deduced the stationary fission rate for different values of the reduced friction parameter β. The fission width corresponding to this stationary regime is written as:

$$\Gamma_f^K = \Gamma_f^{BW} \left(\sqrt{1 + \eta^2} - \eta \right) \tag{1.17}$$

where $\eta = \frac{\beta}{2\omega_{sp}}$ is defined on the base of ω_{sp} that is the frequency of the harmonic oscillator potential that osculates the fission barrier at the saddle point.

With respect to the critical value of $\eta = 1$ ($\beta = 2\omega_{sp}$), the region $\eta >> 1$ implies large dynamical effects. In this case we can write:

$$\Gamma_f^K \approx \Gamma_f^{BW} \frac{\omega_{sp}}{\beta} \tag{1.18}$$

which indicates a significant reduction of the fission width with respect to Γ_f^{BW}, with the increase of the reduced coefficient of friction. The physics underlying this reduction relies on the fluctuations in the random walk of the nucleus towards fission, as previously mentioned. This can be understood in more details from the Fig.1.11, where is shown the velocity distribution $f_k(v)$ at the saddle point, corresponding to the solution of Kramers, for different values of η.

The calculation has been done for the nucleus ^{213}At with a temperature at the saddle point $T = 1.5~MeV$. We notice that the width of distribution increases with the friction, producing an increasing fraction of events in the region $v < 0$, where the system comes back to the ground state deformations. These events have low probability to come back to the saddle point and give rise to fission. This implies a reduction of fission width, which is called

25

"statistics". As we will see later, this stationary value Γ_f^K needs a certain time (transient time) to be reached.

Kramers' reduction factor $\left(\sqrt{1+\eta^2} - \eta\right)$ for the fission width has been used by different authors in the statistical model. Within this approach the fission width assumes the Kramers value $\Gamma_f = \Gamma_f^K = \Gamma_f^{BW}(\sqrt{1+\eta^2} - \eta)$ for times $t > \tau_d$ and $\Gamma_f = 0$ for $t < \tau_d$.

1.3.1 One-body and two-body dissipation

The nature of viscosity represents one of the major open question in fission dynamics. The energy dissipation, i.e. the conversion from the collective to intrinsic motion, is a phenomenon related to the motion of nucleons inside the system in route towards fission. The models describing the energy dissipation relies on two mechanisms: one-body and two-body dissipation.

One-body dissipation

The one-body dissipation picture is based on the long mean free path of a nucleon inside a nucleus at a moderate excitation energy. The justification relies on the Pauli principle which limits the phase space accessible to final states of two-body interactions. The other main aspect of the one-body approach is the mean field of the nuclear system acting as a confining vessel. Altogether the nucleons are assumed to behave like a Knudsen gas [Fel87], i.e. they move almost freely inside the system and then bounce elastically at the wall.

One-body dissipation is expected to occur through two mechanisms: the wall and window dissipation. In the wall mechanism the energy dissipation is produced when particles hit a moving wall. This phenomenon occurs in fission, where the nucleons hit the moving surface of the fissioning nucleus. The randomization hypothesis assumes that the bounced particles keep a random velocity distribution. If the motion of the wall is irregular this hypothesis is satisfied. In the framework of this model, the energy dissipation rate is provided by the wall formula:

$$\frac{dE}{dt} = \rho \left\langle v \right\rangle \int_{surface} \dot{n}^2 d\sigma, \tag{1.19}$$

where ρ is the mass density of the nucleus, $\left\langle v \right\rangle$ is the average nuclear velocity relative to the drift velocity, $\dot{n}$ is the relative normal velocity of the wall with respect to the drift velocity of the system.

The window friction mechanism is of a similar nature. It can be shown that considering two nuclei with different mean velocities in contact through

a window, the nucleons crossing the window dissipate energy from collective to intrinsic motion. The transfer of nucleons between two nuclei through a window is the mechanism accompanying the compound nucleus all along its path towards scission in two fragments. In the framework of the model, the energy dissipation is given by:

$$\frac{dE}{dt} = \frac{1}{4}\rho \left\langle v \right\rangle \Delta\sigma(2u_r^2 + u_t^2).$$ (1.20)

where $\Delta\sigma$ is the area of the window between the two nascent fragments at the relative velocity $\vec{u}$, with the component along the normal to the window u_r and the component in the plane of the window u_t.

In realistic calculations for the necked-in shapes of a fissioning nucleus both wall and window mechanisms are applied. For the initial shape of the nucleus, without neck, only wall formula is applied and after appearance of the neck in the shape the wall-and-window formula is used to calculate the friction tensor.

Within this approach, the quantum treatment of one-body dissipation [Blo78] and the analysis of the experimental data on the width of the Giant Dipole Resonance (GDR) have shown that the contribution to the dissipation from the wall mechanism should be reduced. The reduction factor k_s from the contribution of wall formula have been introduced by Nix and Sierk [Nix69]. They have found that the value $k_s = 0.27$ allows to reproduce the experimental data on GDR. The one-body mechanism with $k_s \neq 1$ is usually called modified one-body mechanism, while full one-body refers to $k_s = 1$.

Two-body dissipation

Two body dissipation relies on the nucleon-nucleon interaction. Macroscopic models of this process assimilate the nucleus to a liquid assuming an incompressible irrotational flow during the fission process. This assumption together with the boundary condition would uniquely define the whole velocity field and thereby the collective kinetic energy for the degrees of freedom describing the shape. However, the solution of the resulting Laplace equation is numerically too costly. Therefore, the Werner-Wheeler flow [Kel64] approximation is used [Dav76] where semplificative assumptions are made on the flow velocities.

Both one-body and two-body dissipation are taken into account by the dynamical models through the elements of the viscosity tensor η_{ij}, which are related the dissipative function F, as described in more details in the next paragraph.

Owing to the Pauli exclusion principle, there are reasons to expect that the dominant dissipation process in fission is one-body. However, the expected dominance of one-body effects does not necessarily imply that two-body collision should be ignored, as they can still significantly perturb the situation from an ideal one-body mechanism, especially at high excitation energy.

In this respect, the strength and the nature of nuclear dissipation is expected to be different at equilibrium, saddle and scission configuration, i.e. is shape dependent. Nuclear dissipation is also expected to be temperature dependent [Hil92]. In this framework, both mechanisms could be present in the fission process.

1.3.2 Probing the nature and the strength of nuclear viscosity

The role of viscosity in fission dynamics has been investigated using dynamical models, which describe the evolution of the collective variables defining the shape of the nucleus all along the process towards scission. The predictions of these models have been compared with the most relevant observables of the fission, like the above mentioned pre- and post-scission light particles multiplicities, as well as the total kinetic energy (TKE) and mass distributions of the fission fragments. These studies have addressed fundamental aspects of the nuclear viscosity like:

1. the strength and the nature of nuclear dissipation. As mentioned, one important question is whether this process proceed via one-body or two body mechanism.

2. The dependence of nuclear viscosity on the temperature and on the shape of the fissioning system.

The dynamical models can be divided in two main categories according to the approach: the deterministic and the stochastic approach. The first one is based on classical equations of motion, which describe the deterministic evolution of the nuclear shape, driven by conservative and friction forces. The stochastic approach makes use of the transport equation of nuclear matter: the Langevin and Fokker-Plank equations.

1.3.2.1 Deterministic approach

The effect of viscosity on nuclear fission has been investigated by Davies, Nix and Sierk [Dav76], by solving classical equations of motion, i.e. the La-
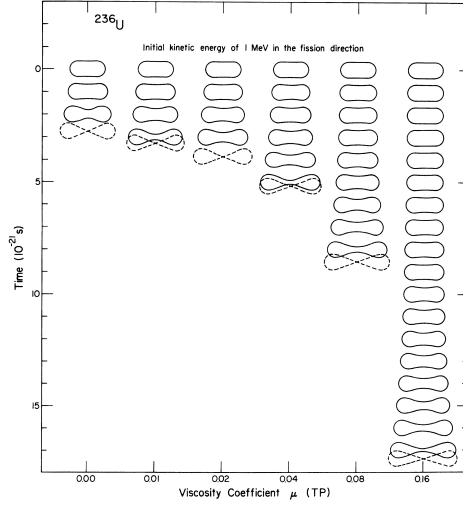
Figure 1.12: Evolution of shapes for the nucleus ^{236}U from saddle point to scission, for different values of the two-body viscosity coefficient μ. The initial condition corresponds to the saddle point with 1 MeV of kinetic energy in the fission direction. The scission shapes are shown with dashed lines (from [Dav76]).

grange equations:

$$\frac{d}{dt}\left(\frac{\partial L}{\partial \dot{q}_i}\right) - \frac{\partial L}{\partial q_i} = \frac{\partial F}{\partial \dot{q}_i} \qquad (1.21)$$

where $q_i\ i = 1, ..., N$ are the generalized coordinates that specify the shape of the system, and where time differentiation is denoted by a dot. Frictional forces are introduced by means of Rayleigh dissipation function:

$$F = \frac{1}{2}\sum_{i,j}\eta_{ij}(q)\dot{q}_i\dot{q}_j, \qquad (1.22)$$

where η_{ij} denotes an element of the shape-dependent viscosity tensor. The rate of dissipation of collective energy into internal excitation energy is equal to 2F.

L is the Lagrangian for the system:

$$L(q, \dot{q}) = T(q, \dot{q}) - V(q) \qquad (1.23)$$

where T is the collective kinetic energy:

$$T = \frac{1}{2}\sum_{i,j}M_{ij}(q)\dot{q}_i\dot{q}_j \qquad (1.24)$$

29

with $M_{i,j}(q)$ the inertia tensor and $V(q)$ is the potential energy of the fissioning nucleus.

In the model only axially symmetric nuclei have been considered, using three deformation coordinates. The inertia tensor is calculated for incompressible, irrotational flow using Werner-Wheeler method. The elements of the friction tensor η_{ij} have been obtained assuming two-body dissipation. The collective potential has been calculated by mean of the usual liquid-drop model and takes into account the lowering in the nuclear macroscopic energy due to the finite range of the nuclear force.

Fig. 1.12 illustrates the shape evolution in the dynamical descending from the saddle to scission configuration for the nucleus ^{236}U, for different values of two-body viscosity. For an initial kinetic energy of 1 MeV in the fission direction, the time from the saddle to scission increases from 2.8×10^{-21} s for zero viscosity to 17.3×10^{-21} s for $\mu = 0.16$ TP. Therefore a viscous ^{236}U nucleus scissions with less translational kinetic energy of the fragments, than a non viscous one. But in addition the scission configuration is more elongated for a viscous ^{236}U nucleus than for a non viscous one.

It must be pointed out that both the smaller translation kinetic energy at scission and the more elongated scission configuration decrease the final translation kinetic energy for the fission fragments at infinity. Therefore, the translation kinetic energy is expected to be a good observable to investigate on nuclear viscosity.

A comparison between the measured TKE for fission fragments at infinity and at pre-scission configuration, for a wide range of nuclei throughout the periodic table, and the prediction of the model is shown in Fig.1.13. It is seen from the figure that the value

$$\mu = 0.015 \pm 0.005 TP = 9 \pm 3 \times 10^{-24} MeVs/fm^3 \qquad (1.25)$$

accounts for most of the experimental data within their uncertainties, although there is a clear variation in the best value of μ from about 0.01 TP for the lighter to about 0.02 TP for the heavier systems.

A similar study has been carried out by Sierk and collaborators. In this work the energy dissipation has been calculated from one-body wall formula until the neck decreases to a critical size, at which point a transition is made to a wall-and-window formula. As it is shown in Fig.1.13(b), the experimental fission-fragment kinetic energies are reproduced when the neck radius at the transition point is 2.5 fm. Taking into account the conclusions of Davies and collaborators, this indicates that the TKE alone does not allow to discriminate between two mechanisms and more observables are needed.

A systematic study of nuclear viscosity has been carried out by C. Bhattacharya and collaborators [Bha96], on the base of pre-scission neutron mul-
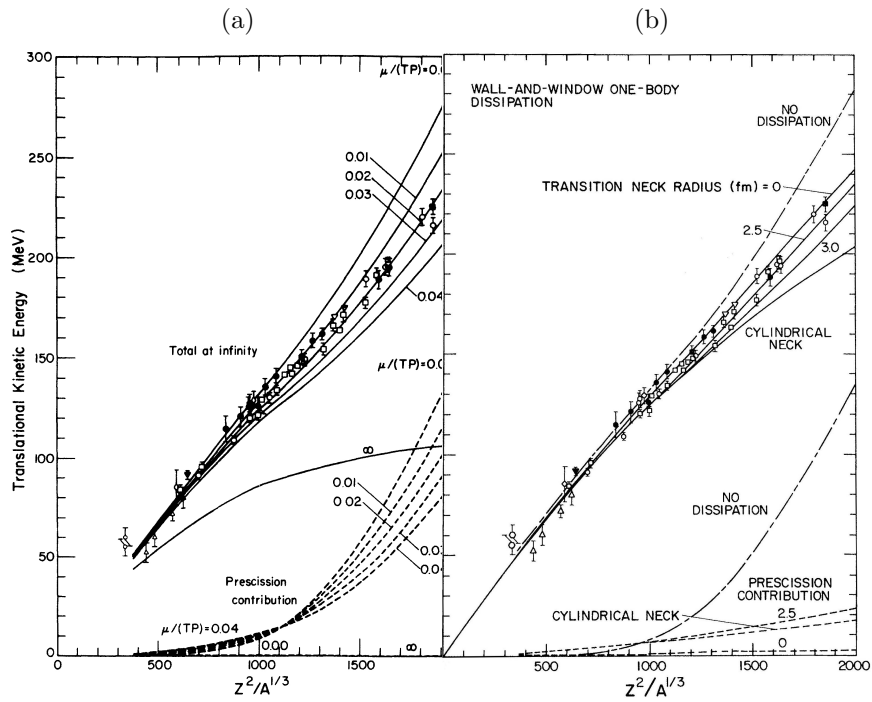
Figure 1.13: Comparison of experimental most probable fission-fragment kinetic energies with the predictions of a dynamical model. (a) Data are compared with the results for different values of two-body viscosity coefficient μ (solid curve). The dashed curves represent the calculated translational kinetic energy at the scission configuration. The limiting result for $\mu = \infty$ is also reported (from [Dav76]). (b) Similar to Fig. (a), with the dissipation given by wall-and-window one-body dissipation, for different transition neck radii (from [Sie80]).
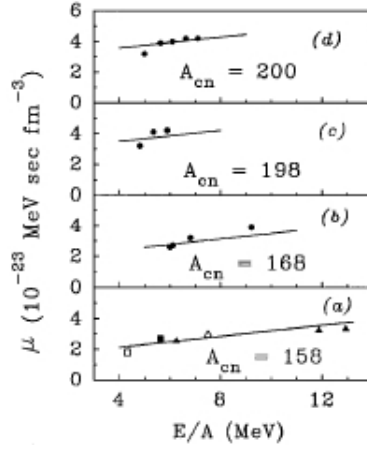
Figure 1.14: Viscosity coefficient μ as a function of bombarding energy (E/A) for various compound nuclei. The solid curves correspond to the values of μ obtained from the global relation 1.26. In (a), filled squares, open squares, filled triangles, and open triangles correspond to $S+Te$, $Ti+Pd$, $O+Nd$ and $Mg+Ba$, respectively. Filled circles in (b), (c), and (d) correspond to $O + Sm$, $Si + Te$ and $F + Ta$ systems, respectively (from [Bha96]).

tiplicities. They have developed a dynamical model where fission trajectories are generated solving Euler-Lagrange equations of motion with dissipative forces derived from Werner-Wheeler prescription, assuming two-body mechanism. Pre-scission neutron emission along the fission trajectory has been simulated through Monte Carlo technique. The predicted pre-scission neutron multiplicities have been compared with experimental data for nuclei in a wide range of mass to extract the optimum value of the viscosity coefficient for each nucleus.

The values of the viscosity coefficients are found to follow the global relation:

$$\mu(E/A, A_{CN}) = aE/A + bA_{CN}^3, \tag{1.26}$$

where E is the bombarding energy.

The values of the parameters $a = 0.180 \pm 0.023$ and $b = 0.357 \times 10^{-6} \pm 0.26 \times 10^{-7}$ have been obtained on the base of a least square fitting of the viscosity coefficients for all the studied systems.

In Fig.1.14 is shown the viscosity coefficient μ as a function of E/A for various compound nucleus masses. The solid curves correspond to values of viscosity coefficient μ obtained from the global relation Eq.1.26. It can be seen that values from 2 to 4×10^{-23} $MeV\,sec\,fm^{-3}$ are obtained.

Considering the value $\mu = 0.9 \pm 0.3 \times 10^{-23}$ $MeV\,sec\,fm^{-3}$ deduced by

32

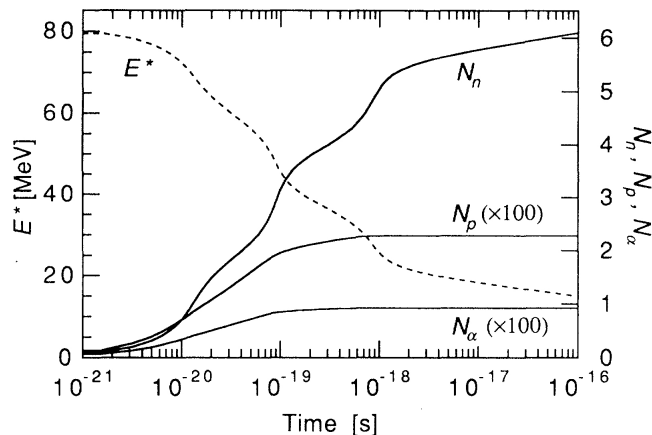**Figure 1.15:** Numbers of emitted neutrons (N_n), protons (N_p) and $\alpha-$particles (N_α) as function of time for ^{200}Pb with initial excitation energy $U = 80.7\ MeV$. Time dependence of the excitation energy (U) is also shown(dashed lines), (from [Wad93]).

Davies for ^{236}U, the Eq. 1.26 provides values significantly higher. As it will be shown in the next paragraph a more realistic study with a stochastic model indicates that two-body dissipation significanlty underestimates the TKE for ^{200}Pb nuclei.

1.3.2.2 Stochastic approach

As already mentioned, a realistic description of fission process can be obtained in the framework of Langevin approach, assimilating the collective coordinates, defining the shape of the fissioning nucleus, to Brownian particles moving in a "heat bath". This latter is represented by the the internal degrees of freedom describing the nuclear excitation.

Fission dynamics of hot nuclei have been investigated using two dimensional Langevin equations by Carjan and collaborators [Car86]. The main goal was to gain insight on the nature of nuclear dissipation, calculating both the neutron pre-scission multiplicity and the TKE of fission fragments, and to compare with experimental data. In the calculations of Carjan et al., the nuclear shapes are described by two collective coordinates on the base of Legendre polynomial parametrization. Neutron, proton, $\alpha-$particle and giant-dipole-resonance $\gamma-$ray were included in the calculation, which have been carried out for the symmetric fission of the nucleus ^{200}Pb, since the following reactions have been studied experimentally: ^{19}F $+^{181}$ Ta (U=80.7 MeV) [Hin86] and ^{16}O $+^{184}$ W (U=195.8 MeV) [Hin92]. Fig.1.15 shows the calculated number of pre-scission particles as a function of time for the initial
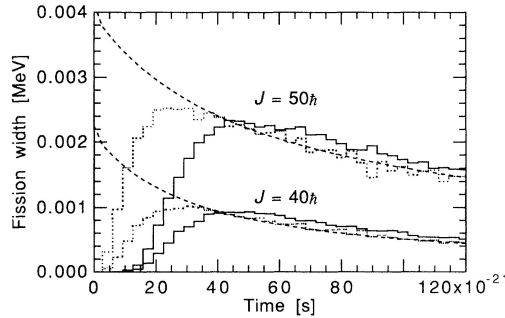
Figure 1.16: Time dependence of the fission width for the symmetric fission of ^{200}Pb for two values of the angular momentum $J = 40\hbar$ and $J = 50\hbar$, at initial excitation energy $U = 80.7 \ MeV$. Solid lines are the widths calculated at scission and dotted lines are those at the saddle. Dashed lines denote quasi stationary fission widths, (from [Wad93]).

excitation energy U =80.7 MeV, assuming one-body dissipation. The step-wise behaviour clearly seen in ν_{pre} is due to changes of the neutron separation energy due to the shell and pairing corrections. As can be seen from the figure, the excitation energy of the compound nucleus (denoted by the dashed line), decreases with time as a result of the emission of the light particles and γ-rays. Fig.1.16 shows the corresponding fission widths as a function of time. The fission width Γ_f is calculated as $\Gamma_f(t) = - \left[1/N(t)\right]\left[dN(T)/dt\right]$, where $N(t)$ is the number of trajectories which did not escape beyond scission (saddle) at time t. One can see that the fission widths (dotted lines at saddle and solid lines at scission) approach the Kramer quasi-stationary value (dashed lines), after a certain time. It is interesting to remark the differences between the static description adopted by the statistical model and the dynamical one: while the first assumes a constant value of Γ_f, in the dynamical model this quantity is a function of time and needs a certain time, called transient time, to reach the stationary value.

In the modified statistical model, used to analyze the pre-scission light particles, the delay time τ_d represents the time needed for Γ_f to reach the value Γ_{BW}. Therefore, it can be identified as the transient time. In particular, from Fig.2 the transient time is about $20 \times 10^{-21} \ s$, somewhat shorter than required by the phenomenological analysis by Hinde and collaborators [Hin89]. Fig.1.16 provide also the saddle-to-scission time (tssc), which is represented by the interval between the dotted and the solid line; its value is $\tau_{ssc} = 20 \times 10^{-21} \ s$. Also this value turns out to be significantly shorter than that derived by Lestone et al. $\tau_{ssc} = 50 \times 10^{-21} \ s$.

Coming to the pre-scission neutrons and TKE of fission fragments, the au-

thors found that both calculated quantities are consistent with experimental values when one-body dissipation is assumed. Unusually strong hydrodynamical two-body viscosity also reproduces the experimental neutron multiplicity, but it significantly underestimates the average kinetic energy. These results indicate that the simultaneous analysis of two observables: the neutron multiplicity and the TKE, provides more reliable information on fission dynamics, allowing to conclude on the dominant nature of the viscosity in fission, for ^{200}Pb nucleus. In this respect, it is worthwhile to remind that the work of Davies et al. and Sierk et al., based on the TKE alone, didn't allow to reach a conclusion on this aspect of fission.

1.3.2.3 Phenomenological approach

The phenomenological approach, based on the comparison of the pre-scission particle multiplicities with the prediction of the SM, has been also used to study the nature and the strength of the nuclear viscosity. The basic idea is the introduction in the SM of the Kramers' reduction factor for the fission width:

$$\Gamma_f^K = \Gamma_f^{BW}(\sqrt{1 + \eta^2} - \eta). \qquad (1.27)$$

In this approach the delay time τ_d represents the transient time needed to the fission width to reach the Kramers' stationary value Γ_f^K. Most of the models assume the following relation between the τ_d and the friction parameter:

$$\tau_d = \frac{\eta}{\omega_{sp}} ln \left(10 \frac{B_f}{T} \right) \qquad (1.28)$$

which has been demonstrated by Grangé and Weidenmüller [Gra80] for $\eta > 1$. In this relation, ω and T represent the frequency of assault to the fission barrier B_f, and T is the temperature of the fissioning system.

In this framework, the nuclear viscosity has been studied for the fission of the composite system ^{188}Pt at U=99.7 and 101.4 MeV [Bad01], on the basis of the measured pre-scission neutron multiplicities and the fission cross sections. The extracted values of the reduced viscosity parameter β are 15 and 24 10^{21}s^{-1}, compatibles with one-body dissipation [Blo92, Wad93].

A different result has been found for the system ^{220}Th by Rubchenya et al. [Rub98], on the basis of pre-scission neutron multiplicities: the effective average value of β decreases with increasing of the excitation energy, similar to the temperature dependence of two-body friction. A similar conclusion comes from the work of Bhattacharya et al. [Bha96] where the values of two-body nuclear viscosity used to predict the observed neutron multiplicities increase with the excitation energy of the composite system.
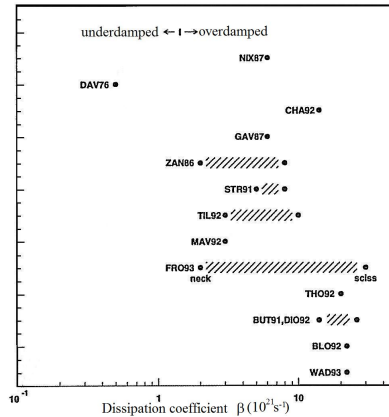
35

Figure 1.17: Experimental values of the dissipation coefficient β (from [Bad01]).

1.3.2.4 Open questions on fission dynamics

As mentioned in the previous paragraph, the nature and the strength of nuclear viscosity have been studied comparing the data with dynamical models or with the SM within a phenomenological approach. A detailed review of these studies has been carried out by Hilsher and Rossner in 1992 [Hil92]. Although much experimental and theoretical work has been devoted to this subject, many questions still remain open. They mainly refer to a precise determination of the fission time scale as well as to the nature of the dissipation and its dependence on the deformation and the temperature.

Concerning nuclear viscosity, as shown in Fig.1.17, the experimental values of the friction parameter range from 2 to 30 $\times 10^{21} \mathrm{s}^{-1}$. This large dispersion reflects the large variety of the studied systems as well as the different approach used (dynamical or phenomenological models). Nevertheless, most of the studies indicate an over-dumped motion ($\beta > 2$) dominated by one-body mechanism.

The lack of constraints to the models could be, in several cases, the source of discrepancies. In this respect, it must be pointed out that in most of the studies only neutron multiplicities have been measured. The systems of intermediate fissility, compared to the heavier ones, have larger pre-scission charged particle multiplicities as well as comparable fission and evaporation residue cross sections. Therefore, the measurements of light particle multiplicities and energy spectra in the two channels as well as of the channel cross sections, allow to put severe constraints on the models,and therefore to obtain more reliable values of the fission delay and of the friction parameter.

Another advantage of these systems is that they are expected to have saddle and scission configurations relatively close in the deformation space.

36

This behaviour limits the saddle-to-scission time, resulting in a simplified physical picture.

In this framework, my PhD. research has been devoted to the study of fission dynamics in the systems of intermediate fissility: 200 MeV $^{32}S +^{100}Mo$ and 180 MeV $^{32}S +^{126}Te$. For these systems, charged particle energy spectra and multiplicities in the pre-scission and evaporation residue channels, as well as cross sections of the two channels, and ER-LCP correlations have been measured using 8πLP apparatus and the electrostatic deflector of LNL coupled to the double-arm TOF spectrometer CORSET, as described in [Tro04]. The TOF spectrometer CORSET [Koz08] has been used to detect fission fragments, allowing to obtain also Mass-TKE and the angular distribution of the fragments. All the observables have been analysed on the base of a dynamical model based on three-dimensional Langevin equations [Kar01]. An analysis in the framework of the statistical model has been also carried out.

Chapter 2

Nuclear models

2.1 Statistical Model

The statistical model in nuclear physics is particularly indicated to describe the reactions that involve heavy compound nuclei [Sto85]. The reason is the following: the compound nucleus is a complex many-body system that, even at low excitation energies, can have a large number of configurations. In particular, the density of states of the CN increases quickly with the excitation energy, becoming very high, with the opening of many decay channels. In this physical conditions, the statistical method not only is appropriate for the description of the system under study, but it is essential to understand and predict many nuclear phenomena.

The statistical model allows to describe the mean properties of hot rotating nuclei, as well as the nuclear decay. About the latter, it is assumed that all the channels are equi-probable and governed by the level density of final states. Therefore, the probability of a decay in a given channel is inversely proportional to the total number of the possible decay channels. The statistical assumption, when combined with the conservation laws and with the principle of detailed balance, leads to the statistical model.

2.1.1 Evaporative decay probability

The starting point to develop a statistical theory of compound nucleus is the *Bohr's independence hypothesis* and the *principle of detailed balance*. The first assumes, when two nuclei fuse together, a redistribution of energy between all nucleons, with a subsequent formation of a thermodynamically equilibrated system. Because the process proceeds through many steps, it is reasonable to assume that the system forgets its formation process, except constants of motion (energy, angular momentum, parity). So the formation

and the decay channels are statistically independent. The *principle of detailed balance* assumes that the transition probability $W_{a \to b}$ of a system from an initial state a to a final state b is related to the probability of the inverse transition $W_{b \to a}$ [Bla52]:

$$\rho_a W_{a \to b} = \rho_b W_{b \to a} \qquad (2.1)$$

where ρ_a and ρ_b are the density of states a and b respectively and $W_{b \to a}$ indicates the transition probability "time-reversed" from b to a.

Using the principle of detailed balance is possible to demonstrate that the probability relative to the emission of a particle i, with energy ϵ_i and orbital angular momentum l_i, from a compound nucleus with energy E_0 and spin J_0 is defined as:

$$P_i(E_0, J_0, (\epsilon_i, l_i), E_1, J_1) \propto \rho(E_1, J_1) T_{l_i}(\epsilon_i) \qquad (2.2)$$

where $\rho(E_1, J_1)$ is the level density of the residual nucleus and $T_{l_i}(\epsilon_i)$ is the transmission coefficient of the inverse process, i.e. of the absorption of the particle i by the residual nucleus. Therefore, one needs to know the level density of the residual nucleus and the transmission coefficient of the inverse process.

2.1.1.1 Level density

The determination of the nuclear level density implies the determination of the number of different ways in which the nucleons ensemble can be arranged in single particle states so the total energy of the system is in the interval [E, E+dE]. The problem is purely combinatorial, the physical aspect enters only in the specification of the single particle states. The starting point is therefore represented by the use of a nuclear model, from which obtain the single particle levels.

Supposing the compound nucleus a system of not interacting fermions, it is possible to obtain the *the Fermi gas level density*. In general, assuming the level density for the states with negative and positive parity are equal, the derivation of the level density formula for a given angular momentum J and both $\pm \pi$ is given by *Bohr Mottelson* [Boh69]:

$$\rho(E, J) = \frac{2J + 1}{12} \sqrt{a} \left(\frac{\hbar^2}{2\Im} \right)^{\frac{2}{3}} \frac{1}{(E - E_{rot})^2} e^{2\sqrt{a(E - Erot)}}, \qquad (2.3)$$

where E_{rot} is the rotational energy and $\Im$ the moment of inertia.

The level density parameter a given by:

$$a = \pi^2 g / 6 \qquad (2.4)$$

where $g = g_p + g_n$ is the sum of the single particle level density of protons and neutrons at the Fermi energy. From many study the values a=A/k, with k ranging from 6 to 12, allow to reproduce the data for composite nuclei in a wide range of mass and excitation energy.

The obvious interpretation of 2.3 is that the rotational energy is not available for the thermal excitation of the system and it does not contribute to the so called *intrinsic level density*.

The spin distribution is often expressed by means of the *spin factor cut-off* σ, where T is the nuclear temperature:

$$\sigma = \frac{\Im T}{\hbar^2} \tag{2.5}$$

Between the empirical level densities, the most known is certainly that of Gilbert-Cameron [Gil65]. The approach consists in the coupling the Back-Shifted-Fermi-Gas (BSFG) to the formula of level density with *constant nuclear temperature*, valid at low energy.

The resulting composite prescription of the nuclear level density is the following.

At high energy the level density at energy E and angular momentum J (both parities) is given by:

$$\rho(E, J) = \frac{\sqrt{\pi}}{12} \frac{e^{2\sqrt{aU}}}{a^{\frac{1}{4}} U^{\frac{5}{4}}} \frac{(2J+1)e^{-\frac{(J+1/2)^2}{2\sigma^2}}}{2\sqrt{2\pi}\sigma^3}, \tag{2.6}$$

where

$$\begin{aligned} U &= E - P(Z) - P(N) \\ \sigma^2 &= 0.0888(aU)^{\frac{1}{2}} A^{\frac{2}{3}} \end{aligned} \tag{2.7}$$

with P(N) and P(Z) the pairing energies. Where the nuclear temperature is given by:

$$\frac{1}{T} = \frac{d}{dU} log(\rho_2) = \sqrt{\frac{a}{U} - \frac{3}{2U}}. \tag{2.8}$$

The model accounts for shell effects, for spherical and deformed nuclei, on the level density parameter [Gil65]; at higher excitation energy, where these effects can be considered negligible, a constant value of the level density have to be used.

At low energy the level density is the following:

$$\rho(E) = \frac{1}{T} e^{\frac{(E-E_0)}{T}} \tag{2.9}$$

where the low energy are considered to be less than E_x being:

$$\begin{aligned} E_x &= U_x + P(Z) + P(N) \\ U_x &= 2.5 + 150/A \end{aligned} \tag{2.10}$$

The parameters T and E_0 are determined imposing the continuity condition of $\rho(E)$ at $E = E_x$.

2.1.1.2 Transmission coefficients

The transmission coefficient introduced in the Eq.2.2 is referred, as already said, to the inverse process, i.e. to the particle absorption by the residual nucleus. On the basis of an analysis in partial waves, the expressions for the elastic and reaction cross sections are:

$$\begin{aligned} \sigma_{el} &= \tfrac{\pi}{k^2} \sum_l (2l+1) \left| 1 - \eta_l \right|^2 \\ \sigma_r &= \tfrac{\pi}{k^2} \sum_l (2l+1)(1 - |\eta_l|^2) \end{aligned} \tag{2.11}$$

where $\eta_l = e^{2i\delta_l}$ with δ_l a complex number that represents the *phase shift* between the outgoing and the ingoing wave and contains all the information relative to the interaction potential; η_l is known as *reflection coefficient*, instead

$$T_l = 1 - |\eta_l|^2, \tag{2.12}$$

represents the probability that an interacting particle produces not elastic processes, among which the fusion represents the inverse process of the evaporation. When the dominant process is the fusion, T_l represents with a good approximation the transmission coefficient describing the evaporation.

The most used method to obtain the transmission coefficients for the evaporation of a light particle from a composite system, leading to a residual nucleus, is based on the analysis of elastic scattering in the system of particle-residual nucleus using the optical model.

In particular, the parameters of the complex interaction potential are determined by the comparison of experimental angular distribution concerning the elastic scattering with the predictions of optical model. From these parameters is possible to obtain the phase-shift δ_l, and therefore the transmission coefficients.

Transmission coefficients for the LCP's evaporation have been also derived by the direct measurement of the cross section of the inverse process, namely the fusion of the light particle with the residual nucleus. In particular, fusion excitation functions for protons and $\alpha-$particles for target nuclei in a wide range of mass $(40 \div 230\ a.m.u.)$ have been measured and analyzed on the basis of a barrier penetration model [Vaz84].

In this framework, transmission coefficients for the particle evaporation can be obtained using the barriers extracted from the fusion systematics and approximating the potential to a parabola. In this approximation the

42

well known formula of Hill-Wheeler for the transmission coefficient can be obtained:

$$T_l(E) = \frac{1}{1 + e^{\frac{2\pi}{\hbar\omega_l}(V_l(R) - E)}} \tag{2.13}$$

where $\hbar\omega_l$ represents the curvature of the barrier:

$$\hbar\omega_l = \left[\frac{\hbar^2}{\mu}\frac{d^2V_l(R)}{dR^2}\right]_{R_{BARRIER}} \tag{2.14}$$

and

$$V_l(R) = V_N(R) + V_C(R) + \frac{l(l+1)\hbar^2}{2\mu R^2} \tag{2.15}$$

where $V_N(R)$, $V_C(R)$ and $\frac{l(l+1)\hbar^2}{2\mu R^2}$ are the nuclear, Coulomb and centrifugal part of the potential, respectively.

2.1.2   Fission probability

In the collision between two heavy nuclei leading to the fusion of the projectile and the target, the CN is produced at high excitation energy and angular momentum. During the decay process shape oscillations will occur due to the antagonist effects of the forces involved. For high values of the angular momenta the dynamical evolution of the shape can lead to an increase of the nuclear deformation till the saddle point configuration is reached.

Once reached this point, the nucleus have a large probability to fission proceeding through the scission configuration. In the framework of a purely deterministic approach the saddle-point represents a point of "no return", i.e. when this point is reached the fission is the only possible evolution of the nucleus.

As mentioned in the first chapter, differently from the evaporative decay channels, the fission probability does not depend on the level density of the residual nuclei [Sto85] (i.e. the fission fragments at infinity distance), instead it depends on the properties of the compound nucleus at the saddle configuration. This corresponds to the maximum of the potential, as shown in the Fig.2.1.

In the figure is also represented the spectrum of intrinsic states at the equilibrium configuration and at the saddle point one, further it is also indicated the possibility of the compound nucleus to deexcite through the emission of a neutron. The fission probability is determined by the level density ρ at the saddle point and by the transmission coefficient through the fission barrier. In the classical approximation (sharp cut-off) T_l is equal to 1 if the total available energy is greater than the fission barrier and 0 otherwise. This is
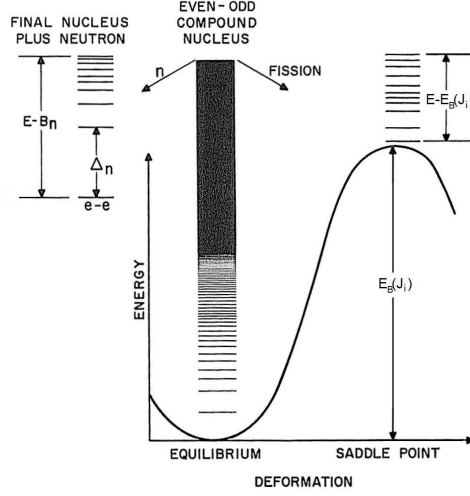
Figure 2.1: Potential as function of the nuclear deformation. The corresponding
level spectrum at the equilibrium and saddle configurations is also
shown, together with the decay by neutron emission.

in generally a good approximation for reactions of fusion-fission induced by
the heavy ions. Therefore, the fission rate for a CN at excitation energy E_i
and angular momentum J_i is given by:

$$R_f(E_i, J_i; E_f, j) \approx \frac{2J_i + 1}{h} \frac{\rho(E_f, j)}{\rho(E_i, J_i)}, \qquad (2.16)$$

where

$$E_f = E_i - E_B(J_i) - \epsilon^s \qquad (2.17)$$

is the thermal energy at the saddle point, with $E_B(J_i)$ fission barrier, E_i is
the initial excitation energies, ϵ^s is the translational kinetic energy of the
nascent fragments and J_i is the initial angular momentum. The factor $2J_i + 1$
arises from a summation over the transmission coefficients, which have been
ste equal to 0 ot 1, and j is the angular momentum of the transition-state
levels.

With the increasing of the angular momentum of the compound nucleus
the fission barrier decreases, making the process more probable. As already
mentioned in the first chapter, the fission rate 2.16 relies on the Bohr-Wheeler
static approach. A more realistic picture, considering the fission as a diffusion
process over the barrier, leads to a reduction of the fission rate by the Kramers
factor: $\left(\sqrt{1 + \eta^2} - \eta \right)$.

44

2.2 Rotating liquid drop model

One of the most important models describing fission is the *rotating liquid drop model* [Coh74], based on an analogy between the properties of nuclear matter and the liquids. Assuming an axial symmetry, the nuclear shape is parametrized through a finite development in Legendre polynomials. The symmetry axis is chosen as a polar axis and the nuclear surface is described specifying the distance $R(\theta)$ from the nuclear center as function of polar angle θ:

$$R(\theta) = R_0 \left(1 + \sum_{l=0}^{l_{max}} \alpha_l P_l(cos\theta) \right) \qquad (2.18)$$

where R_0 is the radius of spherical nucleus. In this description the coefficients α_l of the development 2.18 assume the meaning of collective variables defining the nuclear shape, and the potential energy $E(\alpha_l)$ of the system can be obtained summing three contributions :

$$E = E_S + E_C + E_R, \qquad (2.19)$$

where E_S, E_C and E_R, are respectively the superficial, Coulomb and rotational energy.

The **surface energy** is defined as the area of the nuclear surface multiplied for the γ coefficient of the surface energy:

$$E_S = \gamma \oint d\sigma \qquad (2.20)$$

that is, in the spherical case, equal to:

$$E_S^{(0)} = 4\pi R^2 \gamma = cA^{\frac{2}{3}} \qquad (2.21)$$

with c = $17.9439(1 - Kl^2)$ MeV, K=1.7826, l= neutron excess =(N-Z)/A.

The **Coulomb energy** is defined as the sum of the interactions between the pairs of the volume elements

$$E_C = \frac{1}{2} K \int \int \int \int \int \frac{d\tau_1 d\tau_2}{r_{12}} \qquad (2.22)$$

where K is the square of the (uniform) charge density in the electrostatic case. In the spherical nucleus it becomes:

$$E_C^0 = 0.7053 \frac{Z^2}{A}. \qquad (2.23)$$

The **rotational energy** is given by

$$E_R = \frac{L^2}{2\Im},\tag{2.24}$$

where L is the angular momentum and $\Im = \int \int \int r_\perp^2 \, dr$ is the moment of inertia. In the spherical nucleus it becomes

$$E_R^0 = \frac{L^2 \hbar^2}{2\Im_0} = \frac{1}{2} \frac{L^2 \hbar^2}{\frac{2}{5} M R^2} = \frac{5}{4} \frac{L^2 \hbar^2}{m_0 r_0^2 A^{\frac{5}{3}}},\tag{2.25}$$

where $M = m_0 A$ with $m_0 = 939.15 \frac{\text{MeV}}{\text{c}^2}$ and $R = r_0 A^{\frac{1}{3}}$ ($r_0 = 1.2249$fm) from which

$$E_R^0 = 35.54 \frac{L^2}{A^{\frac{5}{3}}}.\tag{2.26}$$

If α indicates the set of parameters describing the nuclear shape, from the study of the equation $\frac{\partial E}{\partial \alpha} = 0$ the model determines the points of minimum and maximum in the potential energy, which correspond to the stable (equilibrium configuration) and unstable configurations (saddle point configurations) of the system. Within this model two parameters are defined: the fissility (x) and the parameter that gives the measure of angular momentum (y).

The fissility is defined as

$$x = \frac{E_C^0}{2E_S^0} = \frac{1}{50.883(1 - 1.7826 l^2)} \frac{Z^2}{A}.\tag{2.27}$$

The possible values of x are in the range $0 \div 1$: x=1 corresponds to the largest charge that could be sustained by the liquid drop, i.e. it is the limit beyond which the nucleus disintegrates (spontaneous fission), in fact for $x > 1$ no stable configurations exist.

The parameter:

$$y = \frac{E_R^0}{E_S^0} = \frac{1.9249}{1 - 1.7826 l^2} \frac{L^2}{A^{\frac{7}{3}}}\tag{2.28}$$

provides the strength of the centrifugal force that promotes the nuclear fission respect to the cohesive force of superficial tension.

The equilibrium and the saddle-point shapes predicted by the RLDM are shown in Fig. 2.2, for different values of x and y parameters.

Between the predictions of the RLDM of particular importance are the fission barriers, as they determine the probability of the process as shown by 2.16.
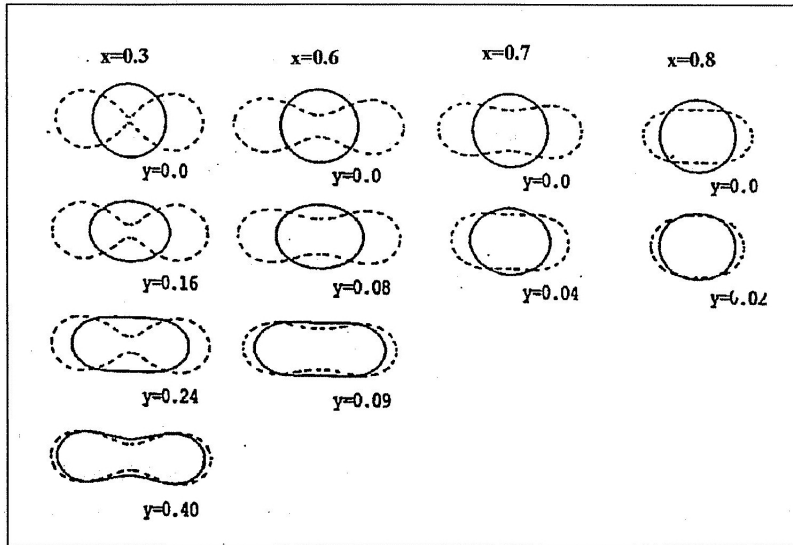
Figure 2.2: Equilibrium (solid lines) and saddle-point shapes (dashed lines) for different values of x and y parameters (from [Coh74]).

Many experimental studies on fission indicate the need to reduce the RLDM fission barriers by a factor in the range $0.5 \div 0.9$ for nuclei with mass $A \leq 200$ in order to reproduce the fission cross sections.

An improvement of RLDM is constituted by the rotating liquid drop model with finite range (FRLDM) [Sie86]. It takes into account the finite range of the nuclear forces and the diffuseness of the nuclear surface in the potential energy of the nucleus.

This model predicts fission barriers lower than those provided by the RLDM one for $A \leq 200$ as shown in the Fig.2.3, where the fission barriers at $L = 0$ predicted by the two models are shown with the experimental results. The FRLDM reproduces the experimental values with an uncertainty of $\pm 1 MeV$. The same model allows to reproduce also the mass distributions of the fission fragments. The same difference between the predictions of the two models is found for all the angular momenta L > 0.

2.3 The statistical model simulation codes: Lilita and PACE2

As already mentioned, the statistical model has been in these last years the base for the study of nuclear reactions that proceed through the formation of a compound nucleus. Different codes have been developed that provide the
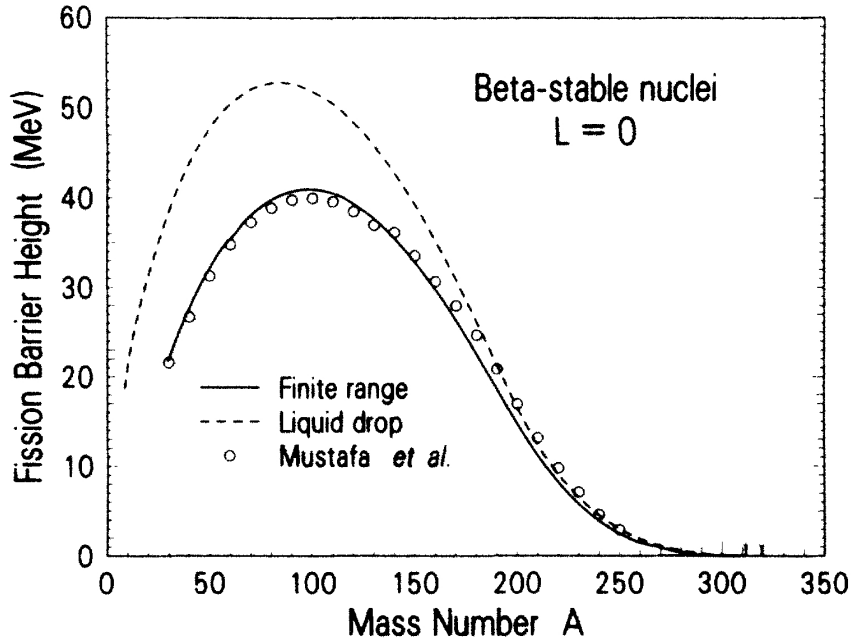
Figure 2.3: Calculated fission barrier heights as function of mass number for beta-stable nuclei in the RLDM and FRLDM (dashed and solid lines, respectively). The open circles are experimental points (from [Sie86]).

energy spectra, the angular distributions, the multiplicities of evaporated particles and the fission cross sections.

In the present work we have used two statistical model codes: Lilita_N97 and Pace2_N97. Both are multi-step codes based on the Monte-Carlo technique.

The program LILITA [Gom81] allows to simulate the decay of a composite nucleus in the evaporation residue channel. The basic physics of LILITA is contained in the expression 2.3 for the level density and in the transmission coefficients derived from the optical model or from fusion systematics.

The original program LILITA has been extensively modified from the group of Naples, in order to introduce new options, the new version is Lilita_N97.

The evaporative code PACE2 (Projection Angular-momentum Coupled Evaporation) [Gav80] simulates the deexcitation of CN both through the evaporation and the fission.

The emission probability of particles is calculated using the expression of the Fermi gas level density in the prescription of Gilbert-Cameron in a modified version. Transmission coefficients from OM and FS can be used.

The fission probability is calculated on the basis of fission barriers from the FRLDM of [Sie78].

48

The program PACE2 has been modified to take into account for the fission delay time τ_{d} as already done by other authors. In particular, the program simulates the time interval where the fission does not compete with the particle emission assuming:

$$\Gamma_f = f(t)\Gamma_{BW}. \qquad (2.29)$$

Two different functions $f(t)$ can be used [ref32mio]: either a simple step function with f(t)=0 for t $< \tau_{\mathrm{d}}$ and f(t)=1 for t $> \tau_{\mathrm{d}}$, or an exponential-type function of the form:

$$f(t) = 1 - exp(-t/\tau_d). \qquad (2.30)$$

The Kramers statistical reduction of Γ_{f} can be also used in the code.

2.4 Three dimensional Langevin equations for the study of fission dynamics

In the stochastic approach of fission based on Langevin equations, the evolution of collective coordinates is considered as motion of Brownian particles. In particular, during the collision the internal degrees of freedom of the collision partners are excited. They are assumed to equilibrate rapidly, and their effect on the relative motion is simulated by the action of a "heat bath" as in the theory of Brownian motion.

The evolution of the system is described by the action of conservative, frictional and fluctuating forces. The basic concepts underlying this approach can be easily understood considering the one dimensional Langevin equation, already mentioned in the first chapter:

$$M\ddot{R} = \tilde{F}(R) + F_{frict}(R, \dot{R}) + F_L(R, t) \qquad (2.31)$$

where R is the collective variable.

$\tilde{F}(R)$ represents the conservative force, whose potential is derived from nuclear macroscopic model as the RLDM;

$F_{\mathrm{frict}}(R, \dot{R}) = -\gamma(R) \cdot \dot{R}$ is the friction force, with $\gamma(R)$ friction coefficient;

$F_{\mathrm{L}}(R, t) = \sqrt{D(R)}\Gamma(t)$ is the Langevin force, where $D(R)$ represents its intensity and depends on the friction coefficient $\gamma(R)$ and the nuclear temperature T with the relation:

$$D(R) = \gamma(R)K_B T, \qquad (2.32)$$

where K_{B} is the Boltzmann constant. This expression states the common origin of frictional and fluctuating forces in the Langevin approach.

49
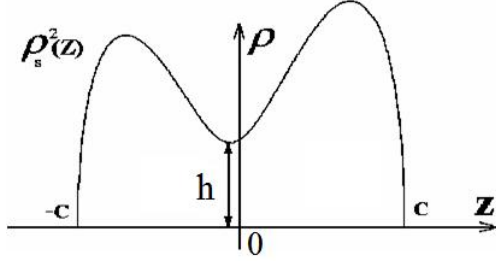
Figure 2.4: Nuclear shape in cylindrical coordinates ρ_s, z together with h, c parametrization.

This is a simple consequence of the fact that the frictional and Langevin forces both have their origin in the coupling between the relative motion and the bath. The relation 2.32 is a special case of the fluctuation-dissipation theorem; in the statistical theory it can be shown that such relation exist quite generally.

The random part $\Gamma(t)$ is modeled as a Gaussian white noise with the properties $< F(t) >= 0$ and $< \Gamma_i(t)\Gamma_i(t') >= \delta_{ij}\delta_c(t - t')$, this term causes fluctuations of the collective variables.

In the present work the data for the composite nuclei ^{132}Ce and ^{158}Er, have been compared with the predictions of a dynamical model based on the three dimensional Langevin equations. Starting from a spherical configuration, characterized by a thermal equilibrium and an angular momentum, this model simulates the decay in the FE and FF channels.

During the stochastic process, light particles are emitted by the composite system. The competition between FF and FE channels is governed by the strength of the friction and random force, which determine the shape fluctuations in the phase space, as well as by the light particle emission, which reduces the excitation energy and the angular momentum of the system.

Shape parametrization

Nuclear shapes are described by the (c,h,α) parametrization [Pau73]. The c variable represents the nuclear elongation, as shown in the figure 2.4 in cylindrical coordinates (ρ_s and z). The variable h is the radius of the neck, that is produced by the dynamical process and corresponds in the figure to the central part of the nuclear shape. The mass asymmetry parameter α is related to the mass (volume) ratio of forming fragments:

$$\frac{A_1}{A_2} = \frac{V_1}{V_2} = \frac{1 + \frac{3}{8}\alpha}{1 - \frac{3}{8}\alpha} \tag{2.33}$$

which is defined as the ratio of the volumes of two parts of the nucleus obtained when the latter is intersected by the plane z=0. The surface of the nucleus in cylindrical coordinates, is given by:

$$\rho_s^2(z) = \begin{cases} (c^2 - z^2)(A_s + Bz^2/c^2 + \frac{\alpha z}{c}), & B \geq 0 \\ (c^2 - z^2)(A_s + \frac{\alpha z}{c})exp(Bcz^2), & B < 0 \end{cases} \quad (2.34)$$

where z is the coordinate along the symmetry axis and ρ_s is the radial coordinate of the nuclear surface. The quantities B and A_s in Eq. 2.34 are defined as:

$$B = 2h + \frac{c-1}{2}$$

$$A_s = \begin{cases} c^{-3} - \frac{B}{5}, & B \geq 0 \\ -\frac{4}{3}\frac{B}{exp(Bc^3)+(1+\frac{1}{2Bc^3})+\sqrt{-\pi Bc^3}erf(\sqrt{-Bc^3})}, & B < 0 \end{cases} \quad (2.35)$$

In the symmetrical case $\alpha = 0$ a family of symmetric shapes is obtained, ranging from the spherical shape (c=1, h=0) to the two-fragment shapes ($A_s < 0$). For the case of $\alpha \neq 0$ different asymmetric shapes are obtained.

The appearance of a neck in the nuclear shape is associated with the instant at which the profile function $\rho_s(z)$ starts to have three extrema, two maxima corresponding to nascent fragments and a minimum between them, which corresponds to the neck thickness.

The equation for the scission surface can be written in the form

$$\rho_s(z_N) = R_N \quad (2.36)$$

where R_N is the neck radius corresponding to the pre-scission shape. Different estimate for R_N has been adopted. The hydrodynamic scission criterion [Bro90] has the form $R_N = l/11$, where l is the length of the nucleus. In the simulations performed in the present work the criterion $R_N = 0.3R_0$, where R_0 is the radius of the spherical nucleus, has been used. This prescription has been obtained on the base of a theoretical systematic study [Nad05].

The collective coordinates $\mathbf{q} = (q_1, q_2, q_3)$, are connected with the shape parameters c, h and α by: $q_1 = c$, $q_2 = (h + 3/2)/(\frac{5}{2c^3} + \frac{1-c}{4} + \frac{3}{2})$, and $q_3 = \alpha/(A_s + B)$ if $B \geq 0$, or $q_3 = \alpha/A_s$ if $B < 0$.

Langevin equations

The multi-dimensional Langevin equations have the form:

$$\begin{aligned} \frac{dq_i}{dt} &= \mu_{ij}p_j \\ \frac{dp_i}{dt} &= -\frac{1}{2}p_j p_k \frac{\partial \mu_{jk}}{\partial q_i} - \frac{\partial F}{\partial q_i} - \gamma_{ij}\mu_{jk}p_k + \theta_{ij}\xi_j(t) \end{aligned} \quad (2.37)$$
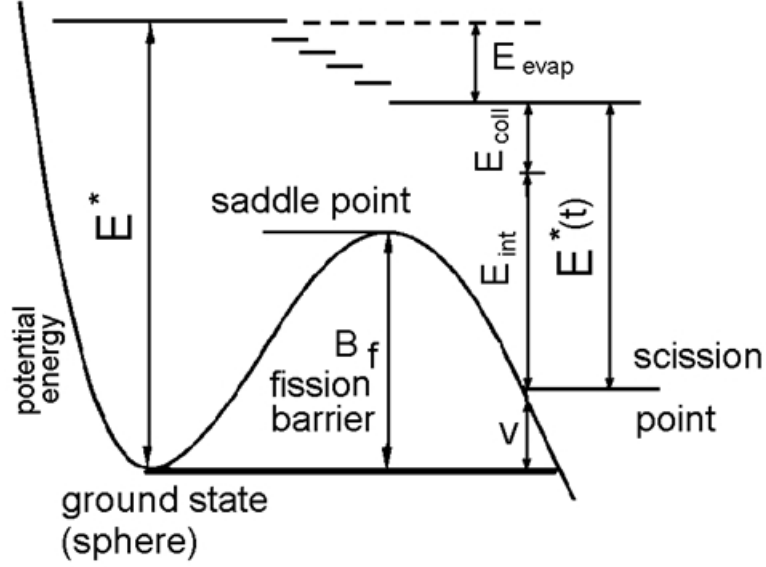
Figure 2.5: Schematic diagram of the energies involved in the fission process.

where $\mathbf{q} = (q_1, q_2, q_3)$ is the vector of the collective coordinates, $\mathbf{p}$ is the vector of the conjugate momenta. The first term of the second equation represents the kinetic energy of the collective degrees of freedom. Where μ_{jk} are the elements of the inertia tensor. $F(\mathbf{q}) = V(\mathbf{q}) - a(\mathbf{q})T^2$ is the Helmholtz free energy, where $V(\mathbf{q})$ is the conservative force from the FRLDM. The third term is related to the dissipated energy where $\gamma_{ij}(\mathbf{q})$ is the friction tensor, assuming one or two-body dissipation. The normalized random variable $\xi_j(t)$ is assumed to be a white noise. The strength of the random force θ_{ij} satisfies the relation $\sum \theta_{ik}\theta_{kj} = T\gamma_{ij}$. The temperature T of the nucleus, that constitutes the heat bath for the collective variables, has been determined by the Fermi-gas model formula $T = (E_{int}/a)^{1/2}$, where a is the level density parameter and E_{int} is the internal excitation energy of the nucleus calculated on the basis of the energy conservation

$$U = E_{int} + E_{coll} + V(q) + E_{evap}(t) \qquad (2.38)$$

where U is the total excitation energy, $E_{coll} = 0.5\sum \mu_{ij}p_ip_j$ is the kinetic energy of the collective degrees of freedom and $E_{evap}(t)$ is the energy carried away by the evaporated particles at the time t. The repeated indices in the equations above imply summation over the collective coordinates.

In the figure 2.5 is showed a diagram of the energies present in the expression 2.38.

To have a realistic simulation of the evaporated light particles from the CN the code Lilita_N97 has been coupled with the dynamical one. The code
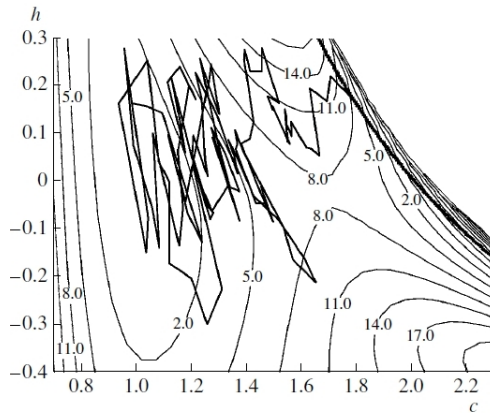
Figure 2.6: Stochastic Langevin trajectory in the space of the collective coordinates $(c, h, \alpha = 0)$. The numbers at the isolines specify the values of the potential energy in MeV. The solid thick line in the right upper corner of the figure is the scission line. The trajectory given in this figure represents a fission event (from [Ade05]).

allows to simulate a large amount of measured observables in a consistent way having all the characteristics required to improve the simulation, as required in many previous work [Hil92, Wad93].

2.4.1 Langevin trajectories

It is interesting to follow a Langevin trajectory simulated by the code, starting from the initial conditions.

When starting modeling fission dynamics assuming a spherical nucleus, i.e. $\mathbf{q}_0 = (c_0 = 1.0, h_0 = 0.0, \alpha_0 = 0.0)$ the initial state is assumed to be characterized by the thermal equilibrium and an angular momentum generated from a triangular spin distribution using the Monte Carlo technique.

The potential energy, as well as the transport coefficients of the Langevin equations, have been calculated on the uniform three-dimensional grid with $151 \times 101 \times 51$ grid points where $c \in [0.7, 3.7]$, $h \in [-0.6, 0.4]$, and $\alpha \in [-1, 1]$. Interpolation between the grid points has been performed using the Lagrange formulas.

The nucleus starts its trajectory moving around the initial spherical shape and such path can be very long in terms of time. To contain the computing time after a fixed period the calculation switches from the dynamical to the static calculation, using the statistical model.

In Fig. 2.6 is represented a fission trajectory in the space of collective coordinates c-h for $\alpha = 0$. The scission configurations, determined by the
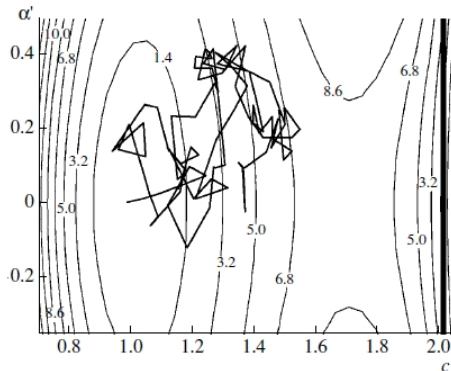
Figure 2.7: The same as in Fig. 1 but in the collective coordinates $(c, h = 0, \alpha)$. The trajectory shown in this figure represents the formation of an evaporation residue (from [Ade05]).

criterion mentioned in the previous paragraph, are represented with a thick solid line; when a nucleus overcomes this limit it will undergo fission. In Fig. 2.7 is represented an evaporation trajectory, in the space c-α for h=0, the scission configurations are represented with the thick solid line; in this case the nucleus does not reach this limit, so it will decay in the FE channel. During the path starting from the spherical shape at every step $\Delta t = 10^{-25}$s the code calculates all the information concerning the shape, the excitation energy and the angular momentum of the nucleus. The angular momentum, the excitation energy and the values of A and Z are transferred to the program Lilita_N97 that calculates the probability of light particle emission. The evolution of the process continues until the scission point is reached or the available energy is not enough for emission of light particle or the maximum time is overcame.

As a result of the calculation one will obtain an ensemble of stochastic Langevin trajectories, each of them describing fission or evaporation events. In the case of fission, the scission configuration for each event is determined by the intersection point of the stochastic Langevin trajectory of the fissioning system with the scission surface in the coordinate space. Thus it is possible to introduce the notion of a mean trajectory and mean scission deformation, obtained by averaging over an ensemble of Langevin trajectories. The mean trajectory will correspond to the symmetrical shapes. Examples of mean trajectories obtained in the three-dimensional Langevin calculations are presented in Ref. [Kar01].
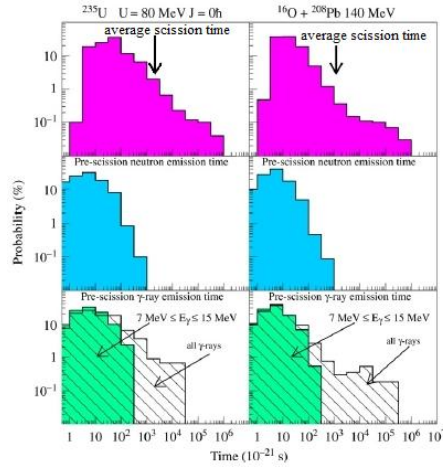
Figure 2.8: Distributions of scission times (upper panel), neutrons emitted prior to scission (middle panel) and GDR $\gamma-$rays emitted prior to scission (lower panel) (from [Gon02]).

2.4.2 Time distribution

Dynamical models, as those based on Langevin equations, provide time distribution of the fission process. As a general behaviour, these time distributions have a peak at about 10^{-20} s with a long tail towards even larger lifetimes of 10^{-19} s to 10^{-17} s. This behaviour is shown in Fig.2.8, where the scission time distributions have been calculated for an excited uranium nuclei without spin (left column) and for excited thorium nuclei with spins resulting from fusion reactions.

These distributions are much broader than those of pre-scission neutron and already for the average scission times, indicated by arrows. Therefore, pre-scission neutron probes only part of the scission time distributions and the average statistical times inferred are smaller than the real average fission time. By contrast pre-scission $\gamma-$rays cover nearly the whole scission time distribution (hatched area). However, to discriminate GDR $\gamma-$rays emitted by the nucleus before scission from those emitted by fission fragments, a selection on the $\gamma-$ray energies has to be applied. Its effect is shown in the lower panels of Fig.2.8 for a typical energy selection between 7 and 15 MeV (green area): pre-scission $\gamma-$rays emitted at long times have low energies and are removed by the selection. Therefore, the pre-scission $\gamma-$rays are not sensitive either to the long scission times. Quite similar qualitative conclusions have also been reached from pure statistical calculations, including Kramers' width reduction with friction parameters $\beta > 2 \times 10^{21} \mathrm{s}^{-1}$.

This implies that the estimates of the fission delay performed with the

SM, within the phenomenological approach, doesn't represent the real mean fission time. In particular, the pre-scission light particles emitted provide an estimate of the transient time as already pointed out in the first chapter. As neutrons have been found to be emitted after the charged particles and considering that the emission is distributed on more than 1 step, because of the high multiplicity, somewhat larger values than the transient time are expected.

In spite of these limitations, it must be pointed out that a good agreement between the data and the predictions of the dynamical model, make one confident that the entire time distributions provided by the model represents the reality. In this respect, the constraints to the model are crucial. As mentioned, the systems of intermediate fissility, as those studied in this work, are particular suited for such a study, as they allow to put severe constraints to the model.

Chapter 3

Experimental set-up and data analysis of 200 MeV $^{32}\mathrm{S} +^{100}\mathrm{Mo}$ and 180 MeV $^{32}\mathrm{S} +^{126}\mathrm{Te}$ systems

This chapter is dedicated to the illustration of the experimental apparatus and the techniques to carry out the experimental data. The chapter is closed summarizing all the measured quantities for $^{32}\mathrm{S} +^{100}\mathrm{Mo}$ and $^{32}\mathrm{S} +^{126}\mathrm{Te}$ experiments, which represent the strong point of these works concentrated on intermediate fissility systems.

3.1   Beam characteristics

The experiments on the reactions $^{32}\mathrm{S} +^{100}\mathrm{Mo}$ and $^{32}\mathrm{S} +^{100}\mathrm{Te}$ were performed at the XTU Tandem-ALPI Superconducting LINAC accelerator complex of the Laboratori Nazionali di Legnaro (LNL). A pulsed beam of $^{32}\mathrm{S}$ at 200 and 180 MeV were produced by the XTU Tandem. The repetition rate was 800 ns and the duration was about 3 ns for both the reactions. The intensity was kept between 1-3 enA. The target of $^{100}\mathrm{Mo}$ was self-supporting 400 μg/cm^2 thick and the target $^{126}\mathrm{Te}$ was 300 μg/cm^2 thick on a backing $^{12}\mathrm{C}$ of 15 μg/cm^2.

3.2 8πLP apparatus

The 8πLP apparatus is used to detect light charged particles (LCP), fission fragments and evaporation residues (ER). The trigger system is flexible enough to allow the design of complex trigger logics. In particular, fission fragments and ER are used as a trigger for exclusive measurements, namely
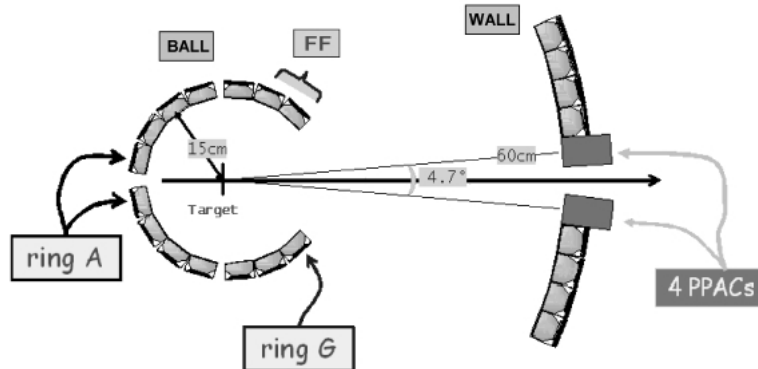
Figure 3.1: 8πLP detector.

LCP in coincidence with fission fragments and ERs. As it will be shown later, the extraction of the LCP multiplicities does not require the individual normalization of the FF and FE inclusive channel.

3.2.1 LCP detectors

The 8πLP detects LCP (protons, deuterons, tritons and $\alpha-$particles) with an angular coverage of about 80% of the total solid angle, with low identification threshold and high granularity. These properties allow the measurement of high precision energy spectra and angular correlations on a large number of angles, also in the case of processes with low cross sections, e.g. pre-scission LCP emission.

8πLP consists of two detector subsystems, each made of two-stage telescopes: the Wall and the Ball. The Wall contains 112 telescopes and is placed at 60 cm from the target. Each of the Wall telescopes consists of a 300μm Si detector backed by a 15 mm Csi(Tl) crystal and has an active area of 25 cm^2 which corresponds to an angular opening of about 4º. The Wall covers the angular range from 2º to 24º. The Ball has a diameter of 30 cm and consists of 7 rings placed coaxially around the beam axis. Each ring contains 18 telescopes and covers an angular opening of about 20º. The telescopes of the Ball are made of a 300μm Si detector mounted in the flipped configuration (particle entering from the Ohmic side) backed by a 15 mm CsI(Tl) crystal. The Ball has a total of 126 telescopes and covers the angular range from 34º to 165º. The rings are labeled from A to G going from backward to forward angles. For geometric reasons, the Ball telescopes have four different shapes with an active area ranging from 7.2 cm² to 17.8 cm², and cover solid angles from 32 msr to 79 msr.

Particle identification is carried out by the $E - \Delta E$ method for the ions

that are stopped in the E stage. The particles stopping in the first stage are identified by the TOF method in the case of the Wall telescopes, and by the Pulse Shape Analysis (PSA) technique in the case of the Ball telescopes. In this configuration Ball and Wall arrays can detect protons and $\alpha-$particles with energies grater than 1 MeV and 3 MeV (energy thresholds) respectively.

3.2.2 LCP identification

To identify the charged ions that enter the telescopes two different techniques have been adopted $E - \Delta E$ and $\Delta E - t$.

When the particles (protons, deuterons, tritons and $\alpha-$particles) have enough energy to go through the Si first stage of the telescope the identification is carried out with the $E - \Delta E$ technique. ΔE represents the energy lost in the first detector of the telescope. From the Bethe-Block model is known that:

$$\frac{\Delta E}{\Delta x} \propto \frac{M Z^2}{E} \tag{3.1}$$

where M, Z and E are mass, charge and initial energy of the particle, respectively. Δx is the detector thickness of the first stage of the telescope. From this it follows that in the matrix $E - \Delta E$, and equally, in the $E_R - \Delta E$ (E_R is the residual energy in the second stage of the telescope), the particles with different charge or different mass are placed in different hyperbola branches.

A typical matrix collected with a telescope during an experiment with $8\pi LP$ is shown in Fig.3.2. There are four regions which correspond to four different kinds of particles: protons, deuterons, tritons and $\alpha-$particles . This method requires that the particle must have enough energy to pass through the ΔE stage of the telescope.

The second identification technique concerns with the particles that stop in the ΔE stage (e.g. protons with energy $E_p \leq 6$ MeV or $\alpha-$particles with $E_\alpha \leq 25$ MeV and fission fragments). A different method is used for the Wall and for the Ball telescopes. The Wall detectors are about 60 cm from the target. Consequently, the particles that stop in the ΔE stage can be identified by correlating the total energy lost (in this case ΔE is the total energy) and the TOF. The TOF is extracted directly by the time measured by the TDC. In fact, the start of the TDC is generated by the Si detector, and the stop by the RF signal.

The technique of TOF is based on the measurement of the time t, spent by the particle to span the distance L between the target and the detector, and its energy $E = \Delta E$. The connects between the TOF and the particle
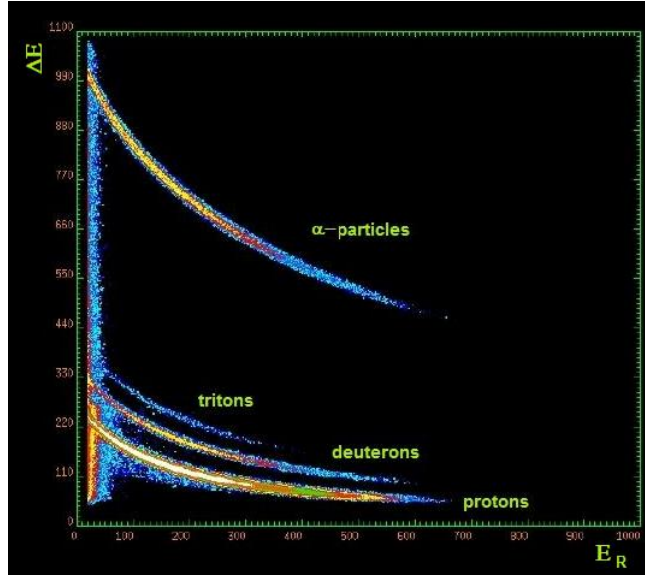
Figure 3.2: $E - \Delta E$ matrix used to identify light particles with higher energy using both the detector stages of the telescopes.

mass is the following relation:

$$t = L\sqrt{\frac{M}{2\Delta E}}. \tag{3.2}$$

In the matrix $\Delta E - t$ the events concerning particles with different masses are clustered in different regions of the matrix and can be identified.

In the case of the Ball telescopes, the flight path of only 15 cm is not enough to allow the separation between particles, due to the poor time resolution of the signal coming from the ΔE Si stages . To overcome this problem the pulse shape analysis of the signal [Pas99] was chosen. The PSA technique is based on the difference in the rise time for particles having different stopping power. In fact the total charge collection time reflects the rise time of the output signals. The discrimination is enhanced if particles are impinging on the ohmic side (generally named "rear side"). This is due to the lower electric field in the entrance region and the lower velocity of the holes which are mainly responsible for the signal pulse formation. To perform PSA the Ball Si detectors are mounted with the rear side facing the target. From the electronics point of view, the PSA was obtained using the same electronics as the TOF, but changing the fraction and the internal delay of the CFD to have an output timing signal sensitive to the rise time of the input signal.
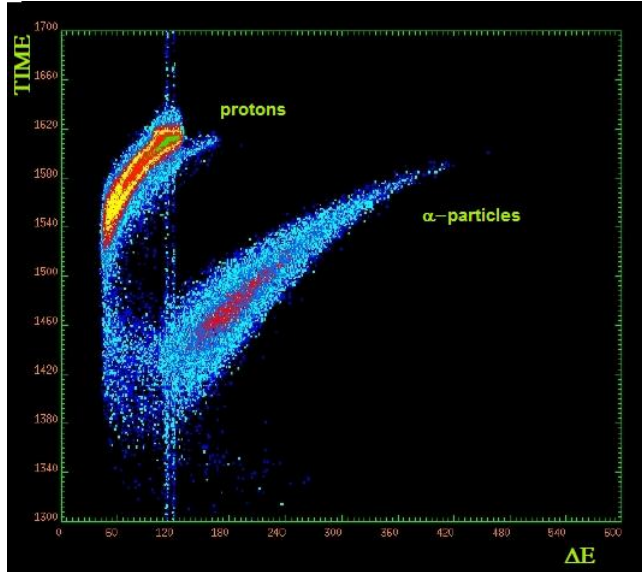
Figure 3.3: Matrix used to identify the light particles in the silicon detector, the first step of the telescope.

3.2.3   Fission Fragments identification

Heavier charged fragments stop on the first stage of the telescopes and can be identified in the telescopes of the Ball by the PSA technique. LCP and FF events are however characterized by different ranges of energies. By using two separate amplifiers we can adjust the gain to allow the heavy fragments energy signals to access the dynamical range of the ADCs. In Fig. 3.4 a typical $\Delta E - t$ matrix is shown. In this case the energy is obtained with the lower gain.

The PSA technique allows the separation between heavy fragments and light particles stopping in the same detector but does not provide any information about the mass or charge of the fragments. The selection between symmetric and asymmetric mass splitting can nevertheless be achieved on a kinematics ground. Fission fragments are sorted out of the possible binary reaction products by means of the fragment-fragment coincidences. An example of such a selection for the reaction $^{32}S +^{100} Mo$ is in Fig.3.5.

The figures shows fragment-fragment energy correlation corresponding to two fragments detected by two opposing telescopes (namely, opposite side of the beam and in the same plane of the beam direction) in the same ring F (a), in the same ring G (b) and in the rings F-G (c). The plots show clearly the transition between the symmetric and asymmetric mass splitting by a proper choice of the detecting geometry, which means, a variable coverage of the

61
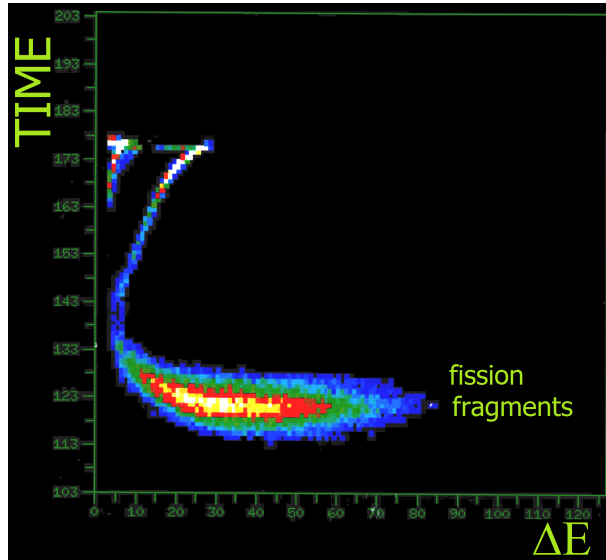
Figure 3.4: Matrix used to identify fission fragments stopped in the silicon detector, the first step of the telescope.
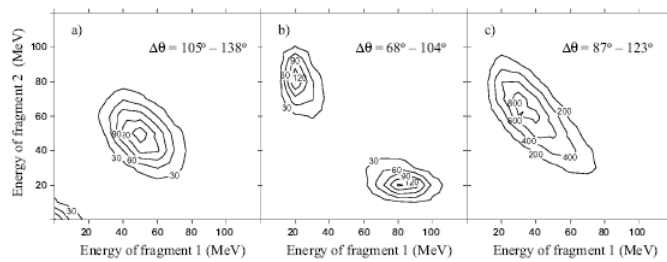
Figure 3.5: Energy-energy correlation matrix of the measured fragments: a) both fragments in ring F, b) both fragments in ring G, c) one fragment in ring F and the other in ring G.

folding angle. The angular correlations are such that when the two fragments are detected in two different telescopes of the ring F, which corresponds to a folding angle $\Delta\theta$ between 105º and 138º, only the symmetric component of the fragment mass distribution is detected; in the case of ring G instead, only the most asymmetric component is selected. The case of rings F and G corresponds to an intermediate condition, namely to an angular range centered on the most probable folding angle for symmetric fission.

3.2.4 LCP detector calibrations

Since the first stage is a Si detector and the second stage is a CsI detector we have to employ different methods of calibration.

A Si detector has a linear response with energy, independently on the kind of impinging particle. Hence, it is possible to calibrate it by means of a radioactive source and a high precision pulse generator. The CsI detector calibration is more complex due to the fact that the response is dependent on the type of particle. This means that an independent calibration is necessary for protons and $\alpha-$particles .

In order to calibrate the Si detector we have used a ^{241}Am source (that emits $\alpha-$particles at the energies E=5.484 MeV and E=5.435 MeV) coupled with an high precision pulse generator, whose signals are sent to each pre-amplifiers. This procedure is applied to the first stage of all telescopes.

The energy calibration of CsI is accomplished by using the events that are recorded during the experiment along with the Si detector calibration and the knowledge of the thickness of the Si detector coupled to the CsI detector.

The algorithm of proceeds in the following way. First, particles are identified in Z and A in the $\Delta E - E_R$ matrix and $\Delta E - E_R^{calc}$ tables are computed from a model that implements the energy loss in absorbers. E_R^{calc} is the energy lost calculated from such a model for each Si detector, given its thickness and the type of particle. In the second step, for each value of the measured energy lost ΔE^{exp} the residual energy is computed from the $\Delta E - E_R^{calc}$ table and a set of (E_R^{calc}, E_R^{exp}) couples is built. At this step E_R^{calc} is in MeV units and E_R^{exp} is in arbitrary units (the ADC channel). In the third and final step a polynomial fit to the couples (E_R^{calc}, E_R^{exp}) provides the calibration searched. This methods has been verified against other direct methods and by substituting the CsI with a Si detector independently calibrated with an α source.

3.2.5 Evaporation Residue detectors

In the 8πLP setup up it is also possible to detect ER. The Wall detectors between 2.5º and 7.5º around the beam axis are in fact replaced by four
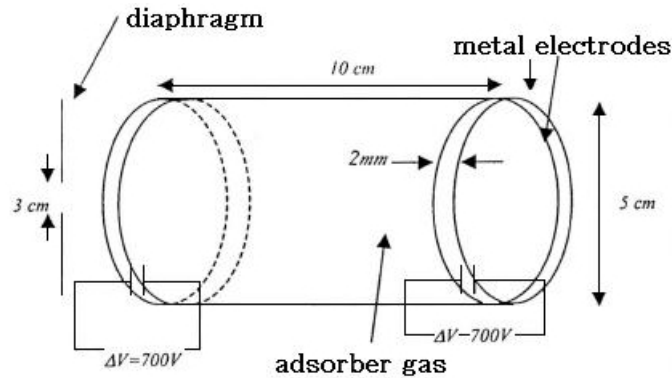
Figure 3.6: Parallel plates avalanche counters used for evaporation residues detection.

Parallel Plate Avalanche Counter (PPAC) modules, each one subtending a solid angle of about 0.3 msr. Each module, identified as PPAC UP, DOWN, LEFT and RIGHT, consists of two coaxial PPACs mounted and operating in the same gas volume at a distance of 10 cm from each other (seeFig. 3.6). By adjusting the gas pressure, it is possible to stop the ER between the two PPACs, and let the fission fragments and elastic scattered ions to impinge on the second PPAC. This is due to the combined effect of higher charge state and lower velocity of the ER with respect to the fission fragmens and the beam ions. Consequently, ER are sorted out from the first PPAC signals using the signals from the second PPAC as a veto. The acquisition of a ER event is started by the signal of the first PPAC vetoed by the second PPAC signal. The time difference between this signal and the RF provides the TOF of the ER.

In the ^{32}S $+^{100}$ Te experiment the four PPACs were replaced by a new module which contains two large area PPACs, one in the front and the other in the back to use the same principle as before. Each PPAC is divided in 18 slices. By using a front mask it is possible to modify the solid angles covered. Also the gas between the two PPACs has been replaced by a solid absorber. This allows to choose independently the optimal operational gas pressure for the PPAC and the optimal absorber thickness for stopping the ER.

The suppression of the elastic events allows to mount a detecting system for ER in an angular range where the elastic channel has a large production rate. This results in a PPAC rate sustainable by the acquisition system.

3.2.6 Electronics and trigger

The signals produced by the particles crossing the detectors are sent to the pre-amplification circuit and later to the amplification one. The CsI pre-amplifiers are directly connected to the photo-diodes, i.e. positioned in the vacuum chamber to reduce the noise produced by the cabling capacities.

The amplifiers produce a *slow* signal (with a shaping time of 1 μs) which is sent to the Analog to Digital converter (ADC) to acquire the energy parameter, and a *fast* signal to extract the time parameter of the event. The latter is sent to a *Constant Fraction Discriminator* (CFD) that produces the start signal for a *Time to Digital Converter* (TDC) working in the *Common Stop* (CS) configuration.

The ADC and TDC are read by the read-out system enabled by the *Master Trigger* (MT) signal. The MT is produced by a coincidence between the conditions imposed by the typology of the events and the signal of the accelerator radio frequency (RF) used as a time reference. A further task of MT is the production of the CS for the TDC modules. This coincidence synchronizes the data acquisition and the arrival of a beam bounce on the target.

The trigger is a complex circuit whose main function is to select specific events among all measured: the logic scheme is shown in Fig.3.7.

The MT signal is produced by an OR logic circuit between 8 different possible types of events:

1. **PPAC AND Wall**: a signal from any one Wall detectors in coincidence with a signal from any one PPAC;

2. **PPAC AND Ball**: a signal from any one Ball detectors in coincidence with a signal from any one ER detectors;

3. **Ball/div**: a signal fraction from any one Ball detectors;

4. **PPAC/div**: a signal fraction from any one ER detectors;

5. **Wall/div**: a signal fraction from any one Wall detectors;

6. **(F OR G) AND Wall**: a signal from any one detectors of F-G rings in coincidence with a signal from any one Wall detectors;

7. **(F OR G) AND Ball**: a signal from any one detectors of F-G rings in coincidence with a signal from any one Ball detectors;

8. **PPAC.nv/div**: a signal fraction from any one ER detectors with and without veto condition.
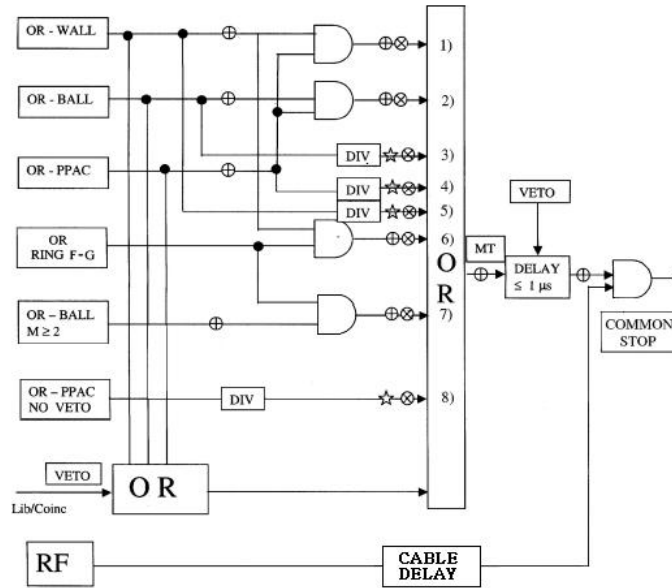
Figure 3.7: Trigger conditions used in the reaction of ^{32}S $+^{100}$ Mo.

The items 1) and 2) refer to the FE process events. Here at least one LCP hits a Wall or Ball detector and at the same time an ER hits one of the PPACs.

The items 3), 4), 5) and 8) allow to acquire inclusive events, i.e. all the single events that hits any one detectors without any condition. Their rates are individually downscaled by a factor set during the experiment. The inclusive measurement is a useful tool to monitor the correct working of the system, and is essential for the determination of the multiplicities. These dividers allow to balance the acquisition rate with respect to the coincidences, thus avoiding to overload the acquisition system and reducing the dead time.

Finally, the items 6) and 7) allow the acquisition of the fragment-fragment and fragment-fragment-particle events, which represent the FF reaction events with and without emission of pre- or post-scission particles.

Each event carries the information about:

- acquisition times and energies of the LCP and fission fragments;

- TOF for the ER;

- trigger pattern that has enabled the MT.

All this information is acquired with an hardware apparatus, the further processing via software allows to reconstruct all the details of the recorded events.

3.3 Analysis of the Fusion-Evaporation channel

To obtain the LCP spectra in coincidence with the ERs, the angular correlation LCP-ER and the LCP multiplicities, the elementary data stored during the experiment have been elaborated. Each event is made of several parameters that include the information with respect to the energy and time of detected ions. The first stage of the analysis consists in the reading of the data from the disk and making of a data-base in which the different kinds of events and their frequency are ordered [Var89].

The technique of elementary data ordering is particularly effective because reduces significantly the space on the disk and also the time needed for the analysis. The N parameters that characterize every event define a N-dimensional space, the event space, and the representative event points describe an hypersurface in this space. The projection of this hypersurface on a generic axis corresponds to the particle spectrum. The projection of the hypersurface on two fixed generic axes produces a matrix. Each element of the matrix represents the number of times that the specific point, characterized by the value of the x and y coordinates, occurs.

The data-base is read by a second program called VISM. It allows the building and visualization of the spectra and matrices assuming different conditions on each parameter, the identification of ER, fission fragments or charged particles, and to impose coincidence conditions.

In a first step the TOF spectra of the PPAC without coincidence conditions are built. In Fig.3.8 a TOF spectrum measured in single by a PPAC in the ^{32}S $+^{100}$ Mo reaction is shown. Two peaks are present: the first, at lower time, is due to the evaporation residues; the second is produced by the elastically scattered ions. It is important to say that the TOF spectrum represented in the figure does not correspond to the physical time spent by ions to travel from the target to the detectors. In fact, the elastically scattered ions have an higher velocity than the ERs; then they need less time to span the same distance. The time inversion in the spectrum is produced by the CS logic used by the TDC (see previous paragraph). In particular, the value produced by the TDC corresponds to the time interval between the CS signal and the start given by the ER or elastically scattered ion that has not
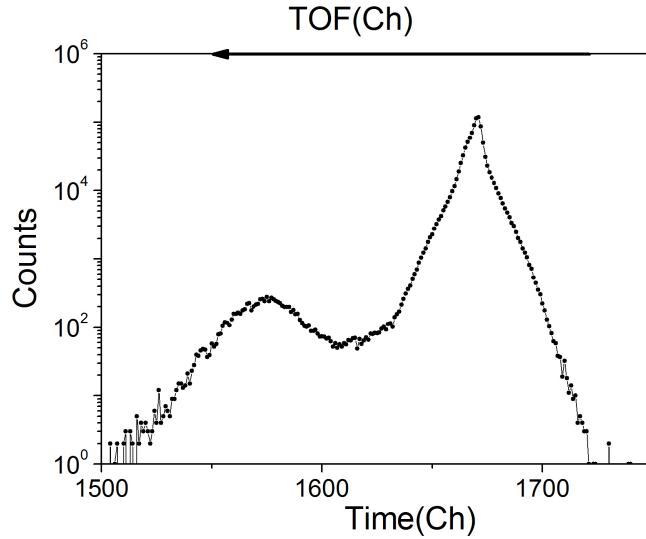
Figure 3.8: Time-spectrum acquired with a PPAC in order to identify the evaporation events.

hit the veto. This value is larger for the faster events. Consequently in the spectrum there is an inversion of time relative to the two channels. However, regardless of the presence of the second PPAC like veto, in the spectrum the bigger contribution is produced by the elastic scattering. This is due to the efficiency of the veto system which is affected by the geometrical shape of the PPAC detector and the performance of electronic system.

Putting the coincidence condition between the registered events in the PPAC and the particles identified in Wall and Ball detectors, there is a consistent reduction of the ratio between the elastic and ER peak because there is no particle emission in the elastic scattering process. The same time spectrum of Fig.3.8 changes into the one shown in the Fig.3.9 after imposing the coincidence with particles.

The assumption that the particles in coincidence with ER's peak come from fusion-evaporation process is confirmed by the time-spectrum shape. There is no correction for the random coincidences, they are negligible with respect to the true coincidences. The LCPs in coincidence with ER are selected by marking with contours (windows) the corresponding regions in the $\Delta E - E$ and $TOF - E$ matrices (cfr. Figs. 3.2 and 3.3) and by gating on the ER peak of Fig.3.9. By merging the events identified with these selections and using the energy-channel calibrations the program builds the evaporative energy spectra for protons and $\alpha-$particles . These spectra, integrated in energy, supply the angular correlation LCP-ER corresponding to each different
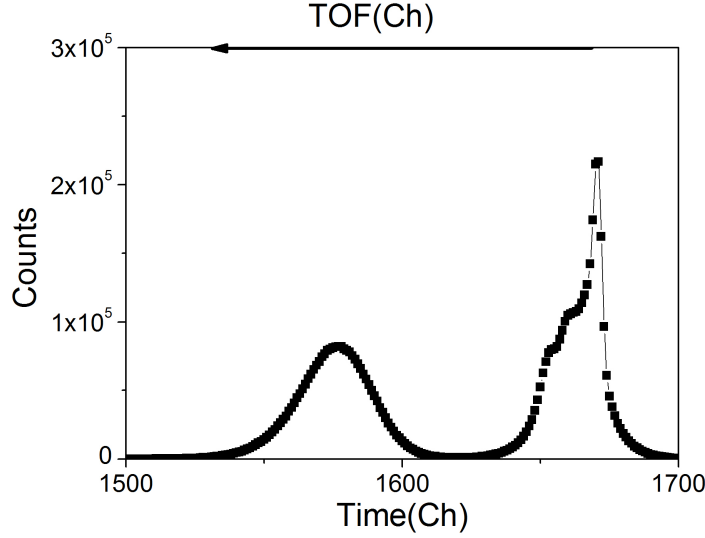
Figure 3.9: Time-spectrum acquired with a PPAC in coincidence with light particles measured by the telescopes of 8πLP.

PPAC.

3.3.1 Angular correlations LCP-ER

LCP spectra in coincidence with ER are normalized with the total ER single events (without coincidence condition). This allows to obtain in the following way the differential multiplicity angular distribution: $dM_i(\theta_j)/d\Omega_j$ (sr^{-1}), where the index i indicates the particle kind. In particular, $Y(\theta_j, \theta_{ER})$ is the number of the particles detected at angle θ_j in coincidence with the ER's detected in the PPAC at angle θ_{ER}; the double differential cross section is given by:

$$\frac{d^2\sigma}{d\Omega_j d\Omega_{ER}} = \frac{Y(\theta_j, \theta_{ER})}{IN_T \Delta\Omega_j \Delta\Omega_{ER}},\qquad(3.3)$$

where I represents the number of beam particles impinging on the target, N_T is the superficial density of nuclei in the target. $\Delta\Omega_j$ and $\Delta\Omega_{ER}$ represent the solid angles of the particle and ER detectors, respectively. Indicating with $Y(\theta_{ER})$ the number of ER in single events (without coincidence conditions), the differential ER cross section is:

$$\frac{d\sigma}{d\Omega_{ER}} = \frac{Y(\theta_{ER})}{IN \Delta\Omega_{ER}}.\qquad(3.4)$$

69
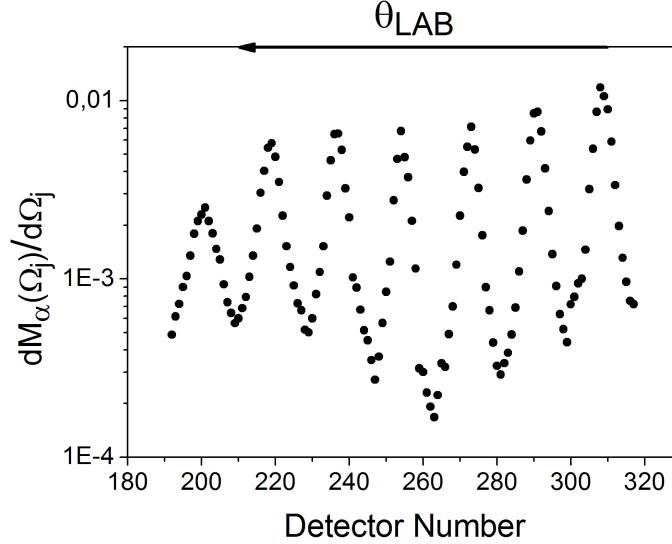
Figure 3.10: Experimental angular correlation of $\alpha-$particles .

From the ratio of Eqs. 3.3 and 3.4 we deduce the differential multiplicity:

$$\frac{dM_i(\theta_j)}{d\Omega_j} = \frac{\frac{d^2\sigma}{d\Omega_j d\Omega_{ER}}}{\frac{d\sigma}{d\Omega_{ER}}} = \frac{Y(\theta_j, \theta_{ER})}{Y(\theta_{ER})\Delta\Omega_j}. \tag{3.5}$$

It is important to consider that I and N_T are the same in coincidence and single measurements. In fact the events are acquired in the same run for both modes. For the ER production in single mode the dividers are taken into account.

In the Figs. 3.10 and 3.11 the angular correlations particle-ER, in terms of differential multiplicities, for protons and $\alpha-$particles , corresponding to a PPAC are shown. The oscillating behaviour, explainable on the basis of kinematics and angular momentum effects, is discussed in the next paragraph, as well as the procedure to estimate the total multiplicity of LCPs in the FE channel.

3.3.2 LCP multiplicity in the FE channel

The particle multiplicities in the FE channel are extracted with the help of the statistical model because a direct measurement requires the use of an
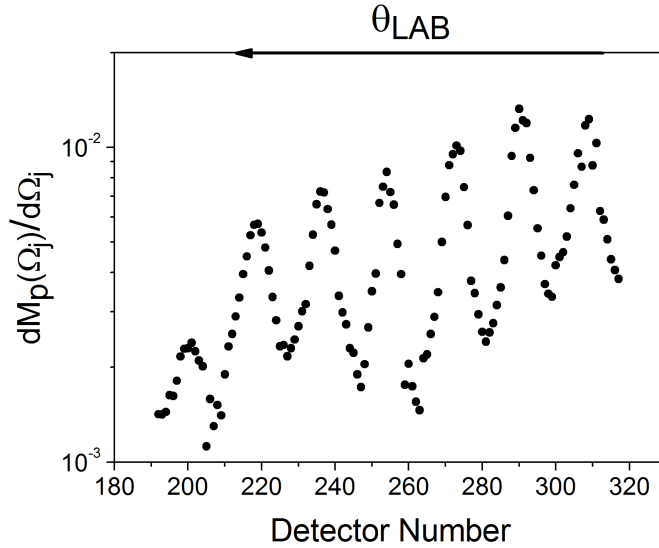
Figure 3.11: Experimental angular correlation of protons.

apparatus able to measure all the LCPs and ERs emitted, that means, an angular coverage of 4π for LCP as well as for ER detectors. However the ordinary apparatuses have a limited angular coverage for both quantities. To extract the differential multiplicity distribution of LCPs in the ER channel Eq. 3.5 was used.

In the Figs. 3.10 and 3.11 the differential multiplicities are shown. The oscillating behaviour depends on the features of the experimental apparatus and is explainable on the basis of simple considerations about the particle emission process. When a particle is emitted the residual nucleus assumes a recoil velocity determined by the momentum and energy conservation laws. The angular momentum of the compound nucleus makes the plane perpendicular to its direction preferential for particle emission. This is called spin-off effect. These kinematic constraints coupled with a specific geometrical configuration of the 8πLP detectors determins the angular correlation (AC) shape between the particles and evaporation residues.

The reaction plane is defined as the plane containing the beam direction and the center of the ER detector. The spin is consequently aligned in the direction perpendicular to the reaction plane. Particles are preferentially emitted in the reaction plane because of the spin-off effect. The local minimum and maximum in Figs. 3.10 and 3.11 correspond to the particle detector in this plane. The minimum is reached when the particle detector is in the semi-plane as the ER detector; instead the maximum is when the ER detector and the LCP detector are in the opposite semi-plane. All the other detectors,

71

at the same polar angle, but with different azimuthal angle with respect to the beam axis, assume the intermediate values. The difference between the amplitudes of the maxima depends on the variation of the polar angle, for fixed values of the azimuthal angle. In fact the decrease of the polar angle with respect to the beam will increase the differential multiplicity due to the focusing produced by the center mass velocity.

To integrate the differential multiplicity distributions we use a code which implements the statistical model. During the extraction of the multiplicity all the variations induced by the kinematics of the process have been properly taken into account thanks to the use of a simulation code that calculates step by step the quantities associated to each emitted particle. To determine the total multiplicities (the average number of protons or $\alpha-$particle per ER) it is necessary to integrate the experimental differential multiplicity distribution on the whole angular range. This is accomplished by the statistical model code once the input parameters are adjusted to reproduce the experimental angular distribution shown in Figs. 3.10 and 3.11.

The first step consists in the search for a prescription of SM able to reproduce the AC behaviour once the experimental constraints are include in the code (detectors geometry, energy thresholds....). Here we assume that if the measured behaviour is reproduced in 80% of the total angular range, there is no reason that justifies differences in the remaining solid angles. In particular this assumption is confirmed by the fact that the dependence of the behaviour has no singularity points, because it depends on analitical laws and center of mass motion. The calculation has been performed with the well known code Lilita_N97 [Gom81]. In the final step, the calculated AC is normalized to the experimental one. The normalization factor times the calculated total multiplicities provides the experimental multiplicities. The values obtained are summarized in Tab.3.1.

System	M_p	M_α
$^{32}S +^{100}Mo$	0.90(0.14)	0.56(0.09)
$^{32}S +^{126}Te$	0.38(0.03)	0.23(0.08)

Table 3.1: Proton and $\alpha-$particle multiplicities in the FE channel for both measured systems ^{132}Ce and ^{158}Er.
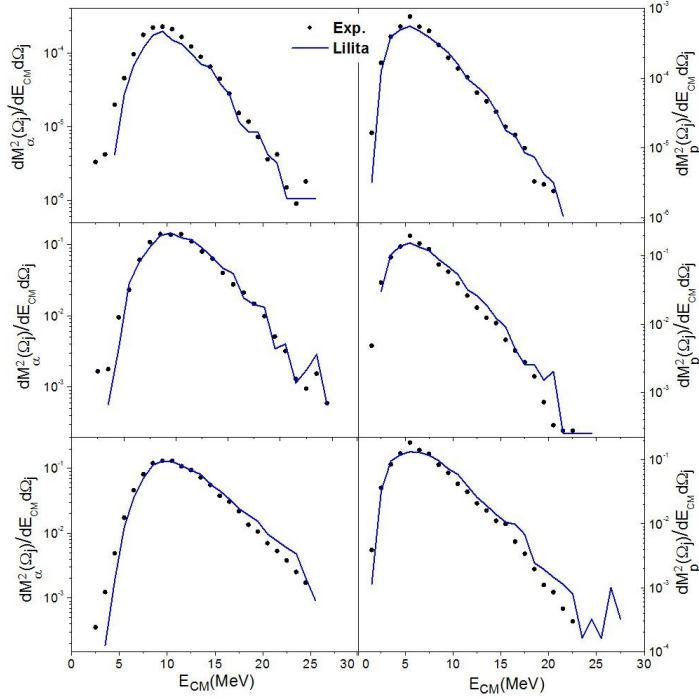
Figure 3.12: Experimental energy spectra in the 8πLP-Ball detector at $\theta = 142^{\mathrm{o}}$(dots). On the left side the $\alpha-$particle spectra and on the right the proton ones are shown. Going from up to down the PPAC in coincidence changes, they are up, down and left respctively.

3.3.3 Proton and α-particle energy spectra in the FE channel

In the Fig. 3.12 the energy spectra, in the laboratory system, of LCPs in coincidence with the ERs, for the Ball detectors at $\theta = 137^{\mathrm{o}}$ and $\phi = 80^{\mathrm{o}}$, are shown. In particular, on the left side the $\alpha-$particle spectra are reported and on the right side the proton ones. From up to the down, the coincidence spectra with PPAC UP, DOWN and LEFT are plotted, respectively. In the same figure the results of SM calculation are reported as a continuous line.

The maxima of particle spectra in the laboratory system are at different energies and amplitudes, due to the different kinematics of the reaction and also to the different angular correlation with the ERs.

All the experimental particle spectra before the comparison with the calculations have been transformed in the center mass system by an automatic procedure which takes into account the kinematic conditions of the process. These spectra show a Maxwellian shape due to the evaporative behavior of the emission. As expected, on the base of the statistical model, all the spec-
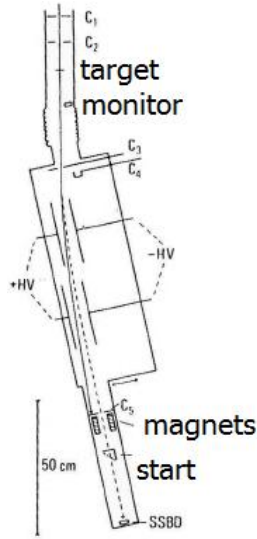
Figure 3.13: Electrostatic spectrometer for cross section measurement (from [Beg85]).

tra show a similar shape in the center of mass frame. This confirms a good energy calibration and a correct working of the detection system.

3.3.4 Evaporation Residues and Fission Cross Section measurement

The knowledge of the FE cross section is important because, together with the FF cross section, allows to put a severe constraint on the model parameters. The sum of $\sigma_{FF} + \sigma_{FE}$ is the fusion cross section.

The measurement of FE cross section was carried out using an electrostatic beam separator [Beg85] for heavy recoiling products (Fig.3.13), that allows to measure the differential cross sections in the angular range $0^o \div 12^o$.

An electrostatic deflector is placed between the target and ER telescope, to separate the beam from the ERs. The different electric stiffness of ERs and beam ions is exploited applying a strong electric field (HV) perpendicular to the ion's direction. The beam and the ERs are then spatially separated; the first are stopped on an exit side of the final collimator (C5), the ERs are instead sent on to a telescope.

The telescope is constituted by a first detector that is a micro-channel plate and represents the start for the TOF measurement; the second is a silicon SSBD with an area of $200 \div 300$ mm^2 and measures the total energy of the ER. It is placed at 30 cm from the first one. The ERs are identified

74
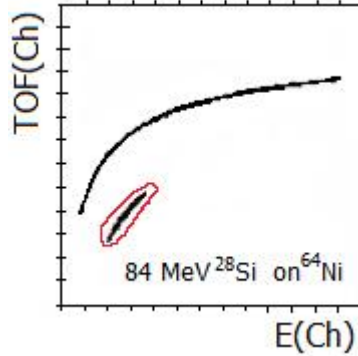
Figure 3.14: Identification of evaporation events from the background of elastic scattering (from [Beg85]).

and separated from the background of the beam-like ions produced in the elastic scattering. In the Fig. 3.14 the E-TOF matrix is shown. The ER angular distribution is obtained by rotating the whole experimental set-up in the horizontal plane. The higher energy events are produced by the elastic scattering and are placed on a hyperbola branch.

The main property of this apparatus consists in the possibility to suppress the presence of the beam-like ions in the telescope till a factor 10^8. The optimal condition for the measurement is obtained setting the high voltage, applied to the electrodes of separator, in order to maximize the ERs production. The absolute value of cross sections is obtained by four monitor counters that are placed in the scattering chamber at the grazing angle in symmetric positions with respect to the beam direction.

The differential cross section of the ERs at the angle θ is obtained from the following expression:

$$\frac{d\sigma}{d\Omega}(E,\theta) = \frac{N_{ER}(\theta)}{N_{mon}(\theta_0)} \frac{1}{\eta_d} \frac{\Delta\Omega_{mon}}{T\Delta\Omega_{ER}} \left(\frac{d\sigma_{Ruth}}{d\Omega}(mon,\theta_0) \right)_{LAB}, \qquad (3.6)$$

$N_{ER}(\theta)$ is the number of ER events; $N_{mon}(\theta_0)$ is the number of beam ions elastically scattered and computed by the monitor detectors; η_d the detector efficiency, that includes the dead time of the electronics, the transparency of the grid and the efficiency of the micro-channel plate; $d\sigma_{Ruth}/d\Omega(mon,\theta_0)$ is the calculated Rutherford cross section corresponding to the monitor counters; $\Delta\Omega_{mon}$ and $\Delta\Omega_{ER}$ are the geometric solid angles of the monitor and the telescope counter, respectively. T is the transmission of the electrostatic deflector, which indicates the effective fraction of $\Delta\Omega_{ER}$. In fact the ERs are scattered in the plane of the electric field due to their dispersion in energy and charge state. T changes very slowly with the beam energy and

75

ranges in the interval $0.50 \leq T \leq 0.75$. The silicon detector efficiency is $\eta_d = 1$, $\Delta\Omega_{mon} = 4.13 \cdot 10^{-5}$sr is the solid angle of each monitor detector and $\Delta\Omega_{ER} \cong 2.1 \cdot 10^{-5}$sr is the solid angle of the telescope. In the reaction $^{32}S +^{100} Mo$ the value θ_0 of the grazing angle is 16°.

The same apparatus has been used for the measurement of the fission cross section. The value of the differential cross section is given by a formula similar to the Eq.3.6 where the ER has been substituted with "fiss":

$$\frac{d\sigma}{d\Omega} = \frac{N_{fiss}}{N_{mon}(\theta_0)} \frac{1}{\eta_d} \frac{\Delta\Omega_{mon}}{\Delta\Omega_{fiss}} \left(\frac{d\sigma_{Ruth}}{d\Omega}(mon, \theta_0) \right)_{LAB} \qquad (3.7)$$

where the new parameter is $\Delta\Omega_{fiss}$, the solid angle of fission fragments detector that is $\approx 3.5 \cdot 10^{-5}$sr.

In the Tab.3.2 the values of extracted cross sections are reported.

System	σ_{FE} (mb)	σ_{FE}(mb)
$^{32}S +^{100} Mo$	828(50)	130(13)

Table 3.2: FE and FF cross sections measured with the electrostatic deflector for ^{132}Ce composite nuclei.

3.4   Analysis of the Fusion-Fission channel

One of the goal of this work is to compare the LCPs multiplicities for the systems under study in the FE and FF channel with the prediction of nuclear models. For the reaction $^{32}S +^{100} Mo$ the rings F and G have been used to detect FF because their angular position optimize the counting rate of coincidences between the fission fragments. Only the ring F has been used in the case of $^{32}S +^{126} Te$. Triple coincidences fragment-fragment-particle and double coincidence fragment-fragment have been measured.

Triple coincidence LCP energy spectra have been built by using all the possible conditions of two fragments in the F/G rings and a particle in whole Ball. The two fission detectors identify the reaction plane, as shown in Fig.3.15. The position of the third detector, where the particles are observed, is defined by two angles: in plane α and out-of-plane β.

The rotational axial symmetry of 8πLP around the beam axis produces eighteen different triples of detectors which identify the same angular correlation, specified by the angles α and β; so their spectra can be summed, corresponding to the same angular correlation fragment-fragment-particle. This allows to increase one order of magnitude the statistics of the triple coincidence events.
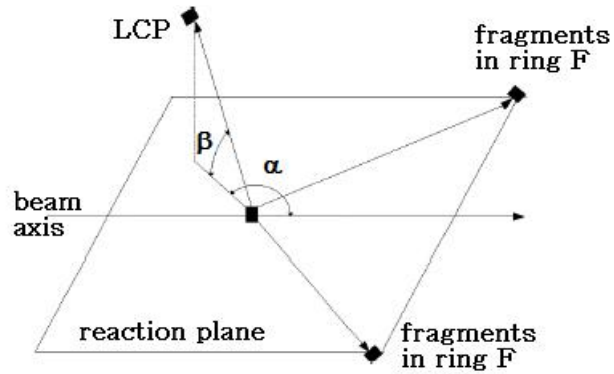
Figure 3.15: Geometry of a triple coincidences measured with 8πLP apparatus for the fission channel. α is the angle in plane and β the angle out-of-plane; they together identify the position of LCP detector with respect to the reaction plane.
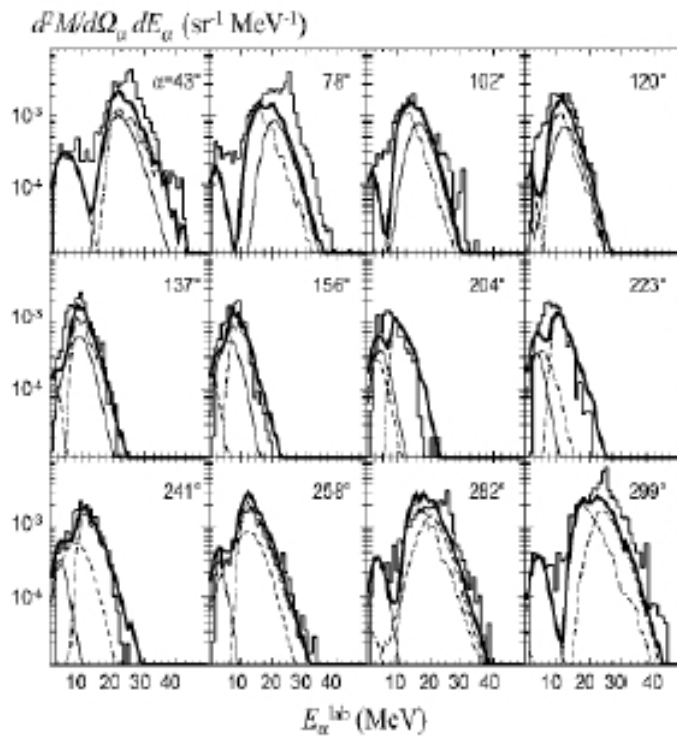
Figure 3.16: $\alpha-$particles spectra measured in fusion-fission channel disentangled on the basis of the different emitting components. All spectra are measured in detectors placed in the same plane of the fission fragments ($\beta = 0$) for different values of α angle.

In the Fig.3.16, as example, the $\alpha-$particle spectra (histogram), measured in coincidence with the fission fragments are shown, for different values of the in-plane angle α and with $\beta = 0$ (in-plane spectra). The spectra are represented in terms of double differential multiplicity. The coincidence spectra are normalized at the corresponding double fragment-fragment coincidence events. Superimposed to the experimental data are the results of a simulation with the program GANES [Aji86] for the following processes of LCP emission.

For each fission trigger, the particle can arise from several sources. In order to extract the pre- and post-scission integrated multiplicities, LCP spectra have been analysed considering three evaporative sources: the composite nucleus prior to scission (CE) and the two fully accelerated fission fragments (F1 and F2). We have used a well-established procedure which employs the Monte Carlo Statistical code GANES. $\alpha-$particles evaporative spectra are computed separately for each source of emission in the trigger configuration defined in the experiment, taking into account the detection geometry. Afterwords, the calculated spectra are normalized to the experimental ones, and the integrated multiplicities are calculated for each emitting source. Since the components overlap in the experimental data, the normalization procedure starts by establishing upper limits for the contribution of each component from the region of the spectra where one component is prominent with respect to the other ones. The curves superimposed on the histograms represent calculated multiplicity spectra for CE (dot-dashed curves), F1 (light solid line) and F2 (dashed line) components, along with their sum (dark solid line). The code GANES simulates the single-step particle emission from deformed nuclei and the evaporation barriers are determined by the extent of the deformation. The single-step approximation can be considered reasonable in the case of LCP pre-scission emission characterized by low multiplicity and high first-chance emission probability. In our calculation, deformation is introduced only for the CE emission, whereas fragment evaporation is assumed from spherical nuclei. The compound-nucleus angular momentum has been extracted from the fusion cross section.

The deformation of the emitter affects both the mean energy of the evaporated charged particle, because of the change in the evaporation barriers, and the out-of-plane angular distribution, because of the increase in the moment of inertia. This emitter deformation results into mean energies of the $\alpha-$particles which are ≈ 2 MeV lower than those expected in the case of a spherical emitter. It is important to stress that to reproduce both the energy spectra and the out-of-plane angular distributions imposes very strong constraints on the model parameters. In this respect, the $\alpha-$particles angular distribution is very sensitive to the nuclear deformation.

Assuming the evaporation from the three emitting sources, the bulk of the experimental spectra is very well reproduced, also considering the wide angular coverage of the detecting array. From the fit to experimental spectra, protons and $\alpha-$particles multiplicities for pre and post-scission emissions have been deduced.

3.4.1 Fission Fragments Mass - TKE distribution

The measurement of mass and total kinetic energy distribution of fission fragments has been carried out using a Time-of-Flight spectrometer called CORSET [Koz08]. A double-arm TOF spectrometer, with a flight path of 30 cm, forms the basis for the experimental setup. This spectrometer includes a compact start micro-channel plate (MCP) detector and position-sensitive MCP stop detector. The two arms replace two telescopes of the ring F on the opposite sides with respect to the beam. This system allows to detect binary products of nuclear reactions. The quantities measured are the time spent by the ion to span the flight path (distance between start and stop detectors) and the (x,y) position of the impact on the stop detector. These three quantities, measured for both fragments, allow to determine the primary mass and energy of the fragments if the two-body kinematics equations are employed.

The time resolution of MCPs is of the order 100 ps, therefore it is possible the separation of different fission products also with a short flight path. This feature allows to achieve the mass resolution of ≈ 2 mass units. The aim of the analysis of the fission fragment data was to determine primary fragment masses m_1 and m_2 and velocity vectors $\tilde{v}_1$ and $\tilde{v}_2$. It was done with a successive approximation method. In the zero approximation, fragment velocity vector $\tilde{v}_f^0$ is determined from the TOF and from the registered coordinates. The main source of error at this stage comes from unaccounted energy loss in the START detector converter foil and in the target ($\Delta E \approx 5$ MeV for symmetrical mass split in both cases). The first approximation for fragment masses $m_{1,2}^0$ was calculated using momentum conservation perpendicular to the beam axis $m_1 v_1^\perp = m_2 v_2^\perp$ and assuming that the two fragment masses add up to the mass of the compound system prior to fission ($m_1 + m_2 = M_{projectile} + M_{target} - \langle M^{pre} \rangle$), where $\langle M^{pre} \rangle$ is the mean total mass of particles evaporated from the compound nucleus before scission. Since, according to our model predictions, neutrons dominate in pre-scission emission and $\langle M^{pre} \rangle$ was assumed to be equal to neutron pre-scission multiplicity $\langle M_n^{pre} \rangle$. The value of $\langle M_n^{pre} \rangle$ was taken from systematics. The influence of uncertainty in $\langle M^{pre} \rangle$ determination turned out to be much smaller than
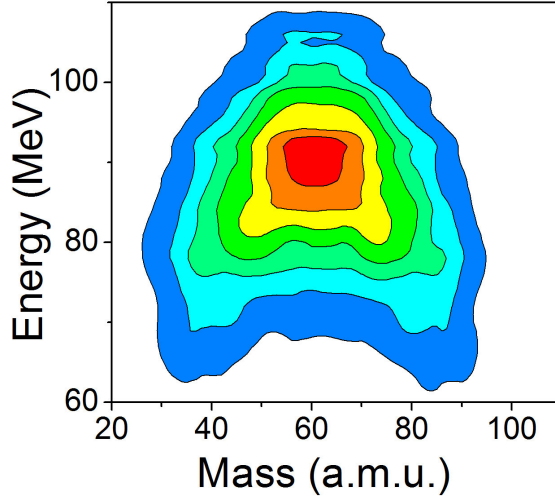
Figure 3.17: The experimental MED of fission fragments. See text for details.

System	M	σ_M	TKE	σ_{E_K}
	a.m.u.	a.m.u.	MeV	MeV
^{32}S $+^{100}$ Mo	66	15.4	90.9 (85.9)	11.4

Table 3.3: Experimental values of mass and energy distribution measured with CORSET spectrometer.

the overall errors. From $v^{\vec{0}}_{1,2}$ and $m^0_{1,2}$ fragment energies $E^0_{1,2}$ were determined using non relativistic formulas. Known fragment mass and energy allows us to calculate consequently the energy loses in the START detector and the target. From the corrected values of $E^1_{1,2} = E^0_{1,2} + \Delta E^{START} + \Delta E^{target}$ and old values of fragment masses $m^0_{1,2}$, new values of the fragment velocities "in the target" are calculated. The above procedure is repeated until it converges. Namely when the last values of the masses obtained is within 1 or 2 mass units from the ones calculated in the step before last. Usually, less than ten iterations are sufficient. Using the extracted values of $\tilde{v}^0_{1,2}$ and $m_{1,2}$ the TKE distribution of fission fragments are calculated. The obtained Mass-TKE distribution is shown in Fig. 3.17.

From the projections of the matrix we have extracted the values reported in Tab.3.3 that can be directly compared with the predictions of dynamical model as it will be seen in the next chapter.

3.5 Summary of the Experimental Data

The full set of experimental data are summarized in Tab.3.4. The number in parenthesis represent the experimental errors. These data are the subject of the investigation in the next chapter.

| System | FE channel | | | FF channel | | | M | σ_M | TKE | σ_{E_K} |
	M_p	M_α	σ_{FE} mb	M_p	M_α	σ_{FF} mb	a.m.u.	a.m.u.	MeV	MeV
$^{32}S+^{100}Mo$	0.90(0.14)	0.56(0.09)	828(50)	0.055(0.007)	0.038(0.005)	130(13)	66	15.4	90.9	11.4
$^{32}S+^{126}Te$	0.38(0.03)	0.23(0.08)	-	0.034(0.005)	0.020 (0.003)	-	-	-	-	-

Table 3.4: Proton and $\alpha-$particle multiplicities in the FE and pre-scission channels, FF and FE cross sections, and mass and TKE fission fragment distributions for both measured systems ^{132}Ce and ^{158}Er.

Chapter 4

Comparison with the predictions of the models

As mentioned in the first chapter, there are still many open questions on fission dynamics. They mainly refer to a precise determination of the fission time-scale as well as the strength and nature of nuclear viscosity and its dependence on the shape and the temperature.

Concerning the time-scale the estimates based on the SM are spread-out over a wide time interval. The main reasons for such a result rely on:

a) the use of the SM, which cannot take into account in a realistic way for the dynamics of the process;

b) the time estimates strongly depends on the parameters used in the model, concerning the level density and the transmission coefficients;

c) the pre-scission light particles and the $\gamma-$ray may probe only the initial part of the fission time distribution, the extent of this part being dependent on the probe.

Although these limitations, the phenomenological study of the characteristic fission time with the SM plays an important role as they provide a clear evidence of the role of nuclear viscosity in the fission process.

Fission dynamics process has been also studied in the framework of dynamical models. Depending on the physical ingredients and the degrees of freedom adopted, these models may provide a realistic description of the fission process. Although much studies based on these models have been carried out, the nature and the strength of nuclear dissipation remain an open question, although most of the indications are in favor of a strong one-body dissipation.

In this framework, the aim of the present work is to make a step forward in the understanding of these aspects still debated of fission dynamics, attacking the problem on two fronts:

a) From the experimental point of view we have chosen to study systems of intermediate fissility, using the high efficient 8πLP apparatus at LNL. This allows to put severe constraints to the models. In fact as already mentioned, these systems present comparable cross sections of FE and FF channel, as well as relatively high emission probability for pre-scission LCP. Therefore, a large set of observables in both channels can be obtained. Furthermore, compared to the heavier systems, those of intermediate fissility are expected to have scission configurations close to the saddle ones, in the space of deformation. This behaviour enhances the role of pre-saddle time, resulting in a simplified physical situation to be studied.

b) From the theoretical point of view, data have been compared to a dynamical model based on three dimensional Langevin equations. The model has been implemented with a realistic treatment of particle evaporation on the base of Lilita_N97 code, which has been linked to the dynamical model code. This version of the model can be considered one of the the most advanced one in the field, representing a powerful tool to investigate fission dynamics.

In order to have a comparison with the previous phenomenological studies, data have been also compared with the prediction of the statical model, as implemented in the evaporative codes PACE2 and Lilita. These latters have been extensively modified in order to include new physical options.

In this chapter we present the analysis of the systems of intermediate fissility ^{132}Ce and ^{158}Er produced at U=122 and 92 MeV by the reaction ^{32}S $+^{100}$ Mo and ^{32}S $+^{126}$ Te.

We start presenting the analysis of ^{132}Ce system in the framework of the statistical model. Then, the analysis with the dynamical model for both systems will be presented, together with a discussion of the results and the conclusions.

4.1   Results for 200 MeV ^{32}S $+^{100}$ Mo system

As illustrated in the third chapter, we have measured an extended set of observables in the fission and evaporation channels for the system 200 MeV ^{32}S $+^{100}$ Mo. Light charged particles in coincidence with fission fragments

and evaporation residues have been measured with 8πLP apparatus at LNL. These measurements allowed to obtain proton and $\alpha-$particle multiplicities in the pre-scission and in the evaporation residue channels, as well as particle energy spectra in both channels and their angular correlation with the evaporative residues. The fission fragment TOF spectrometer CORSET has been coupled to 8πLP in oder to measure Mass-TKE distributions of fission fragments.

FF and FE cross sections have been also measured with the electrostatic separator of the LNL.

These observables, except Mass-TKE distributions, have been compared with the SM predictions, taking into account for the response function of 8πLP apparatus in the simulation.

4.1.1 Analysis based on the Statistical Model

Our approach, using the SM, has been mainly focused on the analysis of the charged particle multiplicities and cross sections in FF and FE channels.

	FE channel			FF channel		
	M_p	M_α	σ_{FE} (mb)	M_p	M_α	σ_{FF} (mb)
Exp.	0.90(0.14)	0.56(0.09)	828(50)	0.055(0.007)	0.038(0.005)	130(13)
present calc.	1.44	1.64	813	0.058	0.034	143

Table 4.1: Proton and $\alpha-$particle multiplicities in the FE and pre-scission channels and FF and FE cross sections for 200 MeV ^{32}S $+^{100}$ Mo reaction. The calculation is performed using the parameters which best reproduce the FF channel data. See text for details.

The set of data is shown in Tab. 4.1 together with the results of the SM calculations performed with the code PACE2_N97 [Gav80]. If we limit our analysis to the FF channel only, namely, if we only try to reproduce the multiplicities in the FF channel as usually done [Pau94], the data can be reasonably well reproduced assuming a_n=A/9, a_f/a_n=1.04, a liquid drop model (LDM) yrast line and optical model (OM) transmission coefficients [Hui61, Per63, Wil64], without any delay. From this result one could conclude that no dynamical effects take place in this decay, in contrast with the systematics [Tho93], although a different combination of input parameters does not exclude the presence of a relatively small fission delay. On the other hand, with the same parameters, the model strongly overestimates the FE particle multiplicities even though it reproduces the FE cross section. This is an evident contradiction: if the model is not able to reproduce the light charged particle multiplicities in the FE channel, once the FE cross section

is well accounted for, the same model can not be supposed as a reliable tool to estimate the fission time scale through the pre-scission light particle multiplicities.

In order to explore the possibility to reproduce the data of both channels with a unique set of input parameters we performed an extensive analysis with different prescriptions of the level density parameter and transmission coefficients, appropriate for the mass and excitation energy of the system under study. Calculations have been carried out adopting three different and well known prescriptions for the yrast line: 1) Gilbert Cameron [Gil65], 2) LDM and 3) sharp rigid sphere (RS) with radius parameter r_0=1.2 fm. Different prescriptions have also been used for the level density parameter a_n: 1) a constant value ranging from A/6 to A/12; 2) inclusion of shell effects [Cha95] with a damping term [Ign75] as a function of the excitation energy and 3) a temperature dependent prescription [Les95]. Transmission coefficients derived from: 1) optical model and 2) fusion systematics (FS) [Vaz84] have been used. To modulate particle-fission competition, different values of fission delay and a_f/a_n have been adopted as well. Calculations have been constrained by the sum of the measured FE and FF cross sections σ_{fus}= 958 $\pm$ 50 mb.

	a	Yrast Line	Trans. Coef.
a	A/6	RS	OM
b	A/12	LDM	OM
c	A/6	RS	FS
d	A/6	LDM	OM

Table 4.2: Prescriptions adopted in the calculations with the statistical model for 200 MeV ^{32}S $+^{100}$Mo reaction.

In Fig. 4.1 we show the multiplicities for protons and alpha particles in the FE and FF channels, as well as the measured channel cross sections, compared to the calculated values, as a function of the ratio a_f/a_n. In the figure the results corresponding to four prescriptions are reported; they are labeled a,b,c,d in Tab.4.2 where the adopted are shown. These prescriptions have been chosen among the many combinations for which calculations have been performed as they allow to explore the full range of variability of the calculated values of the observables under examination. Concerning the shell and temperature effects on a_n parameter as well as Gilbert Cameron prescription for the level density, they produce only minor changes in the results and therefore, are not presented. No fission delay has been included in the calculations.

From Fig. 4.1 we infer that the model is not able to reproduce the observables altogether, the larger deviations being in the FE channel. Here we
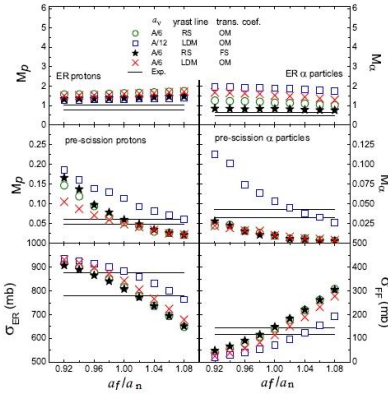
Figure 4.1: Measured evaporative (FE) and pre-scission (PRE) charged particle multiplicities together with the FF and FE cross sections (full lines indicating lower and upper limits of the uncertainty), compared to the predictions of the statistical model changing: the level density parameter (a_n), the yrast line, and the transmission coefficients. For details see text.

can briefly highlight some of the deviations and expected trends in the FE channel. As a general behaviour, for a fixed yrast line, higher values of a_n reduce $\alpha-$particle multiplicities while those for protons are enhanced (square and cross). Compared to OM transmission coefficients, those derived from FS provide lower values for both proton and alpha particle multiplicities (circle and star). The dependence of the calculated multiplicities on a_f/a_n appears to be relatively weak. Finally, we observe, as expected, a strong sensitivity of the $\alpha-$particle multiplicity on the yrast line: assuming the RS yrast line (star), we obtain a strong reduction of this quantity, with respect to that obtained with LDM yrast line (circle).

The evaporative spectra in the FE channel do not allow to discriminate the best prescription. In particular, if we change the main parameters of SM in the commonly used range, the differences do not allow to reject any prescription as shown in Fig.4.2.

With respect to the energy spectra ER-LCP angular correlations appear to be a better probe as they are very sensitive on the SM parameter, as shown in the Fig.4.3. In particular, the differences between different prescriptions are more evident in the $\alpha-$particle -ER correlation with respect to the proton-ER one. All calculations are carried out for the value $a_f/a_n=1$. As a general behaviour, for a fixed yrast-line, the increasing of a_n produces a very strong increasing in the oscillating amplitude (red-dashed and blue dotted lines). Going from an yrast-line calculated using the LDM to an yrast
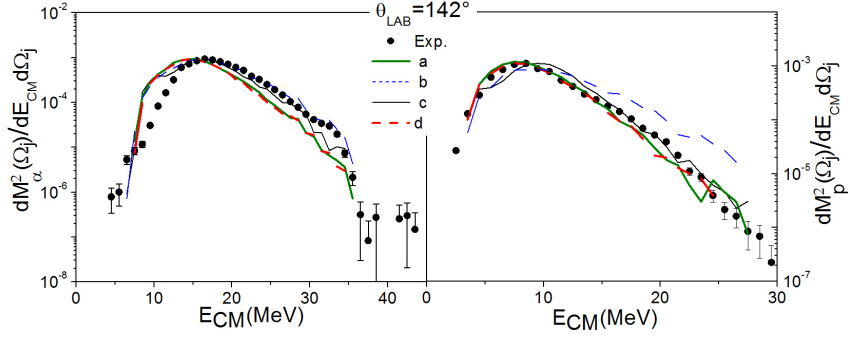
Figure 4.2: Measured α−particles (left) and protons (right) energy spectra in the center of mass system (dots), for the FE channel, compared with the prediction of the statistical model (lines), according different prescriptions, described in Tab.4.2.
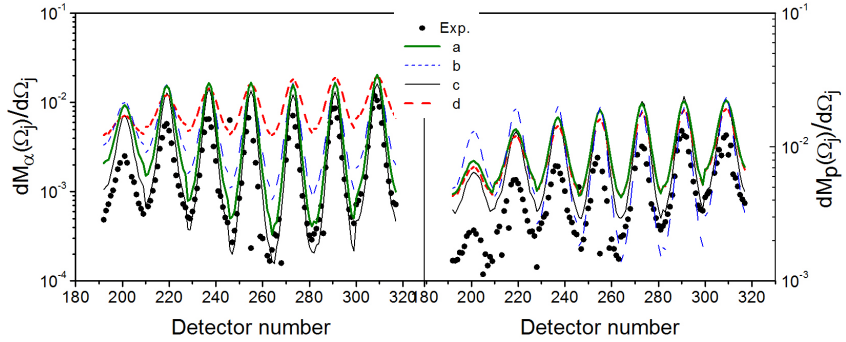
Figure 4.3: Same of Fig.4.2 for LCP-ER angular correlations.

line assuming the nucleus as a Rigid Sphere with $r_0 = 1.2$ fm, that means a decrease of the moment of inertia, we observe a reduction of oscillating amplitude for $\alpha-$particle angular correlation and an increase for proton one. This behaviour, in the case of $\alpha-$particles indicates $a = A/6$ more close to the experimental results. The sensitivity to the TC is not very strong and the amplitude is larger in the case of FS (green-solid and black solid lines).

The main result of this analysis is that the model strongly overestimates proton and $\alpha-$particle multiplicities in the FE channel for this system, irrespective of the prescriptions used for the level density and the transmission coefficients. The same conclusion is reached by the calculations performed with the well known codes Lilita_N97 and Gemini [Cha00]. Furthermore, the inclusion of a time delay to suppress the fission does not change the overall behaviour of the calculated data with respect to the experimental data. At the same time, the influence of nuclear deformation in the evaporative channel would further enhance the predicted particle multiplicities, resulting in a larger overestimation. On the other hand, the comparison of the measured proton and $\alpha-$particle energy spectra with the statistical model predictions, shows no evidence of nuclear deformation, in fact it would produce a shift towards low energy and would be particularly evident in the low energy part of the spectra due to the lowering of LCP emission barriers.

The causes for such unexpected behaviour of the SM can be searched along two lines: either the competition between the different decay channels is not properly accounted for or we are missing some decay channel or both. Indications toward the first hypothesis would come from the neutron multiplicity in the FE channel that, unfortunately, are rarely measured. A rough indication of how much the SM branching ratios should be changed in favor of the neutron emission might be taken from the experimental multiplicities. However, since the branching ratios are strongly dependent on the decay step, empirical constant factors to reduce the strengths do not represent a physical reasonable approach to this problem, and would open the question on how to use these new parameters in the FF channel. The measurement of the neutron multiplicities in the FE channel is at this point a mandatory task [Var00]. There is also the possibility of other decay channels not presently considered in the SM code PACE2_N97, like Intermediate Mass Fragments (IMF). Given the low probability of such emission due to low excitation energy, we don't expect the IMF channel to be important for the reactions taken under consideration. In any case we did not observe any IMF in our data from the system ^{32}S $+^{100}$ Mo at $E_{lab} = 200$ MeV in coincidence with ERs.

Concerning the fission channel, pre-scission proton and alpha particle multiplicity and fission cross section can be reproduced indicating no delay

in the fission process, although this result is made questionable by the findings in the FE channel. We have observed this behaviour also in other systems from literature [Var10] in the region $A \approx 150$ and U $\approx$ 100-200 MeV. This observation leaves an additional open question on the proper usage of the SM to predict fission delays.

4.1.2 Analysis based on the dynamical model

As mentioned in the previous paragraph, the analysis of the data for ^{132}Ce composite nuclei with the SM has shown the limitations of this approach to study fission dynamics. It must pointed out that this result could be obtained having measured an extended set of observables, in both FE and FF channels, wich strongly constrain the model. The same observables plus the Mass-TKE of fission fragments have been compared to the predictions of a dynamical model based on three dimensional Langevin equations.

The measured particle multiplicities in the FE and pre-scission channel together with the FF and FE cross sections for the reaction 200 MeV ^{32}S $+^{100}$ Mo are presented in the Tab. 4.3. The results of dynamical calculations for different values of one-body and two-body viscosity and level density parameters, are also reported.

In the calculations the level density parameter has been varied from a=A/6 to A/8. Considering the calculations of one-body viscosity one can see from the Tab.4.3, that the change of a from A/6 to A/8 at a fixed reduction parameter k_s results in an increase of pre-scission particles multiplicities and a decrease of σ_{FF}. The particle multiplicities in the FE channel changes also: the n_{FE} values decreases, p_{FE} does not change, α_{FE} increases. The decrease of dissipation from k_s=1.0 to 0.1 at fixed level density parameter a=A/6 results in a substantial increase of σ_{FF} from 143 mb to 230 mb, while the pre-scission n, p, and α multiplicities decrease by a factor 2 approximately.

In the case of two-body viscosity we report in Tab. 4.3 the results for the viscosity coefficient ranging from 0.02 to 0.5$\times10^{-21}$ MeV s fm^{-3}. This interval includes also unusual large values, i.e. much larger than the values found in the early work of Davies $\nu_0 \approx 0.02 \times10^{-21}$ MeV s fm^{-3}. The behaviour is qualitatively the same as in the case of one-body. The increase of viscosity coefficient results in slight change of multiplicities in the FE channel and a strong increase of pre-scission particle multiplicities. At the same time the σ_{FF} values decreases from 215 (187) mb to σ_{FF}= 77 (55) mb for a=A/6 (a=A/8). The change of viscosity coefficient at a fixed a influence the multiplicities in FF channel and σ_{FF} (σ_{FE}) cross sections only, whereas particles multiplicities in FE changes substantially less. Finally the change of level density parameter a results in a substantial change of pre-scission LCP

Viscosity		FE channel				FF channel			
One-body	a MeV^{-1}	n_{FE}	p_{FE}	α_{FE}	σ_{FE} (mb)	n_{pre}	p_{pre}	α_{pre}	σ_{FF} (mb)
k_s=0.1	A/6	5.41	1.26	0.55	706	0.34	0.021	0.013	230
k_s=0.25	A/6	5.38	1.24	0.54	762	0.39	0.026	0.016	174
k_s=0.5	A/6	5.35	1.22	0.54	770	0.52	0.042	0.017	166
k_s=1.0	A/6	5.30	1.198	0.56	793	0.63	0.052	0.030	143
k_s=1.0	A/7	5.16	1.20	0.61	797	0.64	0.059	0.041	139
k_s=1.0	A/8	4.98	1.20	0.70	802	0.80	0.075	0.061	134
Two-body (10^{-21} MeV s fm^{-3})									
ν_0=0.02	A/6	5.4	1.26	0.52	721	0.30	0.019	0.009	215
ν_0=0.02	A/8	5.1	1.24	0.66	749	0.29	0.037	0.022	187
ν_0=0.10	A/6	5.31	1.196	0.56	784	0.50	0.035	0.022	152
ν_0=0.10	A/8	5.00	1.18	0.69	789	0.52	0.057	0.041	147
ν_0=0.15	A/6	5.26	1.18	0.57	811	0.61	0.048	0.028	125
ν_0=0.15	A/8	4.93	1.17	0.71	822	0.59	0.063	0.043	114
ν_0=0.5	A/6	5.20	1.05	0.60	859	1.10	0.107	0.089	77
ν_0=0.5	A/8	4.76	1.06	0.76	881	1.25	0.181	0.174	55
Exp.			0.90	0.56	828		0.055	0.038	130
			(0.14)	(0.09)	(50)		(0.007)	(0.005)	(13)

Table 4.3: The experimental and calculated particle multiplicities in the FE and pre-scission channels together with the FF and FE cross sections.

multiplicities.

The calculations show that in order to fit experimental data in both FE and FF channels one needs to use level density parameter a=A/6 and strong dissipation $k_s = 1$ (full one-body) or the unrealistic value ν_0=0.15 $\times 10^{-21}$ MeV s fm^{-3} for two-body.

From the present results it is seen that the reproduction of the particle multiplicities together with the cross sections is only possible at high values of viscosity and level density parameter close to a=A/6.

In case of low viscosity at fixed level density parameter the value of σ_{FF} will be substantially overestimated. In case of change of level density parameter from A/6 to A/8 the values of α_{FE} will be overestimated.

In conclusion, for the best description of experimental data in the case of one-body dissipation one needs to use $k_s = 1$ and a=A/6. In this calculations only the values of p_{FE} will be overestimated approximately of 15%.

In the case of two-body dissipation one needs to use the very large value $\nu_0 \simeq 0.15 \times 10^{-21}$ MeV s fm^{-3} in order to get the best description of the experimental data.

Owing to the unususal value of two-body dissipation it appears to consider one-body as the dominant mechanism. This result is in agreement with previous findings from Ref. [Wad93] for ^{200}Pb compound nucleus. In particular, as already mentioned in chapter I, the authors found that the experimental pre-scission neutron multiplicities and the average TKE of fission fragments are well reproduced when one-body dissipation is assumed. Unusual strong
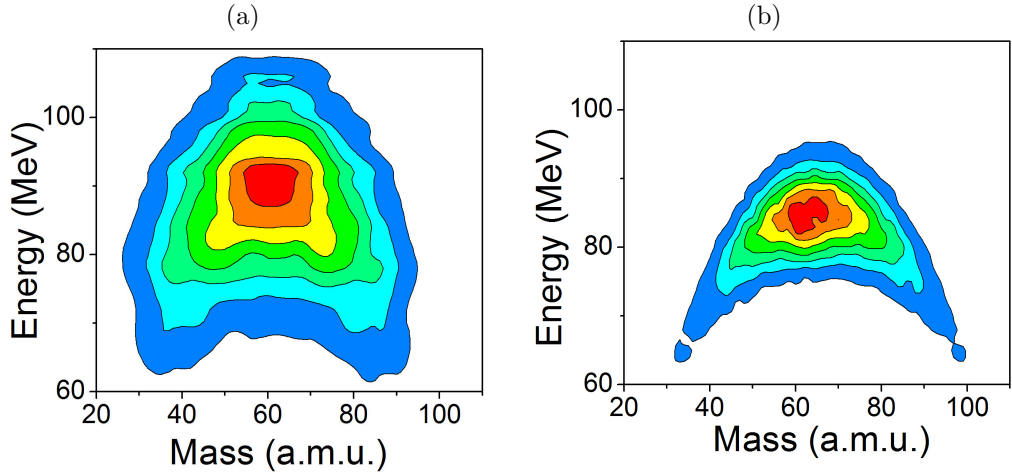
Figure 4.4: Experimental (a) and theoretical (b) MED of fission fragments. See text for details.

hydrodynamical two-body viscosity ν_0=0.125 $\times 10^{-21}$ MeV s fm^{-3} also reproduce the experimental neutron multiplicity, but it significantly underestimates the average kinetic energy of fission fragments.

4.1.3 Mass and TKE distribution of fission fragments

Mass and total kinetic energy of fission fragments for ^{132}Ce composite nuclei have been compared with the predictions of the dynamical model, adopting the input parameters that better reproduce the particle multiplicities and cross sections in FF and FE channels, namely one-body dissipation with $k_s = 1$ and a=A/6.

The fission fragment MED in the form of contour diagrams of the distribution $Y(E_K, M)$ obtained in the calculation in comparison with the experimental data is shown in Fig.4.4. One can see a reasonable agreement in the general behavior of the contours between the experimental and theoretical diagrams. However, the calculated distributions $Y(E_K, M)$ deviate from the experimental ones in the range around the mean values for symmetric fission. One can see, that in the calculations there are no events with $E_K > 95$ MeV. This means that in the dynamical calculations at the scission point there are not sufficient variability of the shapes of the nucleus.

The discrepancy can be clearly seen in Fig. 4.5, where the experimental and theoretical kinetic energy distributions of fission fragments are shown. The yield of calculated energy distribution is substantially lower than the experimental one in the range of high E_K values: $95 < E_K < 120$. The
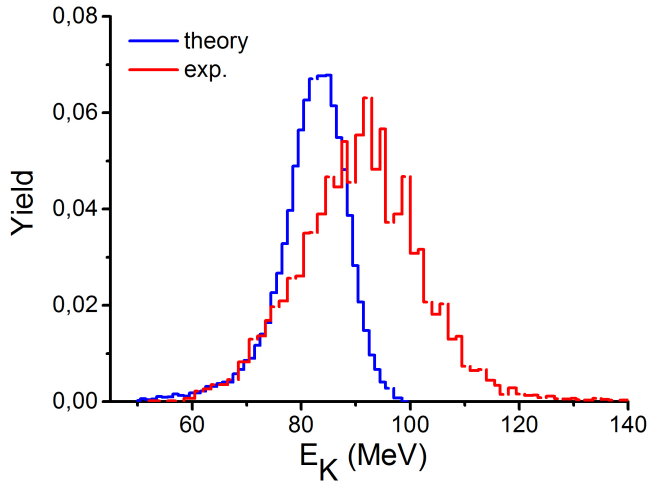
Figure 4.5: The experimental and theoretical (one-body) kinetic energy distribution of fission fragments.

experimental energy distribution is substantially wider than the calculated one. A similar result has been obtained in 3D Langevin calculations made in Refs. [Kar01]. In order to obtain values of σ_{E_K} closer to the experimental ones, one needs to use low values of viscosity $k_s \simeq 0.1 - 0.25$, which does not allow to reproduce the pre-scission particle multiplicities.

Anyway the variation of σ_{E_K} is very small as shown in Tab.4.4, where the calculated parameters of MED (the mean kinetic energy $\langle E_K \rangle$ and variances of mass σ_M and kinetic energy σ_{E_K} distributions) for other sets of input parameters are presented. (The average measured mass $\langle M \rangle = 66$ as well as the predictions of the model are not reported, as this observable is very well reproduced by the code, regardless the input parameter used.)

As can be seen from the table, the increase of σ_{E_K} from 7.3 to 8.1 MeV is obtained for a=A/6 going from k_s=1 to k_s=0.1.

The kinetic energies of fission fragments are determined at the moment of scission and depend on the scission criterion used in the calculations. The investigation of the influence of different scission criteria on the energy distribution is presented in Ref. [Bor08]. In this paper it was shown that commonly accepted scission criteria in nuclear physics could not provide a reasonable description of experimental energy distribution for a fissioning nuclei in a large range of Z^2/A, at least in the calculations based on the (c,h,α) parameterization. A possible way to improve the theoretical description of the experimental data on kinetic energy distribution could be the use of another deformation dependence of viscosity and/or the use of a new parameterization, which could provide more flexible shapes of the compound nucleus

Viscosity One-body	a	σ_M a. m. u.	σ_{E_K} MeV	$\langle E_K \rangle$ MeV
k_s=0.1	A/6	16.3	8.1	82.6
k_s=0.25	A/6	16.0	7.7	82.5
k_s=0.5	A/6	15.5	7.6	82.2
k_s=1.0	A/6	14.9	7.3	82.0
k_s=1.0	A/7	16.2	8.3	81.7
k_s=1.0	A/8	16.4	8.4	80.9
Two-body				
ν_0=0.02	A/6	15.2	7.6	81.9
ν_0=0.02	A/8	16.6	8.5	81.3
ν_0=0.10	A/6	15.1	7.5	79.6
ν_0=0.10	A/8	16.3	8.4	78.8
ν_0=0.15	A/6	14.6	6.7	79.6
ν_0=0.15	A/8	16.1	8.1	78.6
ν_0=0.5	A/6	14.2	6.6	78.6
ν_0=0.5	A/8	14.9	7.0	78.4
Exp.		15.4	11.4	90.9 (85.9)

Table 4.4: The experimental and calculated parameters of fission fragments MED. The experimental value of $\langle E_K \rangle$=85.9 MeV has been estimated from Viola's systematics [Vio85]

during the descend from saddle to scission.

The mass distributions of fission fragments are presented in Fig. 4.6. One can see that the theoretical calculations for one-body is able to reproduce reasonably well the experimental data. In order to improve the description of experimental mass distribution one can use lower values of k_s. However, the pre-scission particle multiplicities will not be reproduced in this case. The same behaviour has been obtained in the 3D dynamical calculations for other nuclei [Kar01, Nad02]. Assuming two-body dissipation with $\nu_0 = 0.15$ and a=A/7 the same quality of agreement is obtained.

As one can see from Tab. 4.4 the variances of mass and kinetic energy distributions σ_M and σ_{E_K} for the ^{132}Ce are not very sensitive to nuclear dissipation, like it is in the case of heavy nuclei [Kar01, Nad02]. The variances changes only about 25% when the viscosity coefficient k_s changes from 0.1 to 1. This feature of mass distribution is due to a short descent from saddle to scission point for light nuclei. The fissioning system ^{132}Ce pass the region between saddle and scission point in approximately 3×10^{-21} s. During this time the fluctuations of collective coordinates, which determine the width of mass and energy distribution have not the opportunity to become large.

To summarize, the experimental data on σ_M could be well reproduced by the calculations with one-body and two-body dissipation. The simultaneous fit of experimental data on σ_M and particles multiplicities in FF and FE channels could be obtained with k_s=1 (a=A/6) for the case of one-body dissipation and ν_0=0.15 ($a \simeq$A/7) for two-body dissipation although this latter is unusually large. The variance of kinetic energy distribution σ_{E_K} could
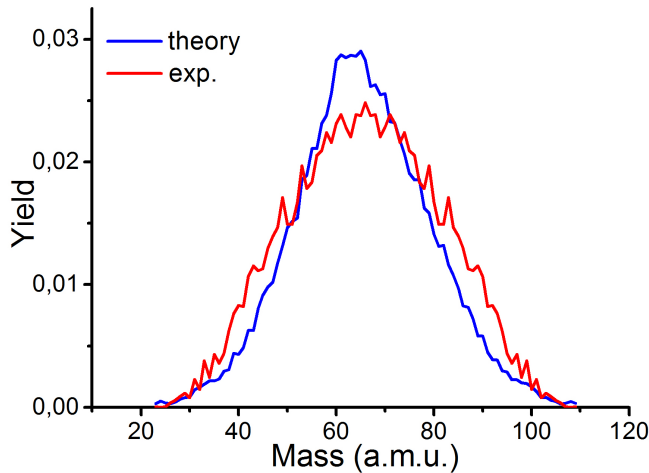
Figure 4.6: Experimental and theoretical (one-body) mass distributions of fission fragments.

not be reproduced in the present calculations. The mean kinetic energy $\langle E_K \rangle$ is better reproduced by the calculations with one-body dissipation than by the calculations with the two-body, this latter providing a value lower than the experimental one. This result is in agreement with the previous findings [Wad93].

4.1.4 Proton and $\alpha-$particle energy spectra

Experimental proton and $\alpha-$particle energy spectra for both fusion-evaporation and pre-scission channels, have been compared with the predictions of the dynamical model. Calculation have been carried out keeping the same input parameters: full (k_s=1) one-body dissipation, a=A/6 and transmission coefficients from fusion systematics.

Emission from spherical nuclei has been assumed in the calculation, for both channels the comparison for the fusion-evaporation channel is shown in Fig.4.7. The good agreement indicates that nearly spherical nuclei are involved in the fusion-evaporation channel.

A good agreement is also obtained for $\alpha-$particles in the pre-scission channel (cfr. Fig.4.8), indicating, also in this case that these particles are emitted from nearly spherical nuclei. This result implies that pre-scission $\alpha-$particle emission occurs in the early stage of fission, where small deformations are involved. This is in agreement with the findings of Ref. [Les91, Ike94], where a phenomenological analysis with the SM has been carried out.

As far as pre-scission protons are concerned, the model is not able to
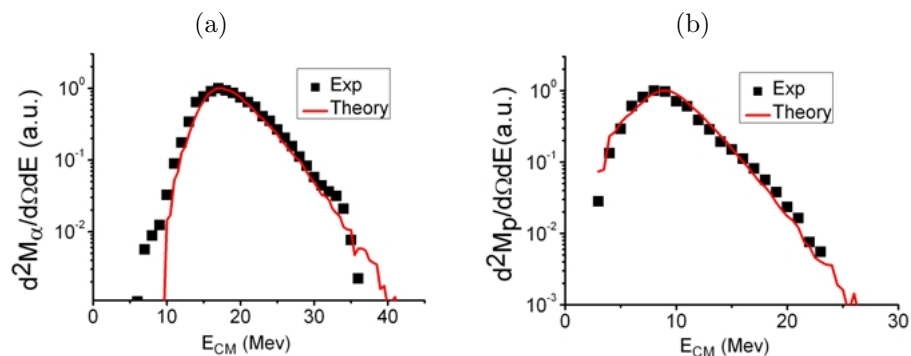
Figure 4.7: Measured α−particles (a) and protons (b) energy spectra in the center of mass system ($\theta_{\mathrm{LAB}} = 142^{\mathrm{o}}$), for the FE channel, compared with the prediction of the dynamical model.
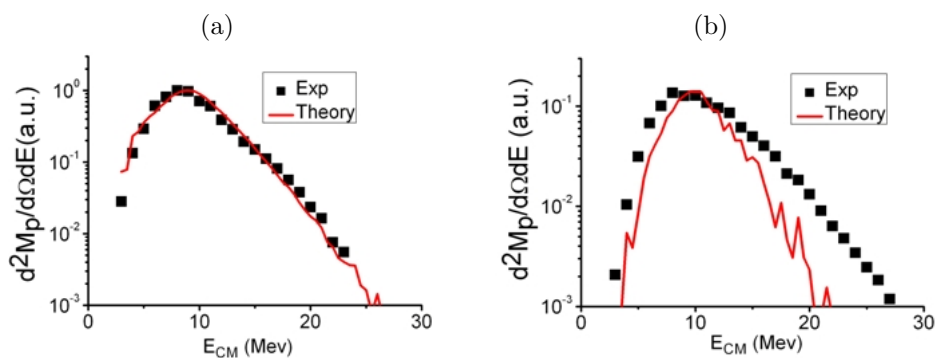
Figure 4.8: Same as Fig.4.7 for the pre-scission channel.

reproduce the data. The surplus of the measured low energy particles with respect to the simulation is indicative of strong deformations of the emitter. This deformation would produce a lowering of the high energy part of the spectrum, with respect to the spherical case, because of the increase of the moment of inertia. This effect is not observed, on the contrary we observe an excess of high energy particles with respect to the predictions of the model. Therefore this result, concerning pre-scission proton spectra, leaves an open question. Nevertheless, the comparison of the data with a calculations for deformed nuclei could be particularly elucidating. Such a study will be possible with the new version of the dynamical model, where we have introduced a consistent treatment of nuclear deformation for particle evaporation.

4.1.5 Angular Correlation ER-LCP

The angular correlation between LCP's and evaporation residues is the observable that characterizes 8πLP. In fact, due to the high granularity and the large number of used detectors it is possible to measure the coincidences with a large variety of geometrical configurations. As mentioned in Chapter III, the angular correlation has an oscillating behaviour coming out from a combined effect of kinematics and angular momentum. This observable appears to be more sensitive, than the spectral shapes, to the relevant parameters of SM: mainly to the level density parameter a and the angular momentum.

The comparison between calculations and experimental data is shown in Fig.4.9. Although the oscillating behaviour is well reproduced, the amplitude is overestimated by the model. As the value of the critical angular momentum $L_{crit} = 72\hbar$ and of the level density parameter a=A/6 are constrained by the other observables, it was not possible to change the value of these parameters in order to improve the agreement. Furthermore, reduction of the amplitudes could be obtained assuming deformed nuclei, but this possibility is ruled out by the good agreement found for the energy spectra, which indicate mainly spherical emitting nuclei. Further studies are needed to obtain a better reproduction of the angular correlation.

4.1.6 Fission time-scale

The time distribution of the fission process is important for understanding the dynamics, as one can explore the influence of different effects at different stages of fission process. The distribution of fission time for ^{132}Ce composite system predicted by the model are presented in Fig. 4.10(a) together with the fission rate R_f for the case of one-body dissipation with $k_s = 1$ and $a = A/6$.
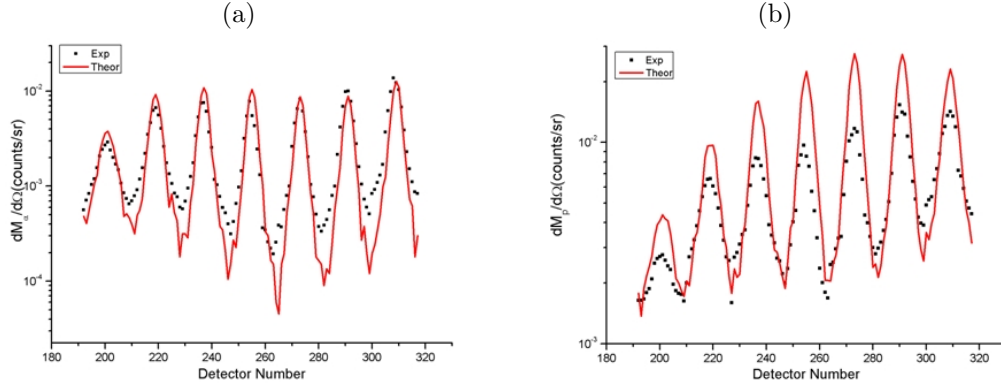
Figure 4.9: Measured ER-α (a) and ER-p (b) angular correlations, compared with the predictions of the dynamical model. LCP have been detected by 8πLP-Ball detectors, whose number is reported in the abscissa. Evaporation residues have been detected at $\theta_{LAB} = 4.5^o$.

The distribution has a maximum at t=$t_f^{max} \simeq 25 - 30 \times 10^{-21}s$. In the time interval $0 < t < t_f^{max}$ we observe a steep rise from 0 to a maximum value. At $t > t_f^{max}$ the fission time distribution has a nearly exponential decrease with a long tail lasting up to 10^{-16} s. Furthermore, one can see from this figure that at the time interval $0 < t < \tau_d$ there are no fission events at all. The time $\tau_d = 5 \times 10^{-21}$ s is a fission delay time, which is used quite often in fission studies [Gra80]. The arrow at t=1250 $\times 10^{-21}$ s indicates the mean fission time $\langle t_f \rangle$. This value can be strongly influenced by the tail of the distribution. In order to determine the mean value with low uncertainty for such a function, one needs to have a large statistics in Langevin simulations. The last could be quite difficult especially for the light fissioning nuclei. Therefore, as the main percentage yield of fission events lies at $t < 400 \times 10^{-21}$ s one can estimate this parameter of the fission time distribution on this time interval.

In Fig. 4.10(b) it is presented the fission rate $R_f(t)$ obtained at different conditions: the $R_f(t)$ calculated at L=60 $\hbar$ and 70 $\hbar$ without evaporation, and for the complete calculation including evaporation for all angular momenta.

The $R_f(t)$ functions at L=60 $\hbar$ and 70 $\hbar$ represent the limits in case of no evaporation, these L values corresponding to the characteristic values for fusion-fission cross section. Inclusion of evaporation in the calculations results in a substantial decrease of the excitation energy U from the beginning of decay process; as a result the $R_f(t)$ is reduced and slightly overcomes the $R_f(L = 60, t)$ at t$\simeq 25 - 30 \times 10^{-21}$ s and after has a smooth decrease. Comparing the fission rate with particle evaporation with the fission time distribution one can see a direct correlations in the behaviour between these

98
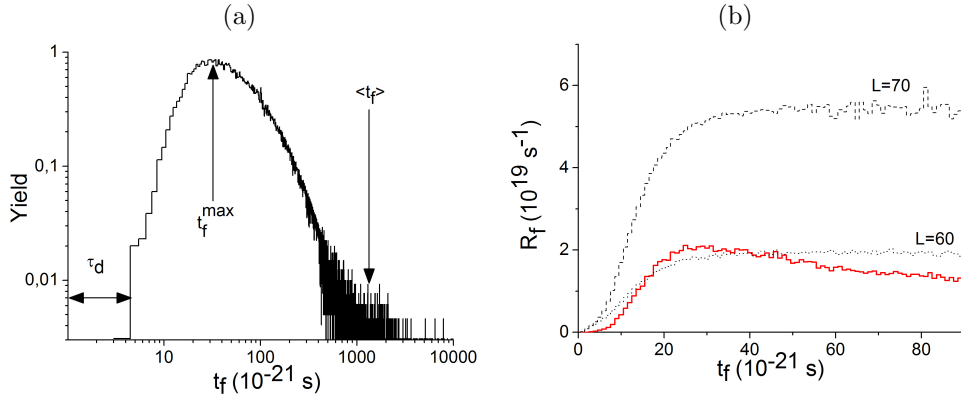
Figure 4.10: Fission time distribution (percentage) and fission rate. See text for details.

two quantities. The fission delay time τ_d, where $R_f(t)=0$ and no fission events occur is $\tau_d \simeq 5{\times}10^{-21}$ s. The steep rise of fission time distribution corresponds to the increase of $R_f(t)$ till the maximum value. The maximum of $R_f(t)$ and fission time distribution are at $t_f^{max} \simeq 25 - 30 \times 10^{-21}$ s. For values of time $t > t_f^{max}$ the smooth decrease of $R_f(t)$ corresponds to the nearly exponential decrease of fission time distribution. In the case of $R_f(t)$ without particle evaporation, where the stationary values of $R_f(L = 60 - 70, t)$=constant, the decrease of fission time distribution will be exactly exponential.

In order to illustrate the characteristic time of the evaporation process we show in Fig. 4.11 the percentage yields of the first $(Y_{n1}(t))$, the second $(Y_{n2}(t))$, and the third $(Y_{n3}(t))$ pre-scission neutron as a function of time. The yields for the first pre-scission proton and alpha-particle are also presented. From this figure one can see that evaporation of particles starts from t=0. The yields for the first neutron, proton, and $\alpha-$particle have approximately the same behaviour as a function of time. It is an exponential decrease from the maximum at t=0 to the value 0 at t=250 $\simeq 10^{-21}$ s. Considering the emission of neutrons one can see that the emission of every next neutron requires a larger time, in comparison with the previous one. The maxima for $Y_{2n}(t)$ and $Y_{3n}(t)$ are at 100 $\times10^{-21}$ s and 900 $\times10^{-21}$ s, respectively. The main reason for such a behaviour is the reduction of the excitation energy U after each evaporation step. Using this characteristic time of emission of different particles one can estimate the timescales of the different processes accompanying the decay of the compound nucleus.

99
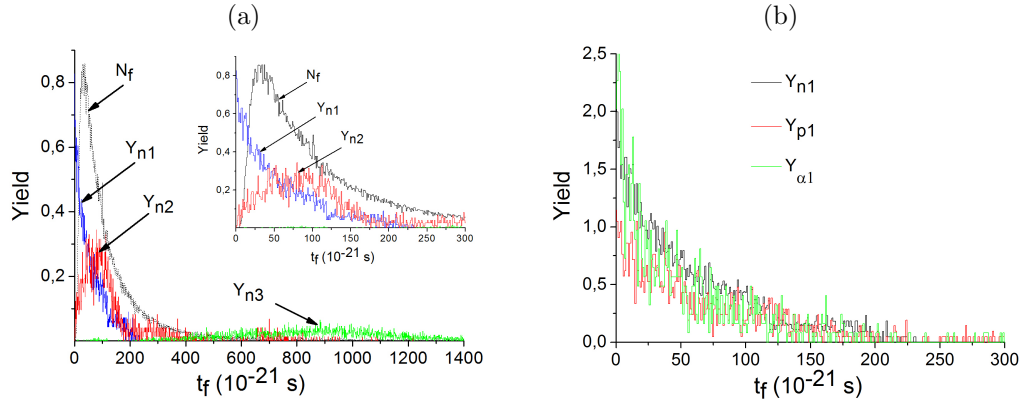
Figure 4.11: The yields of pre-scission particle multiplicities: a) first, second, and third pre-scission neutrons; b) first neutron, proton and alpha particle. See text for details.

4.2 Preliminary results for 180 MeV ^{32}S+^{126}Te system

The second reaction analyzed is ^{32}S +^{126} Te at E_{LAB} = 180 MeV, which produces the composite system ^{158}Er at U=92 MeV. This reaction has been already studied by Gavron and coll. [Gav87], in order to extract the main parameters of the fission process. In their analysis the observables compared with the results of calculations were: the fission cross section [Van83] and the pre-scission neutron multiplicity. They used a modified version of PACE2 incorporating the correction to the Bohr-Wheeler formalism due to nuclear viscosity [Gra80]. The good reproduction of the two observables allowed to deduce a transient time $\tau_{tr} = 35\pm15\times10^{-21}s$ and a lower limit of the reduced dissipation coefficient $\beta \geq 5 \times 10^{21}s^{-1}$.

We are carrying on for this system the same analysis illustrated before for $^{32}S +^{100} Mo$; the preliminary results concerned the observables are reported in Tab.4.5. As far as the analysis with the statistical model is concerned, the model strongly overestimates the proton and $\alpha-$particle multiplicities in evaporation residue channel, irrespective of the used input parameter within a realistic range of variability. A similar result has been found for ^{32}S+^{100}Mo system.

Concerning the analysis with the dynamical model, preliminary calculations show that the best reproduction of the experimental data is obtained assuming full (k_s = 1) one-body dissipation as in the previous reaction, with a value of the level density parameter a=A/9. This preliminary calculation

	M_p^{FE}	M_α^{FE}	M_n^{PRE}	M_p^{PRE}	M_α^{PRE}	σ_{FF} (mbarns)
Exp.	0.38(0.03)	0.23(0.08)	1.7(0.5)	0.034(0.005)	0.020(0.003)	195(20)
one-body,k_s=1,a=A/9	0.26	0.34	1.77	0.032	0.021	186

Table 4.5: Experimental and calculated particle multiplicities for the system ^{32}S $+^{126}$Te at E_{LAB} = 180 MeV in the FE and pre-scission channels together with the FF cross sections.

compound system	td (zs)	tfMAX(zs)	¡tf¿ (zs)
^{132}Ce	5	30	1250
^{158}Er	9	50	850

Table 4.6: Fission time extracted from the simulation adopting the dynamical model.

underestimates proton multiplicity and oversetimate $\alpha-$particle multiplicity in the evaporation residue channel. The result is shown in Tab. 4.5. Work is in progress to obtain a better overall reproduction of the data.

The fission time distribution predicted by the model presents the same behaviour obtained for the previous system; the extracted parameters are given in Tab.4.6. A similar behaviour as far for the ^{132}Ce nucleus is also found for the reduced viscosity parameter β as a function of the deformation. Finally the calculations support the independence of β on the temperature.

In conclusion, the preliminary results obtained for the ^{32}S $+^{126}$Te system confirm the general conclusions reached for the ^{32}S$+^{100}$Mo system, concerning the limitations of the SM and the physical parameters needed to reproduce the data with the dynamical model.

In Fig. 4.12 are shown the predictions of the dynamical model concerning β friction coefficient as a function of nuclear deformation, for different values of one-body reduction factor k_s and for two-body dissipation. Assuming full $(k_s = 1)$ one-body dissipation, which provides a good reproduction of the data we observe that large values of β are involved for nearly symmetrical shape, at the beginning of the fission process, with a decreasing behaviour of β with the increase of deformation.
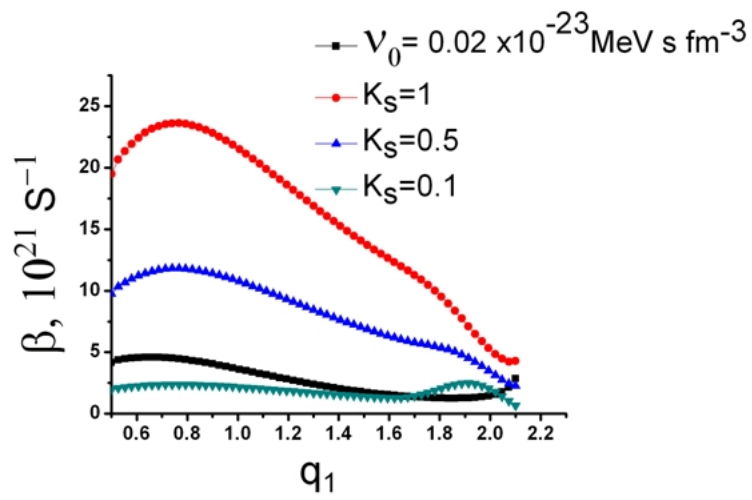
Figure 4.12: β friction coefficient as function of the nuclear deformation.

Summary and conclusions

In this work the fission dynamics for the composite systems ^{132}Ce and ^{158}Er at excitation energy U= 122 , 92 MeV respectively, has been studied. The main goal is to explore some debated aspects of the process: the fission time scale, the nature and the strength of the nuclear viscosity and its dependence on nuclear shape and temperature. The studied systems are particularly suited for such a study as they offer the opportunity to measure an extended set of observables in both fission and evaporation residue channels, implying severe constrains to the models.

Experiments have been carried out with 8πLP apparatus at the Laboratori Nazionali di Legnaro to measure light charged particle multiplicities and energy spectra in the pre-scission and ER channels, as well as channel cross sections, evaporation residue-light charged particle correlations and Mass-Total kinetic energy distributions of fission fragments. Data have been analysed in the framework of the statistical model and of a dynamical model based on three dimensional Langevin equations. For ^{158}Er the results have to be considered preliminary.

The statistical model is able to reproduce the data in the pre-scission channel, but it strongly overestimates the proton and $\alpha-$particle multiplicity in the evaporation residue channel for both reactions, irrespective of the input parameters. This result indicates the limitations of the statistical model and raises serious doubts on its use for studying fission dynamics.

As far as the dynamical model is concerned, a good overall agreement is obtained assuming full one-body dissipation with a shape-dependent viscosity parameter β. In particular, the fission proceeds with large values of $\beta \simeq 24 \times 10^{21}$s^{-1} for nearly spherical shapes at the beginning of the process, with a decreasing behaviour of beta reaching the value $\beta \simeq 5 \times 10^{21}$s^{-1} for highly deformed shapes. A reasonable agreement is also obtained assuming an unusually large value of two-body friction $\nu_0 = 0.15 \times 10^{-21}$ MeV s fm^{-3}.

The evidence of an over-dumped motion in the fission, resulting from our analysis, is in agreement with many of the results reported in the literature.

The fission time distribution provided by the model allows to obtain the average fission times for the two composite nuclei: $\langle t_f \rangle = 1250 \times 10^{-21}s$ and $\langle t_f \rangle = 850 \times 10^{-21}s$ for ^{132}Ce and ^{158}Er, respectively. The delay time, representing the initial time interval during which no Langevin trajectory has reached the scission point, i.e. where $\Gamma_f = 0$, are found $\tau_d = 5 \times 10^{-21}s$ and $\tau_d = 9 \times 10^{-21}s$, respectively. Finally, the transient time needed to build up the maximum value of the fission probability are $\tau_{tr} = 25 - 30 \times 10^{-21}s$ and $\tau_{tr} = 50 \times 10^{-21}s$. These values of the transient time are within the range of the phenomenological estimates based on the statistical model.

The pre-scission alpha-particle spectra for ^{132}Ce composite nuclei are consistent with emission from spherical nuclei, indicating that these particles are evaporated in the early stage of the fission process, where small deformations are involved. Similar results have been reported in Ref. [Hin92, Ike94]. Concerning pre-scission proton spectra, the excess of low energy particles with respect to the prediction of the model, is indicative of strong emitter deformations. This result is not supported by the behaviour of the high energy side of the spectrum, leaving an open question. A consistent treatment of nuclear deformation for particle evaporation has been just included in the dynamical model; a comparison of the data with this new version of the model will help to gain insight on this point.

The mass distribution for ^{132}Ce composite nuclei is reasonably well reproduced by the dynamical model. A slightly better agreement is obtained with one-body dissipation. The width of TKE distribution is underestimates by the model, irrespective of the dissipation mechanism. This faliure is relted to the treatment of the nuclear shapes at the scission configurations, in the model.

Finally, the dynamical model calculation supports the independence of the reduction viscosity parameter β on the temperature.

Bibliography

[Ade05] G.D. Adeev, *Phys. of Part. and Nucl.* **4**, 378 (2005).

[Aji86] N.N. Ajitanand, G. Larana et al., *Phys. Rev.* **C34**, 887 (1986).

[Aud03] G. Audi et al., *Nucl. Phys.* **A729**, 129 (2003).

[Bad01] C. Badimon, *PhD. Thesis*, **CENBG, Bordeaux** (2001).

[Beg85] S. Beghini et al., *Nucl. Instrum. Methods* **A239**, 585 (1985).

[Bha96] C. Bhattacharya et al., *Phys. Rev.* **C53**, 1012 (1996).

[Bas77] R. Bass, *Phys. Rev. Letters* **30**, 265 (1977).

[Bla82] M. Blann and T. T. Komoto, *Phys. Rev.* **C26**, 472 (1982).

[Bla52] J.M. Blatt et al., *Theor. Nucl. Phys.* Wiley, New York (1952).

[Blo78] J. Blocki et al., *Ann. Phys.* **113**, 330 (1978).

[Blo92] J. Blocki et al., *Nucl. Phys.* **A545**, 511c (1992).

[Boh39] N. Bohr and J.A. Wheeler, *Phys. Rev.* **56**, 426 (1939).

[Boh40] N. Bohr, *Nature* **137**, 344 (1940).

[Boh69] A. Bohr and B. Mottelson, *Nuclear structure* **Vol. I** Benjamin, New York (1969).

[Bor08] M.V. Borunov et al., *Nucl. Phys.* **A799**, 56 (2008).

[Bri76] H. C. Britt et al., *Phys. Rev.* **C13**, 1483 (1976).

[Bro03] A. Brondi et al., *Ann. Rep. LNL* (2003).

[Bro05] A. Brondi et al., *Ann. Rep. LNL* (2005).

[Bro90] U. Brosa et al., *Phys. Rep.* **197**, 167 (1990).

[But91] U. Butsch et al., *Phys. Rev.* **C44**, 1515 (1991).

[Cha92] D. Cha and G.F. Bertsch, *Phys. Rev.* **C46**, 306 (1992).

[Cha95] A. Chatterjee et al., *Phys. Rev.* **C52**, 3167 (1995).

[Cha00] R. J. Charity, Computer code GEMINI (unpublished)

[Coh74] S. Cohen et al., *Ann. Phys.* **82**, 557 (1974).

[Car86] N. Carjan et al., *Nucl. Phys.* **A452**, 381 (1986).

[Dav76] K. T. R. Davies et al., *Phys. Rev.* **C13**, 2385 (1976).

[Dil73] W. Dilg et al., *Nucl. Phys.* **A217**, 269 (1973).

[Dio92] I. Dioszegi et al., *Phys. Rev.* **C46**, 627 (1992).

[Eri58] T. Ericsson and V. Strutinski, *Nucl. Phys.* **8**, 243 (1958).

[Eri60] T. Ericson, *Adv. Phys.* **9**, 425 (1960).

[Fel87] H. Feldmeier, *Rep. Prog. Phys.* **50**, 915 (1987).

[Fro93] P. Frobrich et al., *Nucl. Phys* **A556**, 281 (1993).

[Fro96] P. Frobrich and R. Lipperheide, *Theory of nuclear reaction* Oxford: Clarandon Press, (1996).

[Fro98] P. Frobrich and I. I. Gontchar, *Phys. Report* **292**, 131 (1998).

[Gal74] J. Galin et al., *Phys. Rev.* **C10**, 109 (1986).

[Gav80] A. Gavron, *Phys. Rev.* **C21**, 230 (1980).

[Gav87] A. Gavron, *Phys. Rev.* **C35**, 579 (1980).

[Gho50] S.N. Ghosal, *Phys. Rev.* **80**, 939 (1950).

[Gil65] Gilbert and Cameron, *Canad. Jour. of Phys.* **43**, 1446 (1965).

[Gom81] J. Gomez Del Campo and R. G. Stokstad, *ORNL-TM* **7295**, (1981).

[Gon02] I. Gontchar et al., *Europhys. Lett.* **57**, 355 (2002).

[Gra80] P. Grangé and H.A. Weidenmüller , *Phys. Rev.* **B96**, 26 (1980).

[Gro67] J. R. Grover, *Phys. Rev.* **157**, 832 (1967).

[Hil92] M. Hilscher and H. Rossner, *Ann. Phys. Fr.* **17**, 471 (1992).

[Hin86] D. J. Hinde et al., *Nucl. Phys.* **A452**, 550 (1986).

[Hin89] D. J. Hinde et al., *Nucl. Phys.* **A582**, 497 (1989).

[Hin92] D. J. Hinde et al., *Phys. Rev.* **C45**, 1229 (1992).

[Hof94] D. J. Hofman et al. *Phys. Rev. Letters* **72**, 470 (1994).

[Hog78] P.E. Hodgson, *Nuclear reaction and nuclear structure*, Oxford: Clarandon Press (1978).

[Hui61] J. R. Huizenga and G. Igo, *Nucl. Phys.* **29**, 462 (1961).

[Ign75] A. V. Ignatyuk et al., *Yad. Fiz.* **21**, 485 (1975) [Sov. J. Nucl. Phys. **21**, 255 (1975)].

[Ike92] H. Ikezoe et al., *Phys. Rev.* **C46**, 1922 (1992).

[Ike94] H. Ikezoe et al., *Phys. Rev.* **C49**, 968 (1994).

[Jac09] D. Jaquet and M. Morjean, *Prog. Part. Nucl. Phys.* **63**, 155 (2009).

[Jur03] B. Jurado et al., *Nucl. Phys.* **A747**, 14 (2005).

[Kar01] A. V. Karpov et al., *Phys. Rev.* **C63**, 054610 (2001).

[Kel64] I. Kelson, *Phys. Rev.* **136**, 1667 (1964).

[Kil92] M. Kildir et al., *Phys. Rev.* **C46**, 2264 (1992).

[Koz08] E. M. Kozulin et al., *Instr. Exp. Tec.* **51**, 44 (2008).

[Kra40] H. A. Kramers, *Physica* **VII**, 284 (1940).

[Kra79] H. J. Krappe et al., *Phys. Rev.* **C20**, 992 (1979).

[Kra99] H. J. Krappe, *Phys. Rev.* **C59**, 2640 (1999).

[Kuz96] A. V. Kuznetzov et al., *Z. Phys.* **A354**, 287 (1996).

[Lar03] G. La Rana et al., *Eur. Phys. J.* **A16**, 199-207 (2003).

[Leo94] W. R. Leo, *Techniques for Nuclear and Particle Physics Experiments*, Springer-Verlag (1994).

[Les90] J. P. Lestone, *Ph. D. thesis Australian National University* and International Report No. ANU/P1084 (unpublished) (1990).

[Les91] J. P. Lestone, *Phys. Rev. Letters* **67**, 1078 (1991).

[Les95] J. P. Lestone, *Phys. Rev.* **C52**, 1118 (1995).

[Mav92] N. D. Mavlitov et al., *Z. Phys.* **A342**, 195 (1992).

[Nad02] P. N. Nadtochy et al., *Phys. Rev.* **C65**, (2002)

[Nad03] P. N. Nadtochy et al., *Phys. of Atom. Nucl.* **66**, 1203 (2003)

[Nad05] P. N. Nadtochy and G.D. Adeev, *Phys. Rev.* **C72**, 054608-1 (2005)

[New56] T. D. Newton, *Canad. J. Phys.* **34**, 804 (1956).

[Nix69] J. R. Nix, *Nucl. Phys.* **A130**, 241 (1969).

[Nix84] J. R. Nix and A.J. Sierk, *Nucl. Phys.* **A428**, 161c (1984).

[Nix87] J. R. Nix and A.J. Sierk, *Proc. 6th Adriatic Int. Conf. on Nuclear Physics, Dubrovnik* 1987.

[Pas99] G. Paush et al., *Nucl. Instr. and Met. in Phys. Res.* **A349**, 281-284 (1999).

[Pau73] H. C. Pauli, *Phys. Rep.* **7**, 35 (1973) and references therein.

[Pau94] P. Paul and M. Thoennesen,*Annu. Rev. Nucl. Part. Sci.* **44**, 65 (1994) and references therein.

[Per63] F. G. Perey, *Phys. Rev.* **131**, 745 (1963).

[Puh77] F. Puhlofer, *Nucl. Phys.* **A280**, 267 (1977).

[Rub98] V. A. Rubchenya et al., *Phys. Rev.* **C58**, 1587 (1998).

[Sat80] G. R. Satchler, *Introduction to nuclear reaction*, Macmillan Press LTD (1980).

[Sie78] A. J. Sierk et al., *Phys. Rev.* **C17**, 646 (1978).

[Sie80] A. J. Sierk and J.R. Nix, *Phys. Rev.* **C21**, 982 (1980).

[Sie86] A. J. Sierk, *Phys. Rev.* **C33**, 2039 (1986).

[Sto85] G. R. Stokstad, *The use of statistical model in heavy-ion reaction studies* **Vol. III** D. Allan Bromley (1985).

[Str91] E. Strumberger et al., *Nucl. Phys.* **A529**, 522 (1991).

[Tho87] M. Thoennessen et al., *Phys. Rev. Lett.* **59**, 2860 (1987).

[Tho93] M. Thoennessen and G. F. Bertsch, *Phys. Rev. Lett.* **71**, 4303 (1993).

[Til92] G. R. Tillack et al., *Phys. Lett.* **B296**, 296 (1992).

[Tro04] M. Trotta et al., *Ann. Rep. LNL* (2004).

[Van83] J. van der Plicht et al., *Phys. Rev.* **C28**, 2022 (1983).

[Var89] E. Vardaci, *VISM, a computer program for analysis* **CMU** (1989).

[Var98] E. Vardaci et al., *Eur. Phys. J.* **A2**, 55 (1998).

[Var00] E. Vardaci et al., in *Proceedings of the International Symposium on Dynamics Aspects of Nuclear Fission, Casta-Papiernicka, Slovak Republic, Oct 1998*, edited by Yu. Ts. Oganessian, J. Kliman and S. Gmuca (World Scientific, Singapore, 2000), p. 261.

[Var10] E. Vardaci et al., Forthcoming paper, accepted by *Eur. Phys. J.* .

[Vaz84] L. Vaz, *Z. Phys. Atom and Nuclei* **318**, 231 (1984).

[Vig81] S. E. Vigdor, *Proc. XIIIth Masurian Summer School on Nuclear Physics. Mikolajki, Poland* Nukleonika, 26 (1981)

[Vio85] V. E. Viola et al., *Phys. Rev.* **C31**, 1550 (1985).

[Von86] T. Von Egidy et al., *Nucl. Phys.* **A454**, 109 (1986).

[Von88] T. Von Egidy et al., *Nucl. Phys.* **A481**, 189 (1988).

[Wad92] T. Wada et al., *Nucl. Phys.* **A538**, 283 (1992).

[Wad93] T. Wada et al., *Phys. Rev. Letters* **70**, 3538 (1993).

[Wei37] V. F. Weisskopf, *Phys. Rev.* **52**, 295 (1937).

[Wei40] V. F. Weisskopf and D. H. Ewing, *Phys. Rev.* **57**, 472 (1940).

[Wil64] D. Willmore and P. E. Hudson, *Nucl. Phys.* **55**, 673 (1964).

[Zan86] W. P. Zank et al., *Phys. Rev.* **C33**, 519 (1986).

List of Figures

112

113

114

115